

Vibration and Position Control of Piezoelectric Tube Scanners for Fast Atomic Force Microscopy

Iskandar Al-Thani Mahmood

**B.Eng (Hons) in Mechatronics Engineering
M.Sc in Mechatronics Engineering**

Supervisor: Professor S. O. Reza Moheimani

*A thesis submitted in fulfillment
of the requirements for the degree of*

Doctor of Philosophy

School of Electrical Engineering
and Computer Science

The University of Newcastle
Callaghan, NSW 2308
Australia

October, 2009

*To my parents,
for your love, support and prayers.*

Acknowledgments

I would like to thank my supervisor Professor S. O. Reza Moheimani for giving me his supports and guidance without which the completion of this thesis would be very difficult. Many thanks also go to my colleagues at the Laboratory for Dynamics and Control of Nanosystems (LDCN) specifically, Dr. Bharath Bhikajji, Dr. Andrew J. Fleming and Dr. Kexiu Liu for their direct collaborations on different parts of this thesis. I also need to extend my thanks to those who have been there along the way, including Dr. Sumeet S. Aphale, Dr. Yuen Yong and many other people in LDCN.

On a personal note, I would like to thank my wife Salmi Mohd Nazir for always being there for me, your faith and belief in me and of course, your love. To my precious children Najihah 'Aqilah and Muhammad Kamil Zaki, thank you for the constant inspiration both of you bring to my life. Last but not least, I would like to thank my parents for their love and prayers, without whom I would not be where I am now.

Declaration

This thesis contains no material which has been accepted for the award of any other degree or diploma in any university or other tertiary institution and, to the best of my knowledge and belief, contains no material previously published or written by another person, except where due reference has been made in the text. I give consent to this copy of my thesis, when deposited in the University Library, being made available for loan and photocopying subject to the provisions of the Copyright Act 1968.

Iskandar Al-Thani Mahmood

October, 2009

List of Publications

During the course of this research, a number of papers have been submitted to international journal and conferences. The following is a list of those articles which have already been appeared in international journals or accepted for publication, as well as a list of conference papers which have been presented or accepted for presentation.

Journal Articles

1. I. A. Mahmood, S. O. R. Moheimani and B. Bhikkaji. A new scanning method for fast atomic force microscopy. Conditionally accepted in *Nanotechnology, IEEE Transactions on*, 2009.
2. I. A. Mahmood and S. O. R. Moheimani. Fast spiral-scan atomic force microscopy. *Nanotechnology*, Volume 20, Number 36, Pages 365503 (4pp), September 2009.
3. I. A. Mahmood and S. O. R. Moheimani. Making a commercial atomic force microscope more accurate and faster using positive position feedback control. *Review of Scientific Instruments*, Volume 80, Number 6, Pages 063705 (8pp), June 2009.
4. I. A. Mahmood, S. O. R. Moheimani and K. Liu. Tracking control of a nanopositioner using complementary sensors. *Nanotechnology, IEEE Transactions on*, Volume 8, Number 1, Pages 55 – 65, January 2009.
5. I. A. Mahmood, S. O. R. Moheimani and B. Bhikkaji. Precise tip positioning of a flexible manipulator using resonant control. *Mechatronics, IEEE/ASME Transactions on*, Volume 13, Number 2, Pages 180 – 186, April 2008.

Conference Papers

1. I. A. Mahmood and S. O. R. Moheimani. Improvement of accuracy and speed of a commercial AFM using positive position feedback control. *American Control Conference*, St. Louis, Missouri, June 2009.
2. I. A. Mahmood, K. Liu and S. O. R. Moheimani. Two sensor based H_∞ control of a piezoelectric tube scanner. *IFAC World Congress*, Seoul, Korea, July 2008.
3. I. A. Mahmood, S. O. R. Moheimani and B. Bhikkaji. Precise tip positioning of a flexible manipulator using resonant control. *Advanced Intelligent Mechatronics*, Zurich, Switzerland, September 2007.
4. I. A. Mahmood, B. Bhikkaji and S. O. R. Moheimani. Vibration and position control of a flexible manipulator. *Information, Decision and Control*, Adelaide, Australia, February 2007.

ABSTRACT

The performance of piezoelectric tube scanner in Atomic Force Microscope (AFM) is limited by vibrations and nonlinearities exhibited by the piezoelectric material such as hysteresis and creep. The aforementioned limitations restrict the use of the piezoelectric tube scanner for fast and high resolution operations. As such, this thesis presents several ways of improving the speed and accuracy of piezoelectric tube scanner for the use in Atomic Force Microscopy. In this thesis, two types of feedback control approaches are designed and implemented experimentally in order to improve the performance of piezoelectric tube scanners. The first approach uses strain voltage signal induced in the piezoelectric tube to measure of high frequency displacements of the scanner. Together with capacitive sensor, the use of strain voltage signal allows the closed-loop bandwidth to be increased for fast scans without the additional sensor noise otherwise contributed by the capacitive sensor during fast operation of the scanner. In the second approach, a Positive Position Feedback (PPF) control scheme is implemented on a commercially available AFM to compensate for scan-induced vibration and cross-coupling of its piezoelectric tube scanner. As a result of the implementation of the PPF control scheme, the scanning speed is doubled in comparison to the scanning speed obtained from the standard controller supplied with the commercial AFM. Finally, a spiral scanning method is comprehensively described and evaluated for the use in AFM. Two modes of spiral scanning method, Constant Angular Velocity (CAV) and Constant Linear Velocity (CLV) modes, are presented and compared with the widely used raster scanning method. The use of the spiral scan in CAV mode is shown to allow the scanning speed to be increased very high, approaching the mechanical bandwidth of the scanner. The use of the spiral scan in CLV mode allows scanning of samples to be done at linear velocity, a property shared with the raster scan.

Contents

1	Introduction	1
1.1	Thesis Objectives	1
1.2	Thesis Outline	3
2	Atomic Force Microscopy	5
2.1	Introduction	5
2.2	Working principle of Atomic Force Microscope	7
2.3	Operating modes in Atomic Force Microscopy	9
2.3.1	Static mode	9
2.3.2	Dynamic mode	11
2.4	Piezoelectric Tube Scanner	14
2.5	Limiting factors for high-precision positioning	17
2.5.1	Hysteresis	17
2.5.2	Creep	20
2.5.3	Vibrations	22
2.6	Summary	24
3	Feedback Control of a Piezoelectric Tube Scanner using Complementary Sensors	25
3.1	Introduction	25
3.2	System Description	28
3.3	System Identification	32
3.4	Controller Design	35

3.4.1	Two-sensor-based H_∞ controller	35
3.4.2	One-sensor-based H_∞ controller	42
3.5	Results	44
3.5.1	Hysteresis reduction	44
3.5.2	Closed-loop frequency response	46
3.5.3	Time response	46
3.5.4	One-sensor-based H_∞ controller	50
3.6	Summary	52

4 Positive Position Feedback control of an Atomic Force Microscope **53**

4.1	Introduction	53
4.2	Experimental Setup	55
4.3	System Identification	58
4.4	Controller Design	61
4.4.1	PPF Controller	61
4.4.2	High-gain Integral Controller	65
4.5	Experimental Results	67
4.5.1	Frequency and Time Responses	67
4.5.2	AFM Imaging	71
4.6	Discussion of Results	74
4.7	Summary	75

5 Fast Spiral-Scan Atomic Force Microscopy **76**

5.1	Spiral Scan	77
5.1.1	The CAV spiral	78
5.1.2	The CLV spiral	81
5.1.3	Inversion Technique for CLV spiral	82

5.1.4	Total scan time: Spiral scan vs. Raster scan	85
5.1.5	Mapping Spiral Points to Raster Points	86
5.2	Controller Design	88
5.3	Results	89
5.3.1	Tracking Performance	89
5.3.2	AFM Imaging	92
5.4	Summary	98
6	Conclusions	99
	Bibliography	102
	Appendix	111

List of Figures

2.1	Basic AFM schematic with feedback controllers.	8
2.2	Curves illustrating micro-cantilever deflection corresponding to the scanner vertical displacement during approach and retraction of the tip in static mode. During retraction, the tip is affected by an additional surface tension force from the ambient water layer on the sample surface which caused the tip-sample separation to occur at a longer distance.	11
2.3	Amplitude-frequency curve illustrating a shift in the resonant frequency of the micro-cantilever from ω_o to $\widetilde{\omega}_o$ due to a shift in the gradient of the interactive forces. In AM mode, the micro-cantilever is driven at a fixed frequency ω_f and the change in the resonant frequency ΔF resulted in a change in the oscillating amplitude ΔA . In FM mode, the oscillating amplitude remain unchanged as the micro-cantilever is always driven at its resonant frequency.	13
2.4	(a) Front view and (b) Bottom view drawing of the piezoelectric tube scanner featuring the labels for each electrodes. (Both drawings are not to scale and the thickness of the electrodes is exaggerated.)	15
2.5	Illustration of (a) staircase and (b) triangular wave signals applied to the y axis and x axis respectively to obtain (c) a raster pattern with 5 x 5 data points.	17

2.6	The effect of hysteresis on the piezoelectric tube scanner when driven by a voltage source. (a) Measured scanner's displacement (solid line) due to 5 Hz triangular wave input signal (dashed line). (b) Hysteresis curve illustrating the relationship between the scanner's displacement and the reference input signal. (c) The resulting surface topography image of a calibration grating obtained using the same piezoelectric tube scanner. . . .	19
2.7	Successive AFM images of a calibration grating taken after the scanner was applied with a step voltage to offset each axis of the scanner by $4\text{ }\mu\text{m}$. The images was scanned horizontally with the image origin at bottom-left of each image.	21
2.8	The effect of scan-induced vibration on piezoelectric tube scanner. Scanner's displacements (solid line) when driven by (a) 10 Hz and (b) 30 Hz triangular wave signals (dashed line). AFM images of a calibration grating generated at scan frequency of (c) 10 Hz and (d) 30 Hz.	23
3.1	Piezoelectric tube dimensions in millimeters. (a) Isometric-view and (b) Bottom-view (dimensions are not to the scale and the thickness of the electrode is exaggerated).	29
3.2	The piezoelectric tube is housed in a circular aluminum enclosure.	30
3.3	Schematics of the proposed feedback control system.	32
3.4	One-loop-frequency responses, $G_{v_x u_x}(i\omega)$ (dash-dots), $G_{c_x u_x}(i\omega)$ (dash), and the identified model $G_{y_x u_x}(s)$ (solid).	33
3.5	2-DOF control block diagram.	37
3.6	Feedback control block diagram with weighting functions.	38
3.7	General feedback control configuration.	39
3.8	(a) Weighting functions. (b) Sensitivity functions: desired (solid), achieved two-sensor (dash) and achieved single-sensor (dash-dot).	40

3.9	Frequency response of the designed controllers $K_c(s)$ (solid), $K_v(s)$ (dash) and $\tilde{K}_c(s)$ (dash-dot).	41
3.10	Procedure to obtain shaped reference $r(t)$	41
3.11	2-DOF control block diagram for the one-sensor-based H_∞ controller. . . .	42
3.12	Feedback control block diagram with weighting functions for the one-sensor-based H_∞ controller.	43
3.13	Hysteresis plot of open-loop 5 Hz scan using (a) voltage amplifier and (b) charge amplifier.	45
3.14	Experimentally obtained frequency responses of $T_{y_x r}(i\omega)$ (solid), $T_{y_x \tilde{d}_i}(i\omega)$ (dash) and $G_{y_x u_x}(i\omega)$ (dash-dots).	47
3.15	Open-loop (left) and closed-loop (right) time response plots of 5, 20 and 40 Hz scan. Solid line is measured scanners displacement and dashed line is desired trajectory.	48
3.16	Experimentally obtained closed-loop frequency responses using one-sensor-based H_∞ controller, $T_{y_x r}(i\omega)$ (solid), $T_{y_x \tilde{d}_i}(i\omega)$ (dash) and $G_{y_x u_x}(i\omega)$ (dash-dots).	50
3.17	Closed-loop time response plots of 5, 20 and 40 Hz scan using one-sensor-based H_∞ controller. Solid line is measured scanners displacement and dashed line is desired trajectory.	51
4.1	SPM system and experimental setup used in this work.	56
4.2	Top view of the piezoelectric tube with the internal and external electrode wired in a bridge configuration.	58
4.3	Block diagram of the experimental setup used for system identification of the scanner.	59
4.4	Experimental (dash-dot) and identified model (solid) frequency response of (a) $G_{c_x u_x}(i\omega)$ and (b) $G_{c_y u_y}(i\omega)$	60

4.5	Structure of the x axis feedback controller. The inner feedback loop is a PPF controller designed to damp the highly resonant mode of the tube. Integral action is also incorporated to achieve satisfactory tracking.	62
4.6	Map of open-loop (o), desired closed-loop (\times) and achieved closed-loop (+) poles for the x axis.	64
4.7	Bode diagrams showing gain margins when a unity gain integral controller is cascaded with undamped ($--$) and damped ($---$) scanner's transfer functions in (a) x and (b) y axes.	66
4.8	Open-loop (dash) and closed-loop (solid) frequency responses of the scanner. The resonant behavior of the scanner is improved by over 30 dB due to control action. The proposed feedback control strategy results in significant improvement in cross-coupling between the fast and slow axes of the scanner.	68
4.9	Closed-loop (dash) and open-loop (solid) tracking performance (left) and cross-coupling properties (right) of the scanner for 2 Hz scan (top), and 30 Hz scan (bottom). (A small phase shift was purposely added into the close-loop time responses in order to clearly display the open- and closed-loop time responses.)	70
4.10	First two columns: AFM images of NT-MDT TGQ1 grating scanned in contact mode constant force at 2, 10 and 30 Hz. Images displayed in (a), (b) and (c) were developed using the well-tuned PI controller. Images displayed in (d), (e) and (f) were generated using the PPF controller. A significant improvement in image quality can be observed. Third column: We were able to generate images at scan frequencies beyond the AFM limit of 30 Hz. 40, 50 and 60 Hz scans are illustrated in (g), (h) and (i) respectively.	72

4.11	Cross-section (solid) and reference (dash) curves of the AFM images illustrated in Fig. 4.10 (a) to (i). The cross-section curves were taken about the center of the AFM images and parallel to the square profile of the calibration grating. The scan direction of the curves displayed in (a), (b) and (c) are from 0 to 8 μm . The scan direction of the curves displayed in (d) to (i) are from 8 to 0 μm	73
5.1	Spiral trajectory of 6.5 μm radius with <i>number of curve</i> = 8.	78
5.2	Input signals to be applied to the scanner in the x and y axes of the scanner to generate CAV spiral scan with $\omega = 188.50$ radians/sec. Solid line is the achieved response and dashed line is the desired trajectory.	80
5.3	Input signals to be applied to the scanner in the x and y axes of the scanner to generate CLV spiral scan with $v = 1.13$ mm/sec (or $\tilde{\omega}_{end} = 188.50$ radians/sec). Solid line is the achieved response and dashed line is the desired trajectory.	83
5.4	Spiral points (+) for (a) CAV spiral with $\omega_s = 188.5$ radians/s and (b) CLV spiral with $v_s = 1.1$ mm/s. The sampling frequency used for generating these spiral points is 2 kHz. Both spiral trajectories have a 6.5 μm radius with <i>number of curves</i> = 8. The spiral points are plotted on top of the raster points (.) that make up a 13×13 μm raster-scanned image with of 8×8 pixels resolution.	87
5.5	First two columns: (a) - (f) Tracking trajectories of CAV spirals between between ± 0.15 μm in closed-loop for $\omega_s = 31.4, 94.3, 188.5, 565.5, 754.0$ and 1131.0 radians/s. Third column: (g) - (i) Tracking trajectories of CLV spirals between ± 0.30 μm in closed-loop for $v_s = 0.2, 0.6$ and 1.1 mm/s. The pitch of the spirals was set at 25.44 nm. Solid line is the achieved response and dashed line is the desired trajectory.	91

- 5.6 AFM images of NT-MDT TGQ1 grating scanned in closed-loop using the CAV spiral scanning mode for (a) - (f) $f_s = 5, 15, 30, 90, 120$ and 180 Hz (which corresponds to $\omega_s = 31.4, 94.3, 188.5, 565.5, 754.0$ and 1131.0 radians/s) and using the CLV spiral scanning mode for (g) - (i) $v_s = 0.2, 0.6$ and 1.1 mm/s. The *number of curves* for these AFM images was set to 512. 94
- 5.7 Cross-section (solid) and reference (dash) curves of the AFM images illustrated in Fig. 5.6 (a) to (i). The cross-section curves were taken about the center of the AFM images and parallel to the square profile of the calibration grating. 95
- 5.8 Probe deflection signals showing the profile of the calibration grating for (a) $\omega_s = 31.4$ radians/s and (b) $\omega_s = 754.0$ radians/s. 96
- 5.9 AFM images of NT-MDT TGQ1 grating scanned in open-loop using the CAV spiral for (a) - (c) $f_s = 5, 30,$ and 90 Hz. The *number of curves* for these AFM images was set to 512. 97

List of Tables

3.1	Numerical quantification of hysteresis	46
3.2	RMS values of tracking error	49
5.1	RMS values of tracking error and total scanning time for CAV and CLV spiral scans. Images have a resolution of 512×512 pixels.	90
5.2	RMS values of spiral to raster points mapping error for CAV and CLV spiral scans.	93

Chapter 1

Introduction

In recent years, Atomic Force Microscope (AFM) has become an important tool in nanotechnology research [11, 50]. AFM was first conceived to generate three-dimensional (3D) images of conducting and nonconducting surfaces with extremely high resolutions down to the atomic level. Recently, AFM is also being used in applications that involve manipulation of matter at a nanoscale [55, 57, 73]. A critical component of an AFM is the scanner which is used to move either the sample or the micro-cantilever in a raster pattern in the x - y plane. The scanner also controls the tip-sample distance through the z axis servo. Today, the majority of commercially available AFMs use a piezoelectric tube scanner for the three-dimensional (3D) positioning [52], although flexure-based nanopositioners [4, 65, 70] are emerging as a viable, albeit more expensive alternative. However, the positioning precision and scanning speed of the piezoelectric tube can be adversely affected by vibrations and nonlinearities exhibited by the piezoelectric material such as hysteresis and creep [16]. Therefore, the following section details out the objectives of this thesis.

1.1 Thesis Objectives

The first objective considered in this thesis is to use feedback control approach to improve positioning precision and scanning speed of piezoelectric tube scanners. Feedback controllers are designed to achieve good damping ratio for the first resonant mode of the scanner and to achieve a high closed-loop bandwidth for fast and accurate tracking of input signals. Additionally, charge sources are used to drive the piezoelectric tube scanner instead of the widely used voltage source in order to reduce the effect of hysteresis. Nonethe-

less, when capacitive sensors are used to provide the scanner's displacement measurements for these feedback controllers, the effect of sensor noise on the overall system increases as the closed-loop bandwidth increases. This trade-off is minimized in this thesis by using a low-noise strain voltage signal induced in the piezoelectric tube instead of using the measurements from capacitive sensors for high-frequency displacement measurements. A two-input one-output H_∞ controller is designed for a prototype piezoelectric tube scanner to utilize these two sources of scanner displacement measurements.

Another feedback controller which utilizes only capacitive sensor measurements is designed for implementation on a commercial AFM. Here, a Positive Position Feedback (PPF) controller that was initially used to suppress mechanical vibrations of highly resonant aerospace structures [22] is designed to bring about improvements in term of scanning speed and scanned image accuracy to the commercial AFM. The PPF controller is used to compensate for vibration in the piezoelectric tube scanner of the commercial AFM by shifting its closed-loop poles further into the left-half plane (LHP). A high-gain integral controller is also used to provide tracking and to compensate for cross-coupling between lateral axes of the piezoelectric tube scanner.

The second objective of this thesis is to describe and evaluate spiral scanning method for fast AFM. Here, the piezoelectric tube scanner is forced to follow a spiral pattern instead of the well established raster pattern. The spiral scan is generated in two modes, a constant angular velocity (CAV) mode and a constant linear velocity (CLV) mode. Equations for generating the spiral scan in CAV and CLV modes and equations for calculating total scanning time associated with both modes of the spiral scan are derived. The advantages and disadvantages of spiral scan in both modes over raster scan are also explored. One obvious advantage of CAV spiral scan over raster scan is that the use of the single-tone input signals allows for scanning to be performed at very high speeds without exciting the resonance of the scanner and with relatively small control efforts. Spiral-scanned images are obtained

using both modes to determine the viability and the effectiveness of spiral scanning method for fast AFM.

1.2 Thesis Outline

This thesis begins with an overview of atomic force microscopy in Chapter 2, that includes the working principle of AFM and its various operating modes. In this chapter, a detail description encompasses the construction and mechanics of piezoelectric tube scanner, a major component in AFM, is also discussed. This is then followed by an in-depth discussion on the limiting factors for high-precision positioning of the piezoelectric tube scanner, namely, the effects of hysteresis, creep and scan-induced vibration.

In Chapter 3 the first objective of the thesis is addressed. Specifically, a two-input one-output H_∞ controller is designed to utilize a capacitive sensor and a low-noise strain voltage signal induced in the piezoelectric tube to provide low-frequency and high-frequency measurements of the scanner's displacement respectively. The closed-loop bandwidth of the system and its tracking performance are evaluated to illustrate the effectiveness of the proposed control scheme.

Chapter 4 continues to address the use of feedback control approach in a piezoelectric tube scanner. This chapter describes necessary steps for the implementation of the PPF control scheme which include integration of a dSPACE system into an AFM system and procedures for modeling the piezoelectric tube scanner and designing the PPF control scheme. The effectiveness of the PPF control scheme is evaluated at the end of this chapter by comparing AFM images obtained using this control scheme with the one obtained using a standard AFM controller, i.e., a well tune PI controller.

The focus of Chapter 5 is on the second objective of this thesis that is using spiral scanning method for fast AFM. This chapter begins with derivation of equations for gen-

erating the spiral scan in CAV and CLV modes and calculating total scanning time associated with both modes. Additionally, spiral scan parameters such as *spiral radius* and *number of curves* are defined. Procedures for mapping sampling points on a spiral trajectory to pixels that make up a raster-scanned image are discussed. This includes calculation of the error introduced by these mapping procedures on the generated AFM images. In the Results section tracking performance of CAV and CLV spirals and obtained spiral-scanned AFM images are presented. The AFM images are obtained using a piezoelectric tube scanner in closed-loop and open-loop.

In the final chapter, concluding remarks and a note on proposed future works are presented. In Appendix, three publications from the author's early PhD studies are attached in order to show a more complete picture of his PhD work. The outcomes are not included in the present thesis as they are in a different field.

Chapter 2

Atomic Force Microscopy

This chapter describes one aspect of Scanning Probe Microscopy (SPM), i.e., Atomic Force Microscopy (AFM), which has become the main subject matter of this thesis. In order to provide an overview of AFM, the first section briefly discusses different types of SPM and their applications. Section 2.2 presents the working principle of AFM that includes descriptions of the tip-sample interaction used in AFM and the basic components of this microscope. In Section 2.3, various available operating modes in AFM are presented. Section 2.4 provides an in-depth description of a piezoelectric tube scanner which is a critical component in AFMs. This description encompasses the construction and mechanics of the scanner. Finally, Section 2.5 discusses in detail three major effects, namely hysteresis, creep and vibration that limit the positioning precision of the scanner especially for high speed AFM and long scanning range operations. This discussion also includes distortions observed in AFM images as results of these effects.

2.1 Introduction

The invention of scanning tunneling microscopy (STM) [12, 13] by G. Binnig and his colleagues in 1982 has led to the development of various kinds of scanning probe microscopies (SPMs) such as Scanning Near-field Optical Microscopy (SNOM) [60], Atomic Force Microscopy (AFM) [11] and Scanning Magnetic Microscopy (SMM) [45]. These group of microscopies are referred to as SPM due to the use of probe in these devices for investigation and manipulation of material surfaces down to the atomic scale. Attached to the probe's free end is an extremely sharp tip whose geometrical shape determines the lateral resolution limit of the microscope [50]. Ideally, the tip should be atomically sharp in order

to achieve the atomic resolution. The tip is positioned very close to the sample surface during a scan. At such a close distance, there exist some highly localized tip-sample interaction that can be used to obtain local information and SPM images of the material surfaces. For example, the type of tip-sample interaction used in STM is the tunneling current that flows between a conductive tip and a conductive surface; in AFM is the interactive forces between a tip and a sample surface; and in SMM is the magnetic force between a magnetic coated tip with local magnetic field of a sample surface.

Since their invention, SPMs have become important research instruments in various applications of nanoscience and nanotechnology due to their capabilities to examine sample surfaces down to the atomic scale. Example of these applications include imaging of surface topography of Si(111) 7×7 at atomic resolution using STM [13] and AFM [32], measuring of magnetic forces in recording media using SMM [63] and imaging of molecular topography of a deoxyribonucleic acid (DNA) helix using AFM [76]. STM and AFM are also used in applications that involve manipulation of matter at nanoscale. In [19], operating under low temperature, an STM was used to position individual xenon atoms on a single-crystal nickel surface with atomic precision. The AFM capability to position individual atoms at the desired atomic positions was also demonstrated in [57, 73].

Among the family of SPMs, AFM has become the most widely used microscope to produce topographic images of material surfaces at nanoscale. This is mainly because it can be used to image any material surface, unlike STM where the sample is required to be conductive and most SNOMs where the sample is required to be optically transparent [10]. The AFM's ability to measure the interactive forces also has led to the modification of the AFM probe for measuring other type of forces such as magnetic force, electrostatic force and acoustic force. These modifications have resulted in SMM, scanning electrostatic force microscope (SEFM) and scanning force acoustic microscope (SFAM).

2.2 Working principle of Atomic Force Microscope

AFM was invented by G. Binnig and his colleagues in 1986 [11] based on their design of STM. In line with this, AFM is also known as scanning force microscopy (SFM). AFM is mainly used for imaging surface topography and measuring surface forces of samples with a very high precision. Since its invention, AFM has emerged as a standard tool in nanotechnology research. This is because AFM can be used on conducting as well as non-conducting sample surfaces in any environment including air, various gases, vacuum and fluid. Additionally, AFM can also operate at high and low temperatures.

The working principle of AFM is based on the use of interactive forces between a tip and a sample surface to sense the proximity of the tip to the sample [10]. Generally, the interactive forces can be attractive or repulsive depending on the tip-sample distance. At large tip-sample distances, the interactive forces are attractive and they turn repulsive at small tip-sample distances. The interactive forces are composed of long and short-range components. These interactive forces include electrostatic, magnetic, van-der-Waals and chemical forces [50]. All of these forces, except for the chemical forces, have strong long-range components that conceal the short-range components which change at atomic scale. In order to obtain AFM images with atomic resolution, the long-range force contributions need to be filtered out and only the short-range contributions need to be measured [10].

The basic components of AFM, as illustrated in Fig. 2.1, include a micro-cantilever (probe) with a sharp tip on the free end, a laser-photodetector sensor and a scanner. During operation, a sample is placed on the scanner and the tip of the micro-cantilever is brought very close to the sample surface at a distance of the order of a few nanometers, or less. At such a distance, depending on AFM operating mode, the interactive forces change static or dynamic properties of the micro-cantilever. The changes in the micro-cantilever are often measured using a beam-deflection technique that utilizes a laser-photodetector sensor [50]. In this technique, as illustrated in Fig. 2.1, the laser beam is pointed at the rear side of the

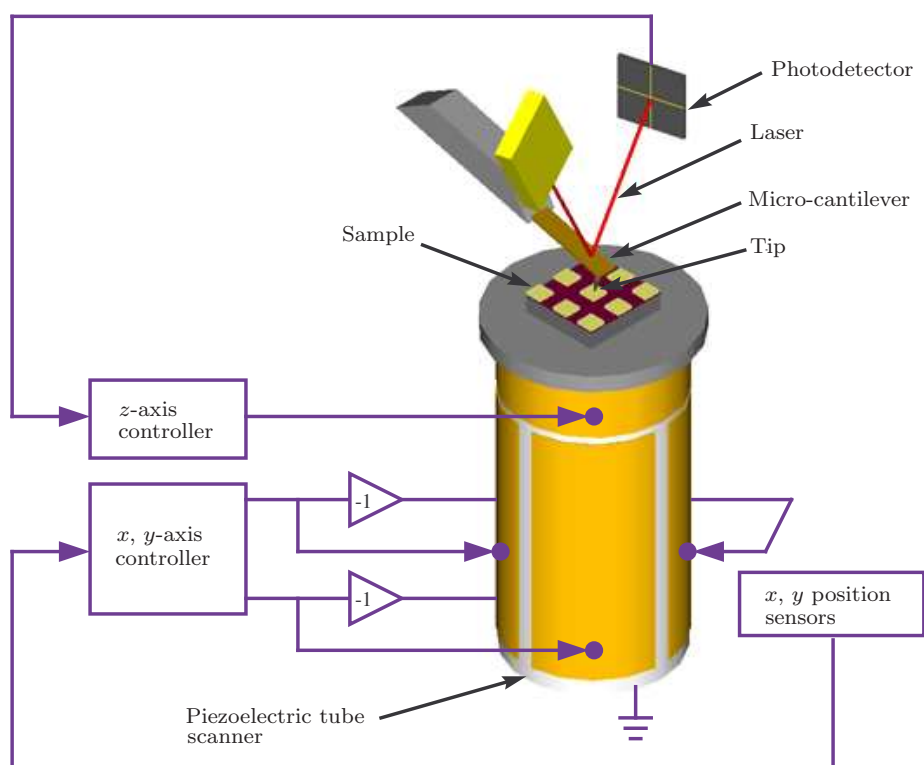


Figure 2.1 : Basic AFM schematic with feedback controllers.

micro-cantilever and its reflection is sensed by the photodetector. In order to generate an AFM image, the sample is typically scanned in a raster pattern.

2.3 Operating modes in Atomic Force Microscopy

The operating modes in AFM can be classified into static and dynamic modes. This classification is based on the different measurement parameters used in sensing the interactive forces. In static mode, the interactive forces are measured using static bending of the micro-cantilever. Whereas, in dynamic mode, the micro-cantilever is excited to vibrate at or near its resonance frequency and its dynamics properties which change under influence of the interactive forces are used as the measurement parameters. Apart from this difference, the basic operation of AFM in both modes remain the same.

2.3.1 Static mode

Static mode is also known as repulsive or contact mode due to the position of the tip relative to the sample surface during measurement. In this mode, the tip is brought into the repulsive force region and into contact with the sample surface [10]. At this position, the repulsive interactive force acting on the tip causes the micro-cantilever to deflect. AFM images can be generated by scanning the tip at a constant height over the entire area of interest on the sample surface. During scan, the measurements from the photodetector will vary according to the topographic features of the sample. These measurements are recorded and plotted as a function of the scanner's lateral positions to produce an AFM image of the interactive force distribution over the sample surface. Acquisition of the AFM image in this manner is called constant-height mode.

AFM images can also be obtained in constant-force mode. In this mode, the repulsive interactive force is kept constant during scan by varying the input voltage applied to the high-voltage amplifier for the z -electrode in order to vary the scanner's height. The variation in the input voltage is achieved through a feedback loop that makes use of the

measurement from the photodetector as a feedback signal. By keeping the repulsive interactive force constant, the tip-sample distance is kept constant regardless of the change in the sample surface. In this mode, the variation in the input voltage is proportional to the surface topography of the sample. Consequently, by plotting the input voltage as a function of the scanner's lateral position, a surface topography image of the sample can be obtained.

In static mode, the resolution of the obtained AFM images is limited by the tip-sample contact area. The diameter of the tip-sample contact area is typically in the range of 1 - 10 nm [50]. This dimension, which is larger than the atomic dimensions, rules out achieving atomic resolution in AFM images when the tip is in contact with the sample surface. In order to achieve atomic resolution in AFM images, the tip needs to be in non-contact with the sample surface but positioned very close within tenth of a nanometer to the sample surface. This is to allow the changes in the short-range attractive force that varies at atomic scale to be measured. However, such small tip-sample distance is very difficult to achieve in static mode due to mechanical instability called jump-to-contact phenomenon [10]. This phenomenon can be explained by referring to the deflection-displacement curve as illustrated in Fig. 2.2. The flat portion of the curve indicates that the tip is in mid-air and not under influence of any interactive forces. But as the sample approaches closer to the tip, at point A, the attractive interactive force starts to pull the tip and causes the micro-cantilever to deflect toward the sample. At point B, upon further approaches toward the tip, the gradient of the attractive interactive force becomes larger than the spring constant of the micro-cantilever. Here, the mechanical instability occurs where the tip suddenly jumps to be in contact with sample surface at point C. From here on, as the sample approaches further, the tip experiences repulsive interactive force and deflects away from the sample. This is represented by the sloped portion of the curve. During retraction of the sample, at point D, the tip suddenly jumps out of contact and returns to free air again. This is because at point D, the gradient of the attractive interactive force becomes weaker than the spring constant.

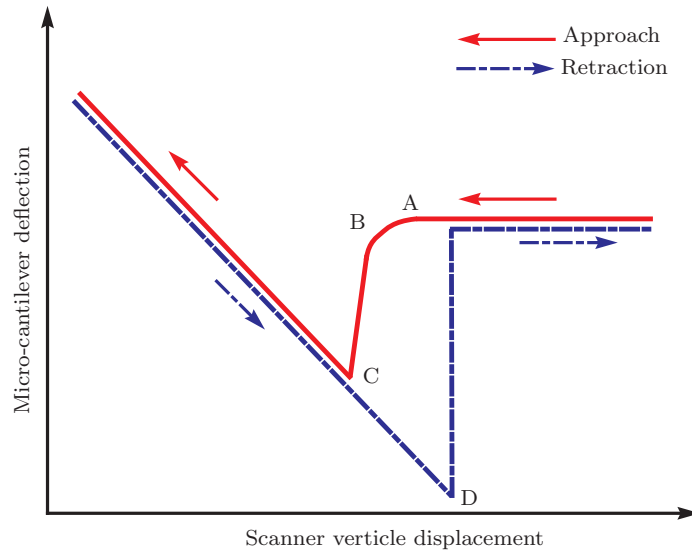


Figure 2.2 : Curves illustrating micro-cantilever deflection corresponding to the scanner vertical displacement during approach and retraction of the tip in static mode. During retraction, the tip is affected by an additional surface tension force from the ambient water layer on the sample surface which caused the tip-sample separation to occur at a longer distance.

In general, static mode can be used easily to obtain nanometer to micrometer resolution AFM imaging. However due to the jump-to-contact phenomenon, this mode is not suitable for atomic resolution imaging. Additionally, in this mode, the tip exerts a relatively large normal force and a considerable lateral force on the sample. Consequently, the probe is subject to significant wear. Hence, this mode may not also be suitable for soft samples that can be damaged easily, e.g., biological samples.

2.3.2 Dynamic mode

Dynamic mode is also known as attractive force imaging or non-contact imaging mode. During measurement, the tip is brought close but without coming in contact to the sample surface in order to assess the short-range attractive interactive force [10]. Note that at

such small tip-sample distance, in static mode, the tip would have likely to come in contact with the sample surface due to the jump-to-contact mechanical instability. However, this is avoided in dynamic mode by vibrating the micro-cantilever at its resonant frequency, thereby increasing its stiffness. The tip-sample distance could be further reduced in order to achieve AFM images with atomic resolution by operating dynamic mode in ultra-high vacuum (UHV) condition instead of in ambient conditions. Operating in ambient conditions, the tip-sample distance must be set at a larger distance to avoid the tip from being trapped in the ambient water layer on the sample surface. In [32] and [21], AFM images with atomic resolution were obtained using dynamic mode under UHV condition.

Dynamic mode can be operated in two basic operating regimes, namely amplitude-modulation (AM) mode and frequency-modulation (FM) mode. In AM mode [46], the micro-cantilever is excited to vibrate by applying an external signal with constant amplitude and frequency to a piezoactuator located at the base of the micro-cantilever. The frequency of the external signal is set close to the resonance frequency of the micro-cantilever. As the tip approaches the sample surface, a shift in the gradient of the interactive forces causes a shift in the resonance frequency and hence a corresponding shift in the oscillation amplitude of the micro-cantilever as illustrated in Fig. 2.3. The tip approach is stopped once the amplitude reaches to a specified set-point. Here, a lock-in amplifier [49] is used to obtain the amplitude and phase information from the output of the photodetector. During a scan, the amplitude is kept constant to this set-point through a feedback loop by varying the height of the scanner. This feedback loop keeps the tip-sample distance constant regardless of the change in the sample surface. In a similar technique undertaken in the constant-force static mode, a surface topography image of the sample is obtained by plotting the input voltage applied to the high-voltage amplifier for the z -electrode as a function of the scanner lateral position. The tip can be brought much closer to the sample surface such that it makes an intermittent contact with the sample surface during each oscillation cycle. This method of measurement is known as tapping mode [79]. In this mode, the amplitude the

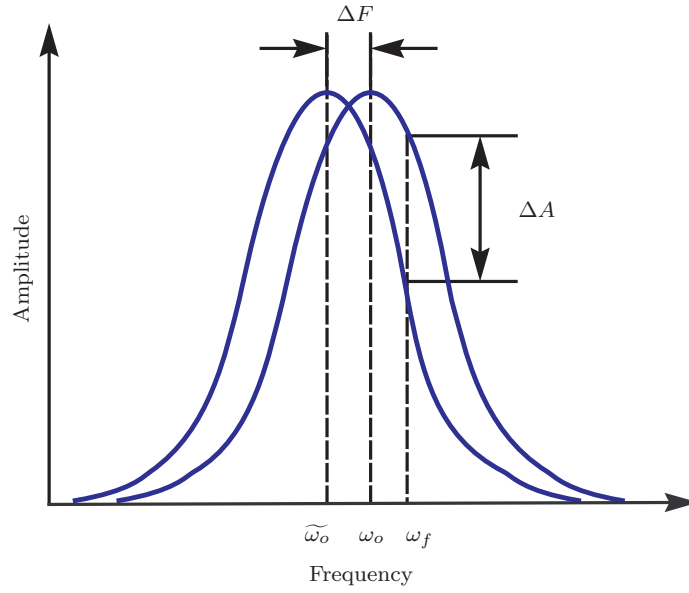


Figure 2.3 : Amplitude-frequency curve illustrating a shift in the resonant frequency of the micro-cantilever from ω_o to $\tilde{\omega}_o$ due to a shift in the gradient of the interactive forces. In AM mode, the micro-cantilever is driven at a fixed frequency ω_f and the change in the resonant frequency ΔF resulted in a change in the oscillating amplitude ΔA . In FM mode, the oscillating amplitude remain unchanged as the micro-cantilever is always driven at its resonant frequency.

micro-cantilever is also affected by the repulsive interactive force acting on the tip during the intermittent contacts.

In FM mode [1, 32], the micro-cantilever is always excited to vibrate at its resonance frequency. This is achieved by amplifying and phase-shifting the micro-cantilever oscillation signal (from the photodetector) by 90 degrees before using it to drive the piezoactuator. In doing so, a shift in the resonance frequency does not change the oscillation amplitude as the micro-cantilever is always vibrating at that frequency. This is illustrated in Fig. 2.3. However, the oscillation amplitude can still vary due to the influence of the interactive forces on the micro-cantilever. In order to fix the oscillation amplitude, an additional feedback loop is used to maintain it at a constant preset value. In FM mode, the change in the

resonance frequency are measured using a frequency demodulator [1] and used as a set-point signal for keeping the tip-sample distance constant during surface topography scan.

A major advantage of FM mode over the AM mode is that the change in the gradient of the interactive forces can be detected almost instantaneously in FM mode. The change in the resonance frequency settles on a timescale of $\tau_{FM} \approx \frac{1}{f_o}$, where f_o is the resonance frequency of the micro-cantilever. However, the change in the amplitude in AM mode does not occur instantaneously with the change in the gradient of the interactive forces. The change in the oscillation amplitude settles on a timescale of $\tau_{AM} \approx \frac{2Q}{f_o}$, where Q is quality factor of the micro-cantilever. The value of Q for a micro-machined micro-cantilever is typically a few hundred when operated in air and can reach hundreds of thousands when operated in vacuum [10].

2.4 Piezoelectric Tube Scanner

The use of the piezoelectric tube as a 3D scanner was first proposed in Ref. [14] to replace the use of tripod scanner in STM. The piezoelectric tube scanner was found to provide a faster response and a better positioning precision in comparison to the tripod scanner owing to its simpler and smaller construction. The piezoelectric tube scanner typically consists of a cylindrical tube made of radially poled piezoelectric material fixed at one end and free at the other. The piezoelectric tube is plated with a layer of electrode on the inner and outer surfaces of the tube. As shown in Fig. 2.4, the inner electrode is continuous and grounded, and the outer layer electrode is segmented into four equal sized electrode sectors of 90 degrees referred individually as $+x$, $-x$, $+y$, and $-y$ electrodes. However, the top part of the external electrode is not segmented. It is left as a circumferential electrode referred as $+z$ electrode. An aluminum or a stainless steel cube is fixed to the top of the tube to serve as a sample holder and also to provide capacitive sensors flat surfaces so that the tube deflection can be measured accurately in the case of a closed-loop scanner.

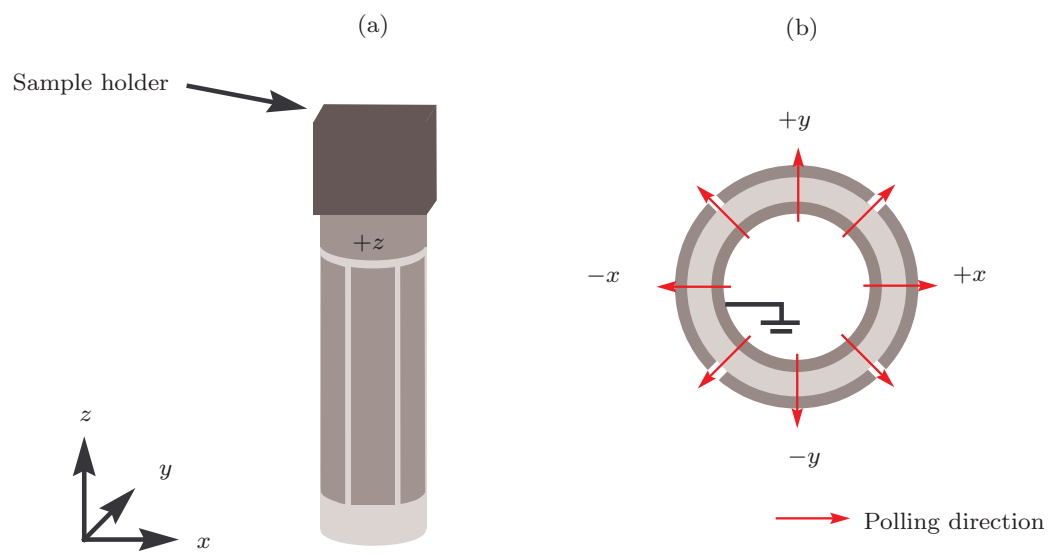


Figure 2.4 : (a) Front view and (b) Bottom view drawing of the piezoelectric tube scanner featuring the labels for each electrodes. (Both drawings are not to scale and the thickness of the electrodes is exaggerated.)

The motions of the scanner in the x axis and y axis are each controlled by a pair of external electrodes, $+x, -x$ and $+y, -y$ electrode pair respectively, that are driven by voltage signals of the equal magnitude but with opposite signs. When these voltage signals are applied to the electrode pairs, the piezoelectric material underneath those electrodes will expand or contract radially depending on the polarity of the applied voltage signal with respect to the polling direction of the piezoelectric material. If the polarity of the voltage signal coincides with the polling direction, the piezoelectric material will expand in the radial direction and causes the tube to reduce in length. If the polarity of the voltage signal is opposite to the polling direction, the piezoelectric material will contracts in the radial direction and causes the tube to increase in length. As opposite voltage signals are always applied to each electrode pair, the length of the tube on one side of the electrode pair will reduce, while the length on the opposite side will increase. This leads to a bend in the tube which produces a lateral deflection of the tube's free end in the x or y axis. The motion of the scanner in the z axis is produced by applying a voltage signal to the $+z$ electrode. Applying a positive or a negative voltage signal to the $+z$ electrode will respectively increase or decrease the tube length.

In AFM, the piezoelectric tube scanner is scanned in a raster pattern as illustrated in Fig. 2.5 (c). A raster scan is normally performed by moving the piezoelectric tube along the x axis (fast-axis) in forward and reversed directions (line scan), and then moving the piezoelectric tube along the y axis (slow-axis) in a small step to reach the next line scan. This movement is attained by applying a triangular wave signal to the x axis and a slowly increasing staircase signal to the y axis of the scanner as illustrated in Fig. 2.5 (a) and (b) respectively. During the forward pass of the line scan, the surface topographic information gathered by the probe is typically stored for image processing [51]. An AFM image is normally comprised of 256×256 data points. These data points are attained by performing 256 line scans and in each forward pass of the line scan, 256 data points are taken at an equal spacing.

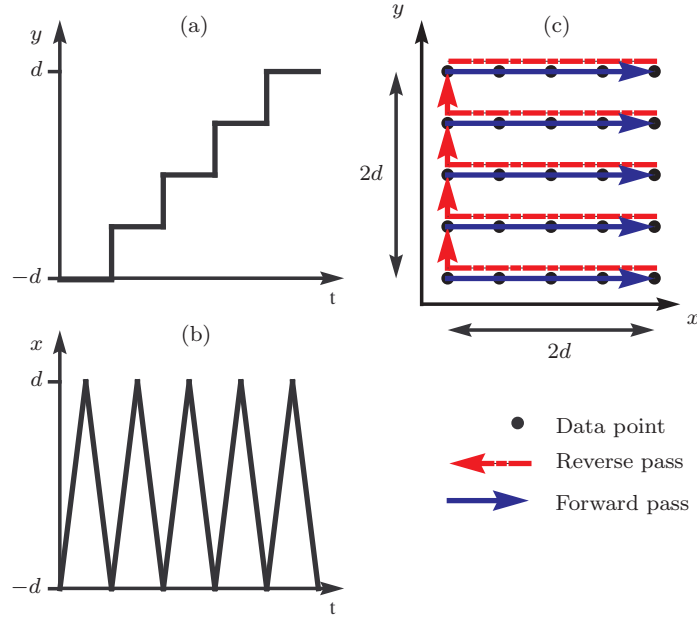


Figure 2.5 : Illustration of (a) staircase and (b) triangular wave signals applied to the y axis and x axis respectively to obtain (c) a raster pattern with 5×5 data points.

2.5 Limiting factors for high-precision positioning

As mentioned previously, AFM images of sample surface topography are typically generated by plotting the input voltage to the high-voltage amplifier for the z -electrode as a function of the scanner's lateral positions. In AFM imaging, the scanner's lateral positions are determined from the reference signals to the x and y axes instead of the scanner's true displacements. Hence, the accuracy of the scanner in tracking these reference signals is crucial for generating accurate AFM images. However, the positioning precision of piezoelectric tube scanner is limited by hysteresis, creep, and vibration [16]. These issues are further elaborated in the following sections.

2.5.1 Hysteresis

Piezoelectric materials are ferroelectric materials and for this reason they exhibit hysteretic behavior when driven by a voltage source [56]. The effect of the hysteresis increases as the

amplitude or the frequency of the applied voltage signal increases [2, 6]. In piezoelectric tube scanner, the hysteresis becomes the main source for nonlinear distortions. When a triangular wave signal is applied to a piezoelectric tube scanner, the resulting displacement can deviate from linear by as much as 15 % between the forward and backward movements due to the presence of hysteresis [50]. In order to minimize this effect, it is a common practice to limit the scan range to a small percentage of the scanner's maximum scan range. Although this method allows the scanner to operate within its linear range, it severely limits the scanner's ability to be used for long-range scans. Earlier AFMs compensate for hysteresis effect by perturbing the input triangular signal to achieve an acceptable trajectory, thus minimizing the effect of this particular form of nonlinearity [50]. Modeling a piezoelectric actuator as a linear dynamic system cascaded with a static nonlinearity and then compensating for the nonlinearity through inversion is another approach that has been researched [6, 31, 41]. However, we are not aware if it has been incorporated into an existing AFM.

Fig. 2.6 (a) illustrates a $13\ \mu\text{m}$ displacement in the x axis of a piezoelectric tube scanner when driven by a 5 Hz triangular wave voltage signal in open loop. It should be noted that the $13\ \mu\text{m}$ displacement is about 10 % of the scanner maximum scan range. The figure illustrates, the scanner's displacement deviations from linear due to the effect of hysteresis. In Fig. 2.6 (b), the scanner's displacement is plotted against the reference signal to form a hysteresis curve. The hysteresis level can be quantified from this curve by taking the maximum vertical divergence between the forward and reverse curve as a percentage of the scanner's displacement. In this case, the hysteresis is about 8.5 %. Fig. 2.6 (c) illustrates an AFM image of a calibration grating surface topography that features arrays of cubes obtained using the same scanner at 5 Hz scan frequency. It can be observed from this image that the presence of nonlinearity in the x axis scan has caused the features of the calibration grating along the x axis to appear curved.

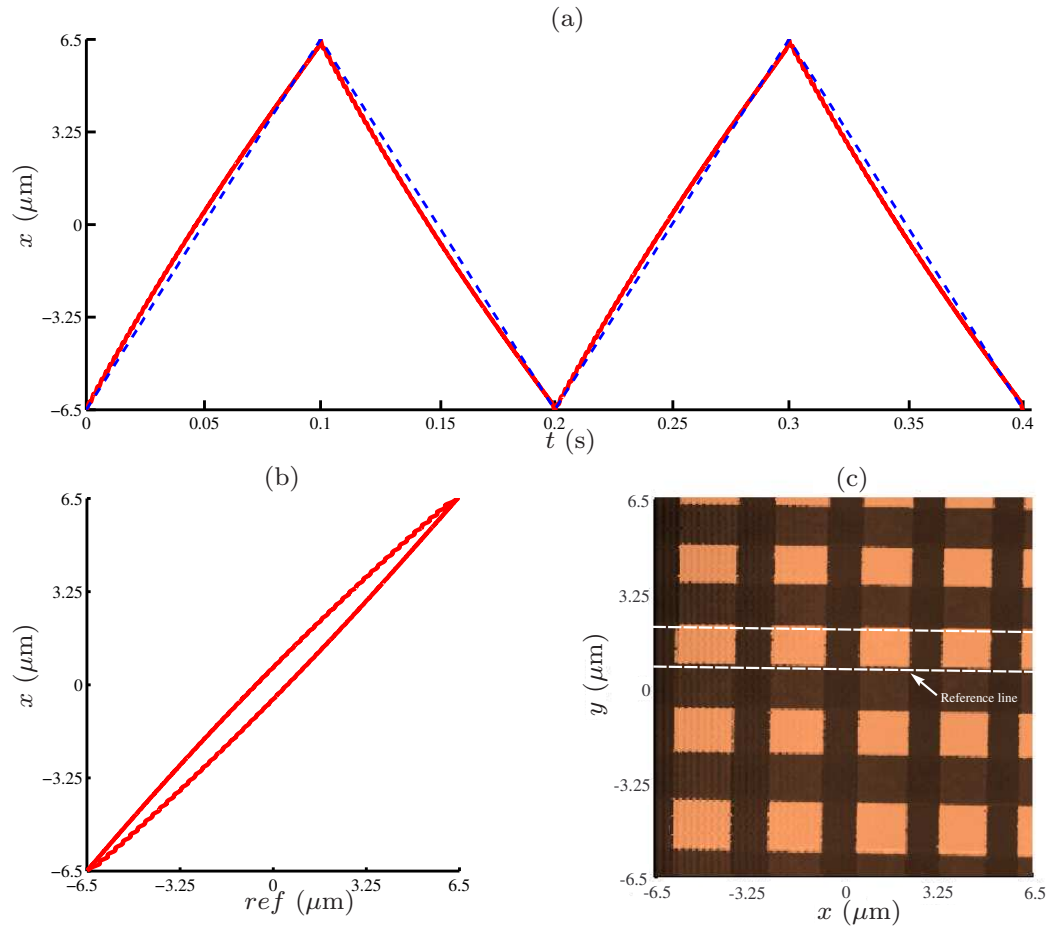


Figure 2.6 : The effect of hysteresis on the piezoelectric tube scanner when driven by a voltage source. (a) Measured scanner's displacement (solid line) due to 5 Hz triangular wave input signal (dashed line). (b) Hysteresis curve illustrating the relationship between the scanner's displacement and the reference input signal. (c) The resulting surface topography image of a calibration grating obtained using the same piezoelectric tube scanner.

2.5.2 Creep

The positioning precision of the piezoelectric tube scanners can also be significantly affected by creep, especially when positioning is required over extended periods of time [16, 23]. In piezoelectric tube scanners, when the applied voltage signal goes through an abrupt change such as a step change, the scanner experiences two stages of dimensional change. In the first stage, the scanner undergoes an instantaneous dimensional change within less than a millisecond. In the second stage, after the input voltage change has completed, the scanner continues to undergo a relatively smaller dimensional change in the same direction but at a much longer time scale. This slow dimensional change behavior in the second stage is known as creep [55]. In AFM imaging, especially during slow operation of atomic force microscopes, the effects of creep can result in significant distortions in the generated image [62]. Creep exacerbates the effect of hysteresis at the turning point of the scanning trajectory, and it has an adverse effect on the vertical positioning of the sample. While a number of methods have been proposed to deal with this phenomenon [16, 35, 66], the most widely used approach in earlier AFMs has been to allow sufficient time for the effect of creep to disappear after each abrupt change of the applied voltage signal or by always performing fast scans. However, these methods are not always practical and possible.

Figs. 2.7 (a)-(d) illustrate the effect of creep on AFM images of a calibration grating generated successively. These images were generated at a 2 Hz scan frequency and 256×256 image resolution. Before these images were generated, the scanner was applied with a voltage step corresponding to $4 \mu\text{m}$ displacement in each axis to offset the scanner to $(-4 \mu\text{m}, -4 \mu\text{m})$. Fig. 2.7 (a) shows that due to creep, the features of the calibration grating were imaged at uneven magnifications. This image distortion occurred because during scanning, although the reference signals have directed the scanner to move in a raster pattern, the scanner continued moving in the direction of the applied voltage step. As a result of this, certain areas of the grating were scanned more than once and consequently causing that part of the calibration grating to appear larger. Figs. 2.7 (b)-(d) show that the

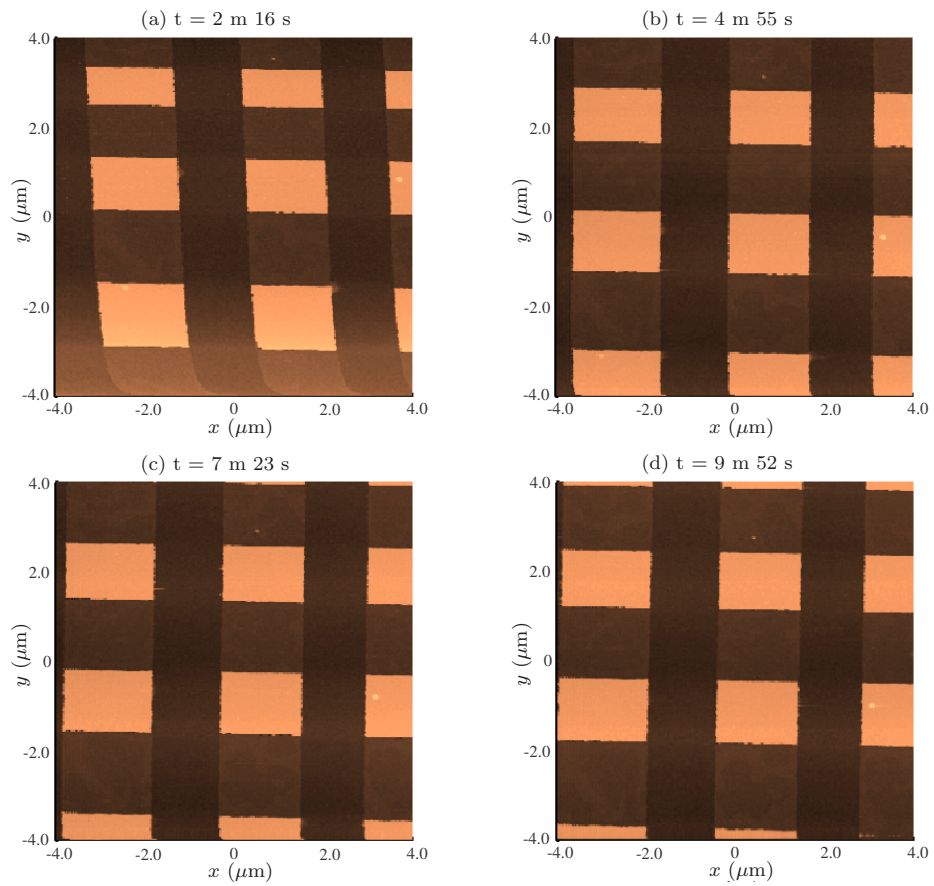


Figure 2.7 : Successive AFM images of a calibration grating taken after the scanner was applied with a step voltage to offset each axis of the scanner by $4\text{ }\mu\text{m}$. The images was scanned horizontally with the image origin at bottom-left of each image.

image distortion decreased as the effect of creep diminished with time. After about 10 minutes, Fig. 2.7 (d) illustrates the features of the calibration grating were imaged at an approximately equal magnification.

2.5.3 Vibrations

The main source of vibrations in a piezoelectric tube scanner is scan-induced vibrations due to excitation of its lightly damped first resonant mode by higher harmonics of the triangular wave signal. In an AFM, in order to perform a high-speed scan, a high frequency triangular wave signal needs to be used. A triangular wave signal contains all odd harmonics of the fundamental frequency. The amplitudes of these harmonic signals attenuate as $\frac{1}{n^2}$, with n being the harmonic number [37]. If a fast triangular waveform is applied to the scanner, it will inevitably excite the mechanical resonance of the scanner. Consequently, this causes the scanner to vibrate and trace a distorted triangular waveform which can significantly distort the generated AFM image. To avoid this complication, the scan frequency of AFMs is often limited to about 10 to 100 times lower than the scanners first resonance frequency [16]. During fast scans, a widely used approach to deal with this issue is to shape the tracking signal such that it does not excite the tube's resonance [16,42]. A downside of this approach is that the tube is still mechanically very lightly damped, and thus susceptible to external disturbances and noise.

Fig. 2.8 (a) illustrates the effect of the scan-induced vibrations on a scanner's displacement when driven by 10 Hz triangular wave signals. This figure shows that instead of following a perfect triangle, the scanner traced a distorted triangular waveform. The distortion in the scanner's displacement was due the excitation of the scanner's first resonant mode which is at about 580 Hz by the higher harmonics of the triangular wave signal. Figs. 2.8 (c) illustrates an AFM image of a calibration grating generated at 10 Hz scan frequency. This figure shows that the distortion in the scanner's displacement has resulted in a ripple-like artifact in the AFM image. Figs. 2.8 (b) and (d) illustrate that the distortions due

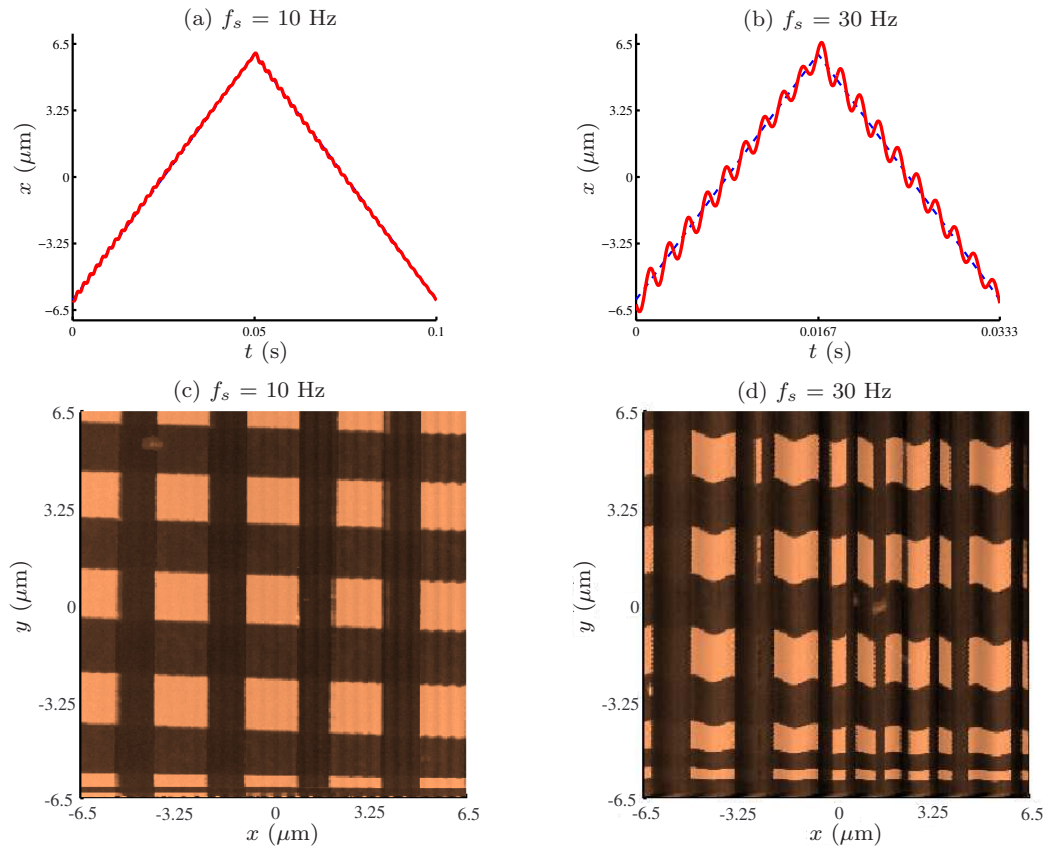


Figure 2.8 : The effect of scan-induced vibration on piezoelectric tube scanner. Scanner's displacements (solid line) when driven by (a) 10 Hz and (b) 30 Hz triangular wave signals (dashed line). AFM images of a calibration grating generated at scan frequency of (c) 10 Hz and (d) 30 Hz.

to the effect of the scan-induced vibration exacerbated when the frequency of the triangular wave signal was increased to 30 Hz. This is because at a higher scan frequency, the amplitude of the harmonics which excite the scanner's first resonant mode are larger. It should be noted that the scanner's displacements and the AFM images shown in Figs. 2.8 (a) - (d) were generated using a scanner driven by a charge source [25, 26] instead of a voltage source. The use of a charge source explains the reduction in the effect of hysteresis seen in Figs. 2.8 (a) and (c). A more detailed discussion on the use of charge source to reduce the effect of hysteresis in piezoelectric tube scanner will be presented in subsequent chapters.

2.6 Summary

In this chapter the working principle of AFM and its various operating modes were presented. This was subsequently followed by an in depth description of an important component in AFMs, i.e., the piezoelectric tube scanner. Then, this chapter continued to discuss in detail the effects of hysteresis, creep and scan-induced vibration on the positioning precision of the piezoelectric tube scanner. It was pointed out that as a result of these effects, the scanner's positioning precision deteriorates when the scanner is used for high speed AFM and long scanning range operations. In the following chapters, we will focus on the use of feedback control approaches to increase the scanner's positioning precision in high-speed AFM. Feedback controllers will be designed to achieve high closed-loop bandwidth as well as to compensate the effects of hysteresis, creep and scan-induced vibration.

Chapter 3

Feedback Control of a Piezoelectric Tube Scanner using Complementary Sensors

This chapter describes the use of a feedback control approach to achieve high-speed and high-precision positioning in a piezoelectric tube scanner by compensating the effects of hysteresis, creep and scan-induced vibration. In this chapter, we design a feedback controller for the fast-axis (x axis) of a scanner. The feedback controller is designed to utilize capacitive sensor and low-noise strain voltage signal induced in the scanner's free electrode to provide low-frequency and high-frequency measurements of the scanner's displacement respectively. The capacitive sensor's bandwidth is kept low in order to reduce the capacitive sensor noise that is detrimental for applications which require subnanometer positioning accuracy such as atomic resolution AFM imaging. The use of strain voltage signal allows the closed-loop bandwidth to be increased greater than the bandwidth of the capacitive sensor to achieve high-speed scans. In the first section of this chapter, a review of existing feedback and feedforward control techniques, and the motivation for this work are presented. Section 3.2 provides a description of the experimental setup. Modeling and identification of the system transfer functions are presented in Section 3.3. Control schemes are devised in Section 3.4. In Section 3.5, simulation and experimental results are presented to illustrate the effectiveness of the proposed control schemes.

3.1 Introduction

There has been a consistent effort in recent years to improve accuracy and speed of piezoelectric tube scanners using feedback control techniques. One of the earliest attempts to control a piezoelectric tube actuator is reported in [75], where a non-contacting inductive

sensor was used to measure the lateral displacement of a tube. Lag-lead and H_∞ controllers were designed and implemented on the tube, and the feasibility of reducing the adverse effects of creep and hysteresis were demonstrated. The authors also reported that the H_∞ controller achieved damping of high-frequency vibrations. The use of loop shaping procedure to design a feedback controller for a piezoelectric tube actuator instrumented with optical displacement sensors to track a raster pattern was described in [17]. Their results show reductions in tracking error and cross coupling due to the use of feedback control. In [39], a *proportional-plus-derivative* (PD) high-gain feedback controller and a feedforward input were used to compensate for creep, hysteresis, and vibration effects in an AFM piezoactuator system. The high-gain feedback controller was first used to linearize the piezoactuator by compensating for the creep and hysteresis. Then, the linearized piezoactuator was modeled to determine the feedforward input to account for the vibration effects. Their results indicated that, the use of feedforward input reduces the tracking error more as compared to using only feedback control. Examples of other successful applications of feedback include [20, 40, 65, 67, 78]. A comprehensive review of the field can be found in [18].

The key idea associated with feedback-based methods is to damp the first resonant mode of the piezoelectric tube actuator. This “flattening” of the frequency response of the scanner will allow tracking of a faster triangular waveform, and consequently a faster scan. Furthermore, to achieve accurate positioning at high frequencies and minimize the adverse effect of hysteresis, the feedback gain is often chosen to be high. There is a limit on how high the feedback gain can be made before the closed-loop system is made unstable, since the existence of sharp resonant peaks in the frequency response of the actuator typically results in a very low gain margin [5]. Using notch filters in the feedback loop has been shown to result in an improvement in the achievable gain margin [38].

The use of high-gain feedback for accurate tracking is necessitated due to the hysteretic

nature of the piezoelectric actuator. If the actuator is driven by a charge source, the hysteresis is significantly reduced, resulting in an almost linear actuator, a fact that has been known since early 1980s [15, 56]. However, until very recently, it has been rarely used due to the difficulties associated with driving highly capacitive loads with commercially available charge or current amplifiers. Recently, in [24–26, 28, 77] a new construction for charge and current sources capable of regulating the DC profile of the actuator have been proposed. A similar charge source is used here to actuate a prototype piezoelectric tube scanner.

Inversion-based feedforward method has also been applied to piezoelectric tube actuators. An attractive feature of feedforward control scheme is that this method does not require any additional sensors for implementation. Model-based inversion approach was used in [16] to compensate for positioning distortions caused by creep, hysteresis, and induced vibrations. A low-order feedforward controller was presented in [69] to suppress the lateral oscillation of a piezoelectric tube scanner. The feedforward controller was designed using H_∞ method such that the system is not excited at frequencies around the first resonance of the piezoelectric tube scanner. The performance of feedforward control schemes heavily relies on an accurate model of the system [16, 69]. Combining feedback and feedforward compensation has been shown to result in satisfactory tracking in a piezoelectric tube scanner in presence of parameter uncertainties in the plant model [3, 8, 9].

In applications where ultrahigh-precision positioning is a necessity, e.g., in AFM, the performance of feedback control scheme is severely limited by the noise properties of the displacement sensor. To appreciate this, consider a displacement sensor that has an RMS noise of $20 \text{ pm}/\sqrt{\text{Hz}}$ - most capacitive and inductive displacement sensors are subject to this level of noise. If the sensor is operated over a bandwidth of, say 10 kHz, its RMS noise will be 2 nm, which makes it impossible to achieve subnanometer positioning accuracy. However, if the very same sensor is operated over a bandwidth of 100 Hz, the noise level

is reduced to 2 \AA , about the radius of an atom. Limiting the bandwidth to 1 Hz , would further reduce this noise level to 0.2 \AA . Thus, the positioning accuracy achievable by a feedback controller can be significantly improved. However, this would also limit the operating bandwidth of the feedback controller, resulting in very slow closed-loop operation of the system. Such a severe closed-loop bandwidth limitation would come at the additional cost of making the closed-loop system sensitive to vibration, noise and other disturbances.

The contribution of this chapter is the utilization of the piezoelectric voltage induced in one of the two electrodes as an additional displacement sensor. Although this signal cannot be used to measure static deflections of the tube, and it has a poor low-frequency response, it can function as an excellent high-frequency displacement sensor, with a noise level of at least three orders of magnitude less than a capacitive sensor. Thus, for all practical purposes, this sensor can be viewed to be almost free of noise. A controller can be designed to achieve satisfactory tracking using these two “complementary” sensors. Here, a two-input one-output H_∞ controller is designed to use the capacitive sensor measurements at low frequencies (below 100 Hz), and at DC, and the piezoelectric strain signal at higher frequencies. For roughly the same noise level, the controller achieves a closed-loop bandwidth more than three times that obtained from a controller utilizing the capacitive sensor measurement alone.

3.2 System Description

The piezoelectric tube used in this work is a cylindrical tube made of piezoelectric material plated with a layer of electrode on the inner and outer surfaces of the tube. The inner electrode is continuous and grounded. The outer layer electrode is segmented into four equal sized electrodes and referred individually as $+x$, $-x$, $+y$ and $-y$ electrodes. The physical dimensions of the tube are given in Fig. 3.1. The piezoelectric tube is housed in a circular aluminum enclosure to protect it from external disturbances and acoustic noise. A hollowed aluminum cube is glued to the top of the tube to serve as a sample holder and

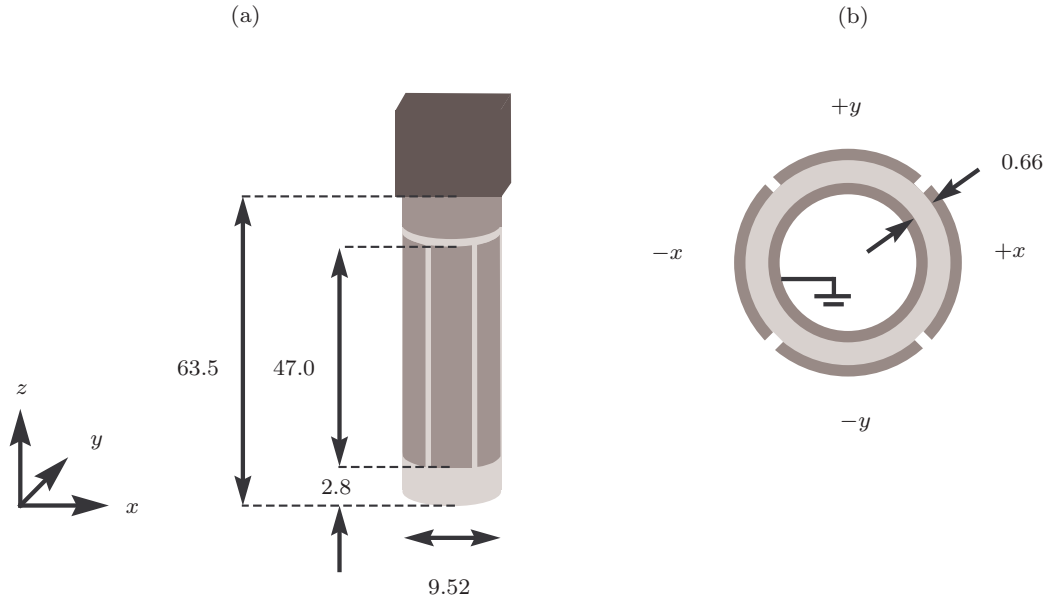


Figure 3.1 : Piezoelectric tube dimensions in millimeters. (a) Isometric-view and (b) Bottom-view (dimensions are not to the scale and the thickness of the electrode is exaggerated).

also to provide the capacitive sensors (ADE Technologies 2804) flat surfaces so that the tip deflection can be measured accurately. The capacitive sensors are fixed at right angles to the cube surface in the x axis and y axis by using nylon screws as shown in Fig. 3.2. The capacitive sensors have a sensitivity of $10 \mu\text{m}/\text{V}$ over a range of $\pm 100 \mu\text{m}$. The RMS noise density of the capacitive sensors were measured in [30] to be $17.5 \text{ pm}/\sqrt{\text{Hz}}$. Each of the capacitive sensors is driven by an ADE Technologies 4810 gaging system that comes with multiple bandwidth settings. By operating the sensor over a bandwidth of 100 Hz, the RMS noise or the resolution of the capacitive sensor is set to 0.175 nm.

In most nanoscale positioning applications, including in most AFMs, the tube motion is produced by applying equal and opposite sign input signals to the electrodes opposite to each other. However, in this work only the $+x$ electrode is used to produce the forward and reverse motions of the tube in the x axis. This is achieved by applying a triangular wave

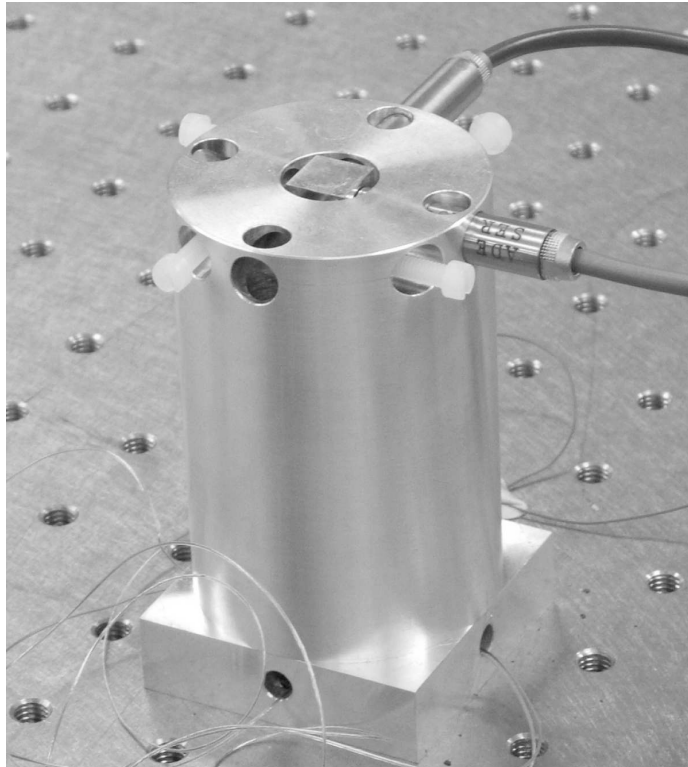


Figure 3.2 : The piezoelectric tube is housed in a circular aluminum enclosure.

signal to this electrode. The opposite electrode $-x$ is used as a secondary sensor to measure the tip deflection. Note that this arrangement reduces the scan range of the tube to half. However, it results in a substantially higher positioning accuracy, as articulated shortly. If needed, a larger scan range can be obtained by utilizing a tube of different dimensions.

When the tube deflects, the piezoelectric strain voltage induced in the $-x$ electrode is found to be proportional to the tip deflection over a certain frequency range. The transfer function from the strain voltage to the output of an instrumentation amplifier resembles a first-order high-pass filter, [53]. This is due to the capacitive nature of the piezoelectric tube. The high-pass filter can be expressed as,

$$G_{hp}(s) = \frac{s}{s + \frac{1}{R_{in}C_p}} \quad (3.1)$$

where R_{in} is the input impedance of the voltage measuring instrument and C_p is the capacitance of the piezoelectric tube.

The RMS noise density of the piezoelectric strain voltage was measured in [29, 30] to be $16 \text{ fm}/\sqrt{\text{Hz}}$, about a thousand times less than that of the capacitive sensor. Such an extremely low-noise level will only cause a few picometers of RMS noise over a bandwidth of tens of kHz. By this measure, this should be the preferred displacement sensor. However, due to its high-pass nature, as articulated above, accurate positioning at low frequencies using this sensor alone is impossible. At low frequencies where the strain signal cannot be used, the displacement measurement obtained from the capacitive sensor can be used directly. The complementary nature of the two measurements allows for the bandwidth of the capacitive sensor to be made very low, thus reducing the overall effect of noise on the controlled position of the scanner to an absolute minimum.

The schematics of the proposed feedback control scheme are illustrated in Fig. 3.3. The $+x$ electrode is being driven by a home-made charge source [25, 26] that renders the plant linear, hence reducing the adverse effect of hysteresis. The charge amplifier has a constant

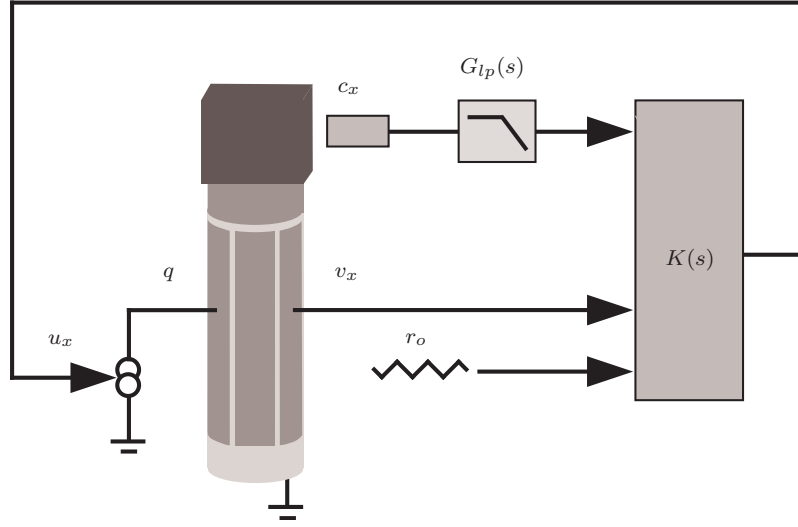


Figure 3.3 : Schematics of the proposed feedback control system.

gain of 68 nC/volt. The two-input-one-output controller is designed to take advantage of the complementary nature of the two measurement signals. Details of the design are explained in Section 3.4. A dSPACE DS1103 controller board equipped with a 16-bit analog-to-digital converter (ADC)/digital-to-analog converter (DAC) cards was used for real-time controller implementation. A sampling frequency of 15 kHz is used to avoid aliasing. In order to reduce the quantization noise, a low-noise preamplifier with a gain of 10 is used to amplify the capacitive sensor output so that it occupies the full range of the ADC card for a range of $\pm 10 \mu\text{m}$.

3.3 System Identification

This section discusses and details the modeling procedures undertaken in this work. The following frequency response functions (FRFs) were determined using a dual channel HP35670A spectrum analyzer,

$$G_{v_x u_x}(i\omega) = \frac{v_x(i\omega)}{u_x(i\omega)} \quad (3.2)$$

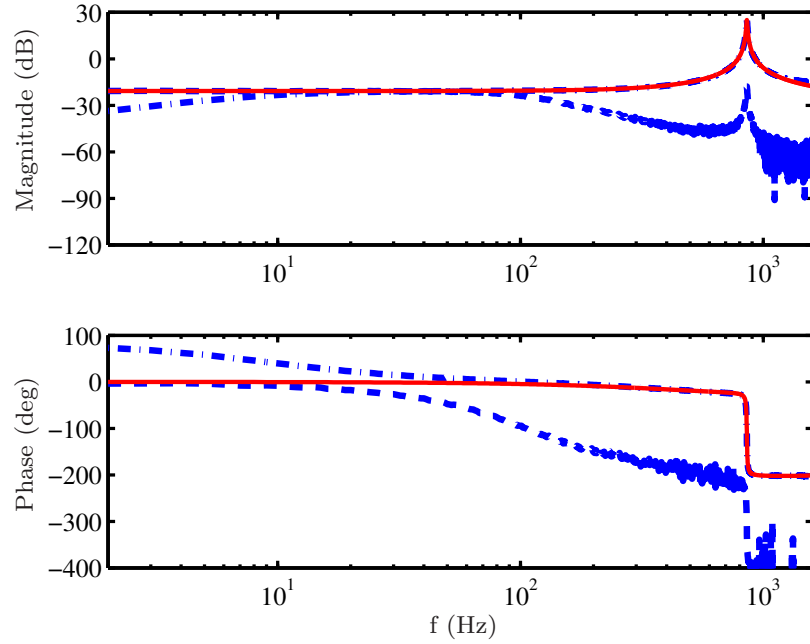


Figure 3.4 : One-loop-frequency responses, $G_{v_x u_x}(i\omega)$ (dash-dots), $G_{c_x u_x}(i\omega)$ (dash), and the identified model $G_{y_x u_x}(s)$ (solid).

and

$$G_{c_x u_x}(i\omega) = \frac{c_x(i\omega)}{u_x(i\omega)} \quad (3.3)$$

where u_x is the input voltage to the charge amplifier, v_x is the induced piezoelectric strain voltage and c_x is the output voltage of the capacitive sensor. The subscript x denotes that the actuation and measurements were performed along the x axis. A band-limited random noise signal (1 Hz to 1600 Hz) was generated using the spectrum analyzer and applied to the charge amplifier as the input, u_x . The corresponding outputs v_x and c_x were also recorded using the same device. The input-output data was processed to generate the FRFs of (3.2) and (3.3) in a non-parametric form as illustrated in Fig. 3.4.

It can be seen from Fig. 3.4 that $G_{v_x u_x}(i\omega)$ includes a high-pass filter with cutoff frequency of about 9 Hz. The high-pass filter results in a phase-lead and heavy attenuation of the strain voltage signal at low frequencies. Thus, the strain voltage cannot be used as a

reliable tip deflection measurement at low frequencies. Nevertheless from about 20 Hz and onwards, the strain voltage provides an excellent signal that can be used to estimate the tip deflection and also the dynamics of the piezoelectric tube. As for $G_{c_x u_x}(i\omega)$, its frequency response includes a low-pass filter with cutoff frequency of 100 Hz. Thus, the capacitive sensor can be used to measure the tip deflection below 70 Hz with acceptable accuracy. After this frequency, $G_{c_x u_x}(i\omega)$ starts to roll off considerably. These two measurements complement each other since the former is accurate at high frequencies, including at the resonance and the latter is reliable at low frequencies, including at DC. Note that a scaling factor of $K_a = 0.2$ has been incorporated into the $G_{v_x u_x}(i\omega)$ to adjust the sensitivity of the signal obtained from $-x$ electrode and make it identical to that of the capacitive sensor signal.

In this work, instead of fitting separate transfer functions to $G_{v_x u_x}(i\omega)$ and $G_{c_x u_x}(i\omega)$, a new FRF was formed by using the low-frequency range (1 Hz to 50 Hz) of the $G_{c_x u_x}(i\omega)$ data and the high frequency range (51 Hz to 1600 Hz) of the $G_{v_x u_x}(i\omega)$ data. The new FRF corresponds to the deflection of the tip, y_x that is not affected by artifacts such as the high-pass property of the strain signal, or the low-pass property of capacitor sensor measurement. A second order model was fitted to the new FRF data. The identification algorithm used for this purpose was the frequency-domain subspace-based system identification approach described in [47] and [48]. The following model was found to be a good fit as illustrated in Fig. 3.4,

$$G_{y_x u_x}(s) = \frac{-0.06s^2 - 342.8s + 2.654 \times 10^6}{s^2 + 49.47s + 2.895 \times 10^7}. \quad (3.4)$$

The high-pass and the low-pass filter characteristics corresponding to $G_{v_x u_x}(i\omega)$ and $G_{c_x u_x}(i\omega)$ respectively are fitted with the following models

$$G_{lp}(s) = \frac{3.948 \times 10^5}{s^2 + 888.6s + 3.948 \times 10^5} \quad (3.5)$$

and

$$G_{hp}(s) = \frac{s}{s + 55.29}. \quad (3.6)$$

3.4 Controller Design

This section discusses and details the H_∞ control design schemes proposed in this chapter. The key objectives of the design are as follows:

- 1) To achieve good damping ratio for the first resonant mode of the piezoelectric tube scanner,
- 2) To achieve higher tracking bandwidth using the low-bandwidth capacitive sensor and the piezoelectric strain voltage signal as the primary and secondary displacement measurements respectively,
- 3) To minimize the effect of low-frequency vibrations on the tube's deflection.

For the sake of comparison, a second controller using only the measurements obtained from the capacitive sensor is also designed to achieve the abovementioned objectives as much as possible.

3.4.1 Two-sensor-based H_∞ controller

The proposed control diagram is illustrated in Fig. 3.5 where a two-degree-of-freedom (DOF) controller scheme is to be synthesized. The control structure consists of the feed-forward controller, $K_{fd}(s)$ and the feedback controllers $K_v(s)$ and $K_c(s)$. The feedback controllers are first designed. Fig. 3.6 illustrates the feedback control block diagram with incorporated weighting functions. The problem can be cast into the standard H_∞ controller design framework as shown in Fig. 3.7. The exogenous input vector is defined as

$$w = \begin{bmatrix} r \\ d_i \\ n \end{bmatrix}$$

and the exogenous output as

$$z = \begin{bmatrix} z_1 \\ z_2 \end{bmatrix},$$

where r is the reference signal to be tracked, d_i represents low-frequency vibrations modeled as an input disturbance, and n represents the sensor noise. Furthermore, u_x is the control signal and v is the measured output. From Fig. 3.6 it is clear that

$$z_1 = W_1 \left(r - G_{y_x u_x} (u_x + W_{bp} d_i) \right),$$

and

$$z_2 = W_2 u_x.$$

The control signal is u_x and v is the vector of measured outputs

$$v = \begin{bmatrix} v_1 \\ v_2 \end{bmatrix},$$

where

$$v_1 = r - \left(G_{y_x u_x} (u_x + W_{bp} d_i) G_{lp} + W_{hp} n \right)$$

and

$$v_2 = r - \left(G_{y_x u_x} (u + W_{bp} d_i) G_{hp} + W_{lp} n \right).$$

To achieve satisfactory vibration reduction at low frequencies, a disturbance d_i has been introduced at the input of the plant and the controller is forced to minimize $T_{y_x d_i}$, the transfer function from the input disturbance d_i to the actual scanner output y_x . The weighting function W_{bp} is tuned to the resonance frequency of the tube that is located in the vicinity of 850 Hz, as shown in Fig. 3.4 and is chosen as,

$$W_{bp}(s) = \frac{1793s}{s^2 + 1793s + 2.893 \times 10^7}. \quad (3.7)$$

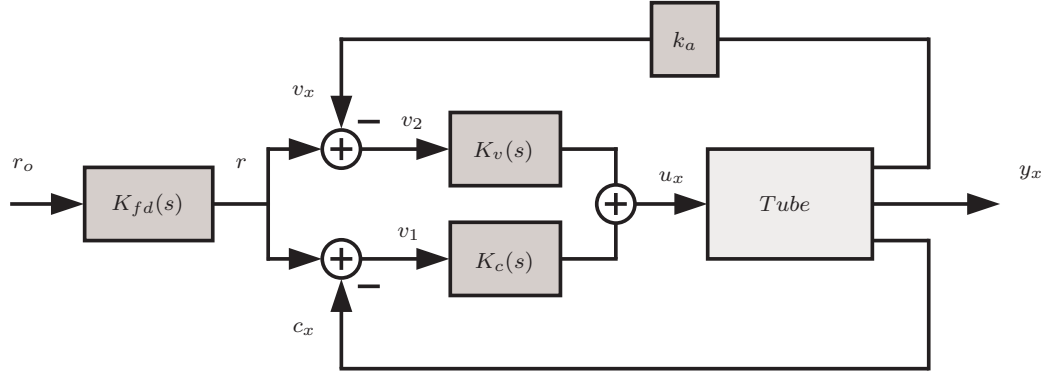


Figure 3.5 : 2-DOF control block diagram.

The capacitive sensor is noisy at high frequencies and the piezoelectric stain voltage signal is distorted at low frequencies. The controller is designed to utilize the capacitive sensor for tracking low-frequency signals, and the strain voltage for tracking signals that contain higher frequency components. This is achieved by introducing the two weighting functions W_{hp} and W_{lp} , as shown in Fig. 3.6, as

$$W_{lp}(s) = \frac{1.262 \times 10^8}{(s^2 + 195.9s + 1.124 \times 10^4)(s^2 + 81.13s + 1.124 \times 10^4)} \quad (3.8)$$

and

$$W_{hp}(s) = \frac{s^2}{s^2 + 1571s + 1.579 \times 10^6}. \quad (3.9)$$

Furthermore, $W_2 = 0.1$ is used to impose a constraint on the control signal. This is to avoid excessively large control signals that could saturate the actuator.

The weighting function W_1 is incorporated to enforce good tracking performance. The inverse of this transfer function can be considered as the desired sensitivity transfer function T_{er} , the transfer function from reference signal r to the tracking error $e = r - y_x$. W_1 is chosen as

$$W_1(s) = \frac{0.3162s + 1257}{s + 1.257}. \quad (3.10)$$

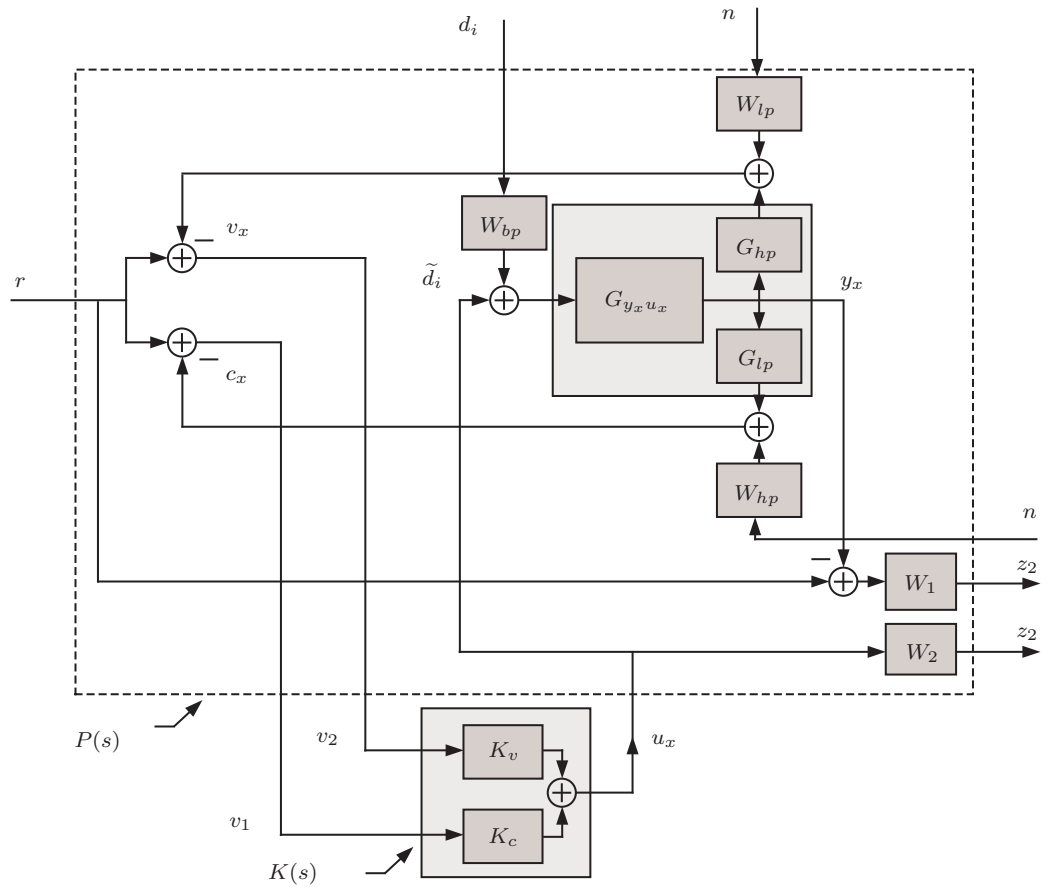


Figure 3.6 : Feedback control block diagram with weighting functions.

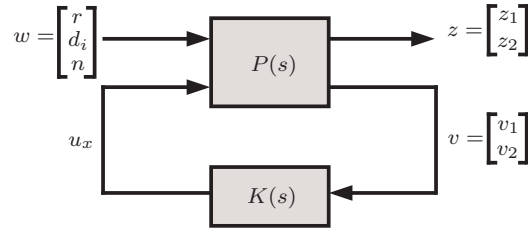


Figure 3.7 : General feedback control configuration.

Fig. 3.8 (a) illustrates the main weighting functions. To examine the effectiveness of the controller, the achieved sensitivity function $S(s)$ is plotted against the desired sensitivity function $W_1^{-1}(s)$ in Fig. 3.8 (b). The figure illustrates that both of the achieved and the desired sensitivity functions match closely except at high frequencies, particularly beyond 1 kHz. This indicates that the synthesized two-input one-output H_∞ controller performs as intended.

Fig. 3.9 plots the frequency responses of the feedback controllers $K_c(s)$ and $K_v(s)$. It can be observed that the two controllers conform to the design requirements. In particular, $K_c(s)$ is a high-gain controller at low frequencies within the bandwidth afforded by the capacitive sensor. On the other hand, $K_v(s)$ maintains a low gain within the bandwidth of the capacitive sensor, but applies a high gain beyond 20 Hz. This “frequency sharing” enables the two controllers to maintain satisfactory tracking of the reference signal over the bandwidth of interest.

The final stage of the controller synthesis involves designing the feedforward controller $K_{fd}(s)$ to shape the reference signal based on the achieved closed-loop frequency response,

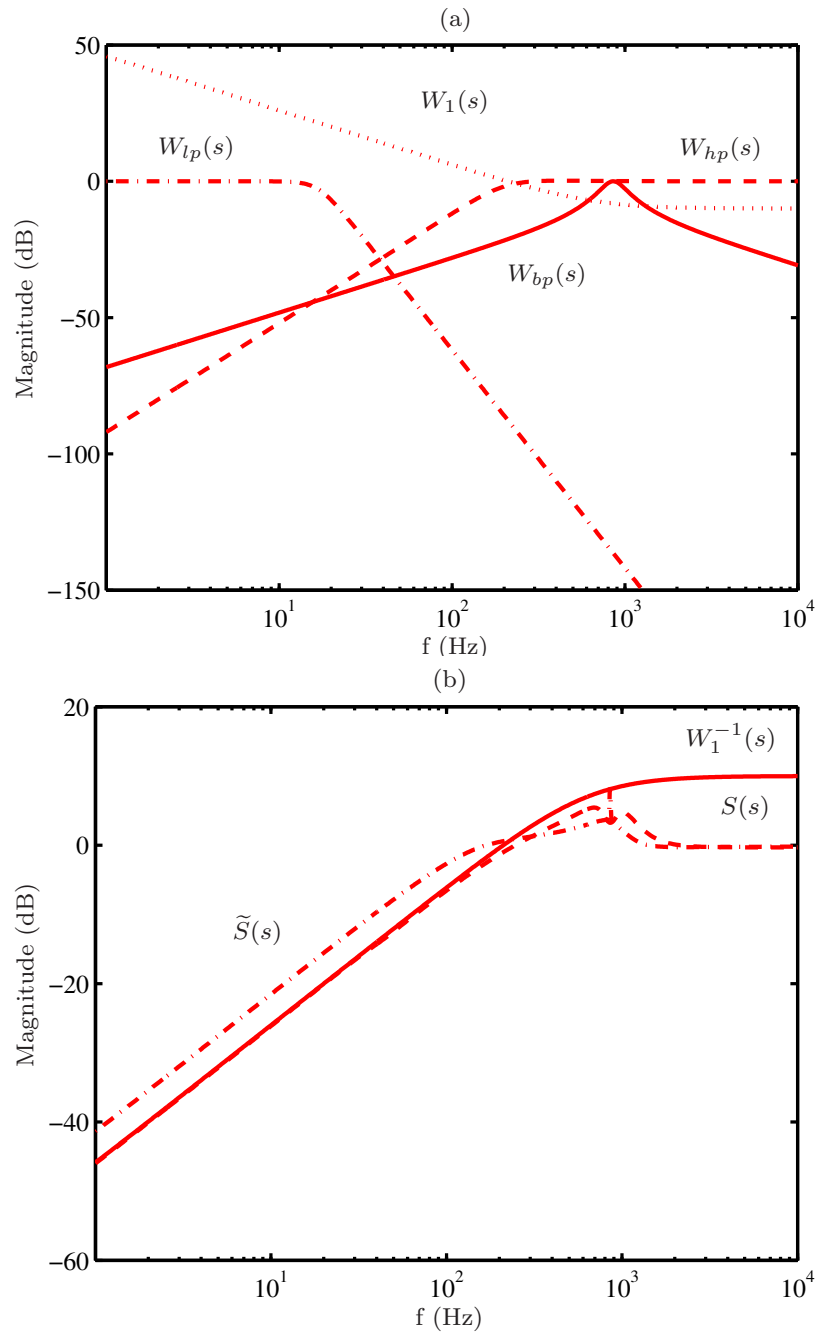


Figure 3.8 : (a) Weighting functions. (b) Sensitivity functions: desired (solid), achieved two-sensor (dash) and achieved single-sensor (dash-dot).

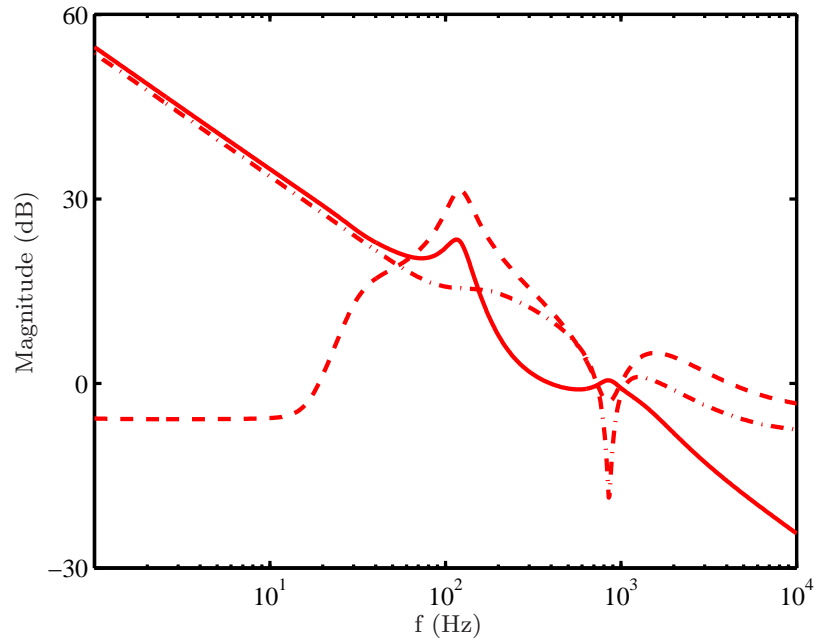


Figure 3.9 : Frequency response of the designed controllers $K_c(s)$ (solid), $K_v(s)$ (dash) and $\tilde{K}_c(s)$ (dash-dot).

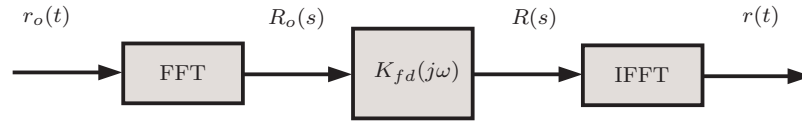


Figure 3.10 : Procedure to obtain shaped reference $r(t)$.

$T_{y_x r}(s)$. The feedforward controller should be chosen such that:

$$K_{fd}(s) \approx T_{y_x r}^{-1}(s). \quad (3.11)$$

Since the reference signal $r_o(t)$ is known and the frequency $T_{y_x r}(j\omega)$ can be measured in advance, the shaped reference signal $r(t)$ can be obtained off-line, as shown in Fig. 3.10. This inversion is generally done over the frequency range for which a satisfactory model of the closed-loop system is available, in this case up to 1600 Hz.

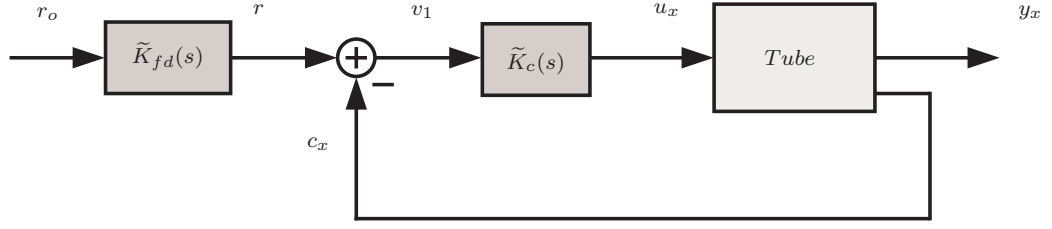


Figure 3.11 : 2-DOF control block diagram for the one-sensor-based H_∞ controller.

3.4.2 One-sensor-based H_∞ controller

The purpose of this section is to demonstrate the immediate benefit of using the strain voltage sensor in addition to the low-bandwidth capacitive sensor. The controller designed here utilizes only the low-bandwidth capacitive sensor to obtain the tip displacement measurement for feedback. To make a fair comparison with the two-sensor-based H_∞ controller, a 2-DOF controller, with a structure depicted in Fig. 3.11, was designed and implemented. Similar weighting functions (3.7)-(3.10) were used in synthesizing the H_∞ controller $\tilde{K}_c(s)$. The feedback control block diagram with the weighting functions is illustrated in Fig. 3.12. A feedforward controller $\tilde{K}_{fd}(s)$ was also designed and implemented in a similar manner as detailed in the previous section.

The achieved sensitivity function $\tilde{S}(s)$ for this control scheme is shown in Fig. 3.8(b). It can be observed that $\tilde{S}(s)$ does not match the desired sensitivity function $W_1^{-1}(s)$. This is a clear indication that a controller designed with one sensor alone is not capable of satisfying the design goals articulated before. Fig. 3.9 plots the frequency response of the feedback controller $\tilde{K}_c(s)$. This is rather similar to $K_c(s)$ with the clear exception that it includes a notch filter at the first resonance frequency of the tube.

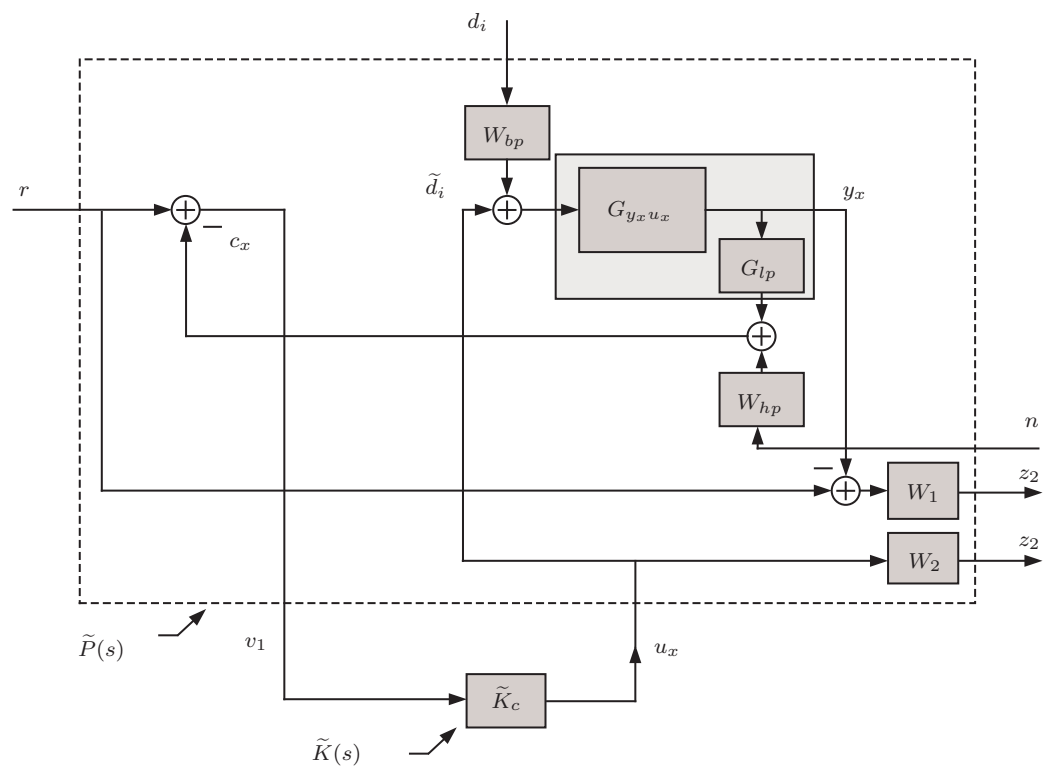


Figure 3.12 : Feedback control block diagram with weighting functions for the one-sensor-based H_∞ controller.

3.5 Results

This section presents experimental results obtained from the two control schemes proposed in this chapter. In order to measure the true deflection y_x , a capacitive sensor with a bandwidth of 10 kHz was used in all tests. The sensor's signal was passed through a second order Butterworth low-pass filter with a cut-off frequency of 100 Hz. This latter signal was made available to the feedback controllers $K_c(s)$ and $\tilde{K}_c(s)$. Note that this low-pass filter is implemented simultaneously with the feedback controllers using the same real-time rapid prototyping system. Therefore, it should be considered as an integral part of $K_c(s)$ and $\tilde{K}_c(s)$. Inclusion of a low-pass filter in this arrangement is not entirely necessary since $K_c(s)$ and $\tilde{K}_c(s)$ are designed to operate at low bandwidths. This filter is incorporated in the design to emphasize the fact that this methodology works fine even with a low-bandwidth (and thus inexpensive) displacement sensor.

3.5.1 Hysteresis reduction

The presence of hysteresis in the prototype scanner was investigated by applying a 5 Hz sinusoidal signal to the piezoelectric tube and measuring its deflection in open loop. A single-tone low-frequency signal was chosen here in order to avoid excitation of the first resonant mode of the tube. Also, this ensures that only the nonlinear component of the deflection is captured since at such a low frequency the linear dynamics of the tube resembles a simple gain with hardly any phase shift.

The tube was made to deflect a large distance ($\pm 3.0 \mu\text{m}$) so that the presence of hysteresis could be clearly observed. The effects of hysteresis were evaluated when the tube was driven by: 1) a voltage amplifier and 2) a charge amplifier. For each case the corresponding input signal and the tip deflection were recorded. Figs. 3.13 (a) and (b) illustrate the plots of tip deflection versus input signal for voltage and charge, respectively. A clear reduction of hysteresis can be observed when the tube is driven by the charge amplifier. In order to quantify the improvement, the presence of hysteresis was measured in terms of

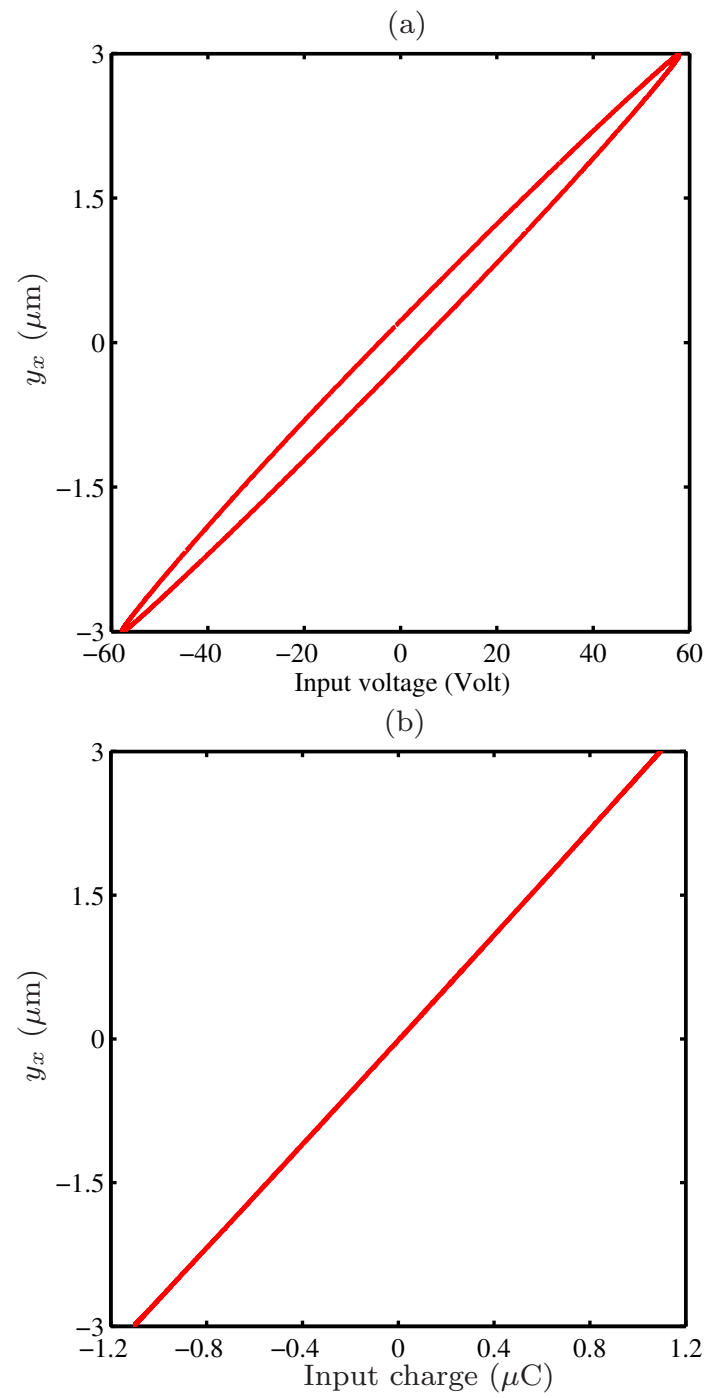


Figure 3.13 : Hysteresis plot of open-loop 5 Hz scan using (a) voltage amplifier and (b) charge amplifier.

Table 3.1 : Numerical quantification of hysteresis

Configurations	Max. output hysteresis	Max. input hysteresis
Voltage amp.	434.0 nm (7.2%)	8.5 volt (7.3%)
Charge amp.	23.2 nm (0.4%)	9.20 nC (0.4%)

the maximum (input and output) percentage deflection from a straight line. The results are tabulated in Table 3.1 and clearly demonstrate the immediate benefit of driving the tube with a charge amplifier. Although the hysteresis is not reduced to an absolute zero, it is made so small that the actuator can effectively be considered a linear device.

3.5.2 Closed-loop frequency response

The performance of the feedback two sensor-based controller was first evaluated by measuring the closed-loop frequency responses of the scanner using the spectrum analyzer. In Fig. 3.14, the closed-loop frequency responses, $T_{y_x r}(i\omega)$ and $T_{y_x \tilde{d}_i}(i\omega)$ are plotted along with the open-loop frequency response, $G_{y_x u_x}(i\omega)$. By inspecting the frequency response of $T_{y_x r}(i\omega)$ we conclude that the closed-loop system has a bandwidth of 310 Hz. Also, a damping of 20 dB at the first resonant mode is evident from the frequency response of $T_{y_x \tilde{d}_i}(i\omega)$. Note that, the frequency response also shows that, the closed-loop system is insensitive to low-frequency input disturbances. Hence, the closed-loop system will perform in a satisfactory manner in presence of low-frequency vibrations, and disturbances. Overall, the two-sensor-based controller satisfies all the performance criteria.

3.5.3 Time response

The ultimate purpose of the x axis feedback control loop is to allow for satisfactory tracking of a fast triangular wave trajectory. This is necessary if the actuator is to be used for fast AFM. First column of Fig. 3.15 plots the open-loop time responses of the scanner due to 5,

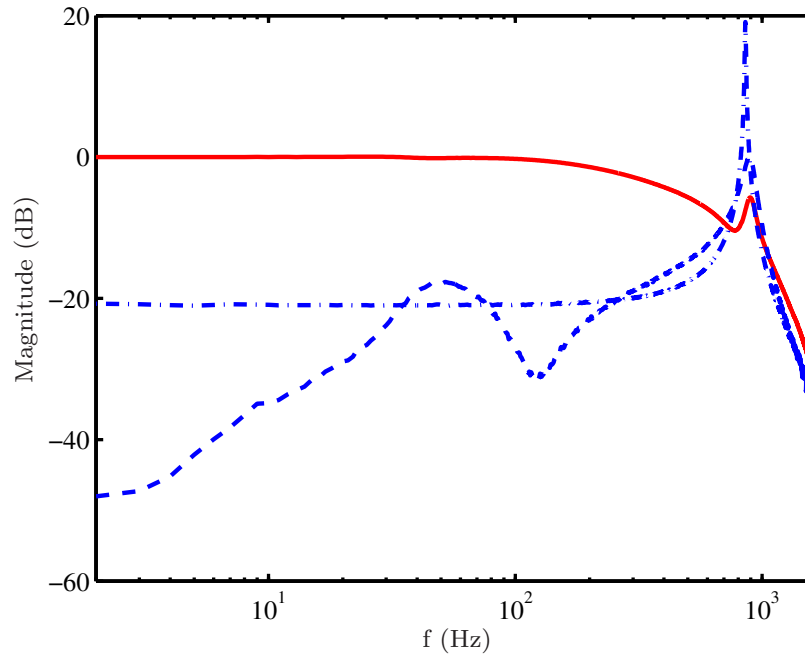


Figure 3.14 : Experimentally obtained frequency responses of $T_{yxr}(i\omega)$ (solid), $T_{y_x\tilde{d}_i}(i\omega)$ (dash) and $G_{y_xu_x}(i\omega)$ (dash-dots).

20 and 40 Hz triangular input signals. It can be observed that as the frequency of the input signal increases, the extent to which the scanner's motion becomes affected by the induced vibrations also increases. Particularly at 40 Hz the scanner's motion is badly affected by amplification of the 11th harmonic (840 Hz) of the triangular signal which is close to the first resonance frequency of the piezoelectric tube (about 850 Hz).

The right hand column of Fig. 3.15 (Figs. 3.15 (d), (e) and (f)) compares the closed loop response of the scanner under the two-sensor-based H_∞ controller with the desired trajectory. It can be observed that the controller successfully damps the induced vibrations and provides excellent tracking performance, particularly at low frequencies. The damping of 20 dB at the first resonant mode of the scanner is sufficient to avoid the amplification of the harmonics near the first resonance frequency. Note that the controller's ability to track the reference signal at its corners is reduced when the frequency of the input signal

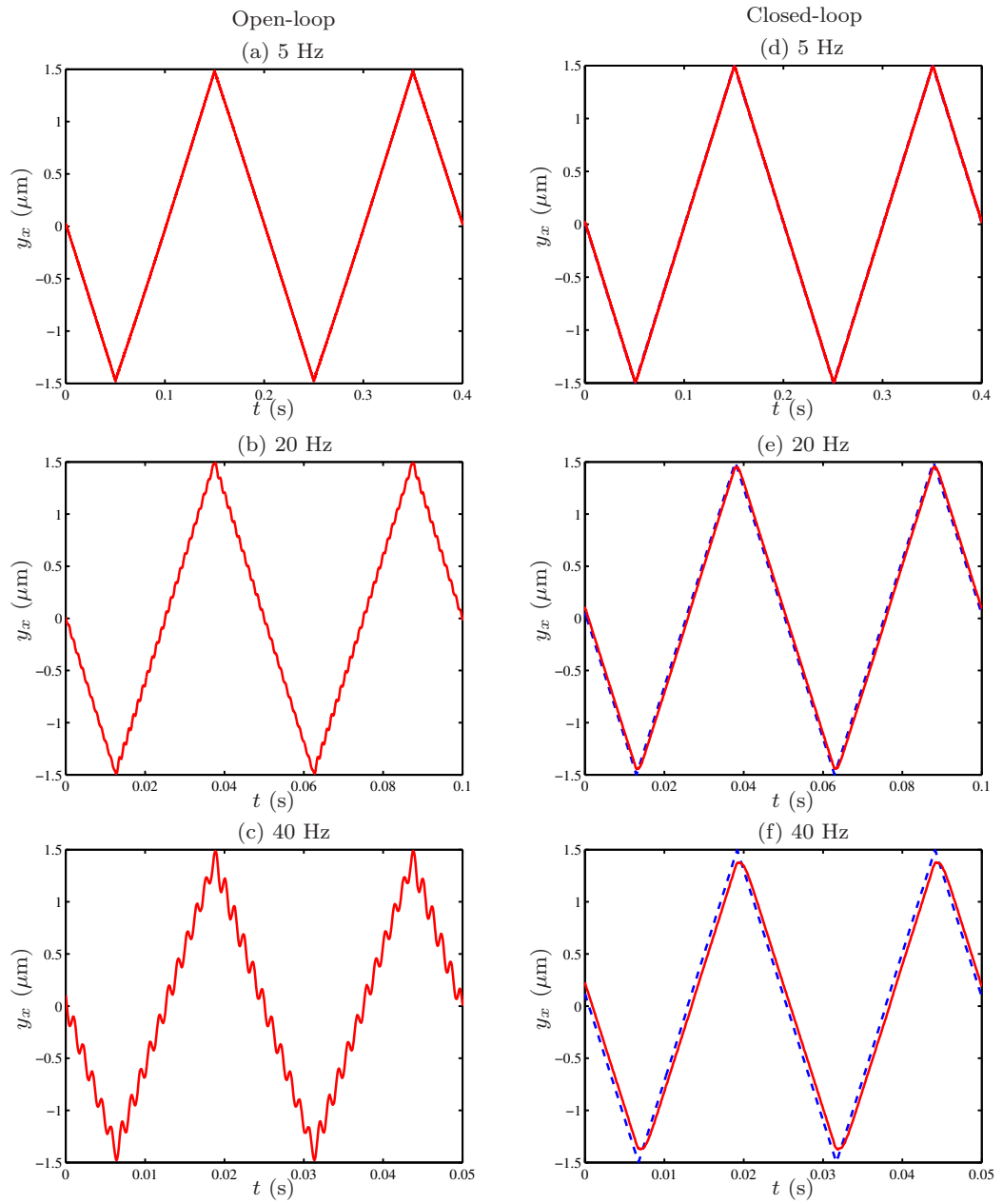


Figure 3.15 : Open-loop (left) and closed-loop (right) time response plots of 5, 20 and 40 Hz scan. Solid line is measured scanners displacement and dashed line is desired trajectory.

Table 3.2 : RMS values of tracking error

Scan Freq.	Open-loop	Closed-loop	
		Two-sensor	One-sensor
5 Hz	12.2 nm	1.9 nm	2.0 nm
10 Hz	9.9 nm	2.3 nm	2.4 nm
20 Hz	10.7 nm	3.2 nm	3.4 nm
30 Hz	17.5 nm	3.1 nm	9.1 nm
40 Hz	67.0 nm	7.6 nm	15.6 nm

is increased. This effect is clearly visible in Fig. 3.15 (f) and is mainly due to the limited closed-loop bandwidth of the system. The feedforward controller incorporated into the tracking system works to correct this effect. However, its effectiveness is limited by the accuracy of the closed-loop model used in the inversion. Nevertheless, this should not be viewed as a drawback as it is common practice in AFM to limit the image size to within a certain percentage of the available window with the understanding that, quite often, the image could be distorted around the edges.

Open-loop and closed-loop tracking errors for various scan frequencies are tabulated in Table 3.2. The tracking errors are determined by calculating the RMS difference between the measured displacement and the reference signal for 90 % of the scan range (ignoring the top and bottom 5 % of the scans). A fixed phase shift between the measured displacement and the reference input can be observed in Figs. 3.15 (d)-(f). In calculating the tracking errors, these phase shifts were removed. At the slow speed scan of 5 Hz the controller displays excellent tracking performance with tracking error of only 1.9 nm, i.e. 0.06 % of the entire scan range. The tracking error remains satisfactory even as the scan frequency is increased as high as 40 Hz, as shown in Table 3.2. The error does not exceed 0.25 % of the scan range. Note that in measuring the displacements, a high bandwidth capacitive sensor with a bandwidth of 10 kHz was used. At this bandwidth, the RMS noise level of the sensor

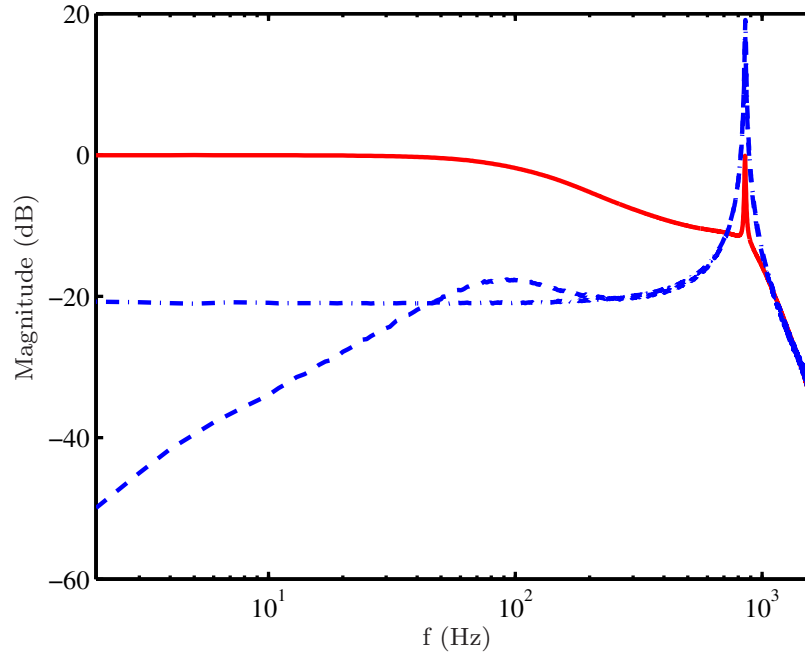


Figure 3.16 : Experimentally obtained closed-loop frequency responses using one-sensor-based H_∞ controller, $T_{y_x r}(i\omega)$ (solid), $T_{y_x d_i}(i\omega)$ (dash) and $G_{y_x u_x}(i\omega)$ (dash-dots).

is calculated to be 1.75 nm. The stochastic noise affecting the “true” output of the scanner is significantly lower than this, since the said noise is largely due to the capacitive sensor signal which is low-pass filtered at 100 Hz. The stochastic noise arising from the strain voltage signal can effectively be ignored in this case due to its extremely low noise density.

3.5.4 One-sensor-based H_∞ controller

For the sake of completeness closed-loop performance of the scanner with the one-sensor-based H_∞ controller is studied here. Fig. 3.16 illustrates closed-loop performance of this controller. It can be observed that the bandwidth of the closed-loop system is about a third of that of the two-sensor-based system. By comparing $T_{y_x \tilde{d}_i}(i\omega)$ and $G_{y_x u_x}(i\omega)$ in Fig. 3.16, it can be concluded that $\tilde{K}_c(s)$ does not damp the first resonance mode of the tube in a satisfactory manner. This is of little surprise since this mode is out of the 100 Hz bandwidth of the controller. However, no induced vibrations are observed when the tube is made to

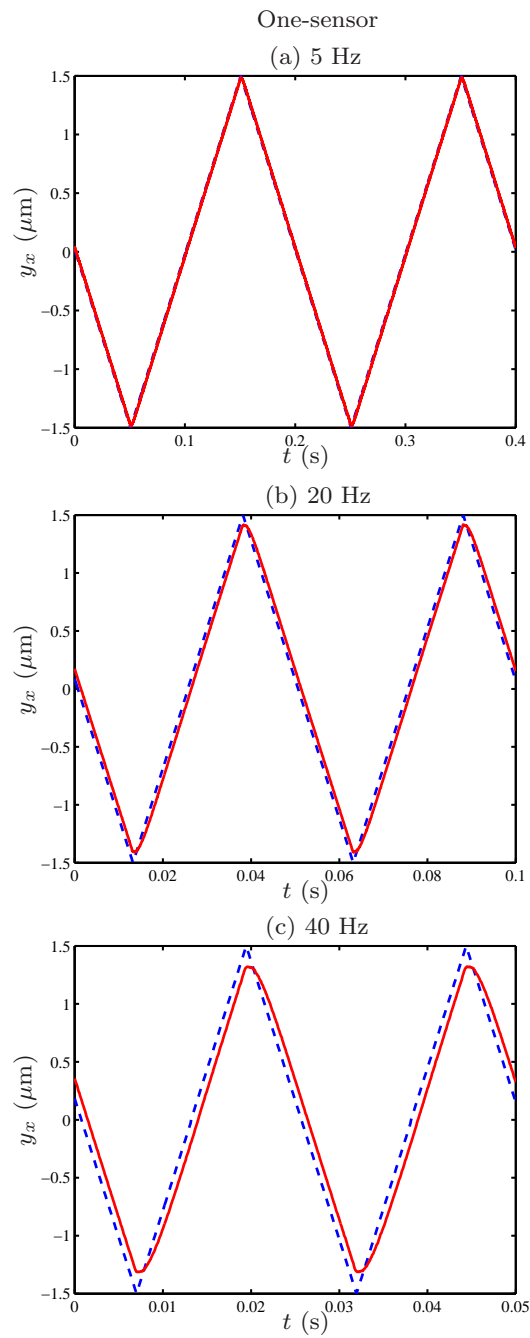


Figure 3.17 : Closed-loop time response plots of 5, 20 and 40 Hz scan using one-sensor-based H_∞ controller. Solid line is measured scanners displacement and dashed line is desired trajectory.

track various triangular waveforms as illustrated in Fig. 3.17. This is due to the existence of the notch filter in $\tilde{K}_c(s)$. Also, the two-sensor-based controller performs better in terms of rejecting low-frequency vibrations and noise.

The closed-loop tracking errors due to $\tilde{K}_c(s)$ are tabulated in the last column of Table 3.2. It can be seen that up to 20 Hz scanning frequency, the tracking performance is comparable to that obtained through $K_c(s)$. However, at higher scan frequencies the tracking performance decrease rapidly as illustrated in Table 3.2 and Fig. 3.17.

3.6 Summary

We described how a high-bandwidth low-noise two-sensor-based controller could be designed for a piezoelectric tube scanner. The two-input one-output controller uses measurements obtained from a capacitive displacement sensor at low frequencies and the piezoelectric voltage signal at high frequencies. By keeping the capacitive sensor loop bandwidth low, the effect of sensor noise on the overall system is significantly reduced. Having access to the piezoelectric voltage signal allows the controller to achieve tracking over a wide bandwidth and successful damping of the resonant mode of the scanner. Overall, this chapter provides a further justification for using complementary sensors, whenever possible, in nanoscale positioning systems in line with results reported in [58] and [29]. In the next chapter, the focus of our works shifts from designing feedback controllers for a prototype piezoelectric tube scanner to an actual scanner used in a commercial AFM.

Chapter 4

Positive Position Feedback control of an Atomic Force Microscope

This chapter presents experimental implementation of Positive Position Feedback (PPF) control scheme for vibration and cross-coupling compensation of a piezoelectric tube scanner in a commercial AFM. In this chapter we illustrate the improvement in accuracy and imaging speed that can be achieved by using a properly designed feedback controller such as the PPF controller. In the first section of this chapter, the motivation and overview of PPF control scheme were presented. Section 4.2 provides descriptions of the AFM and other experimental setup used in this work. Modeling and identification of the system transfer functions are explained in Section 4.3. Control schemes for the AFM scanner are devised in Section 4.4. Finally, in Section 4.5 experimental results are given to illustrate the drastic improvement in accuracy and imaging speed that can be achieved with the proposed control schemes.

4.1 Introduction

Feedback has always been an integral part of every AFM for vertical positioning. A feedback controller requires a measurement signal to operate effectively. In an AFM, this measurement is conveniently made available by the laser-photodetector sensor, enabling accurate vertical positioning of the scanner. The utilization of feedback to improve lateral positioning of the scanner, however, requires displacement sensors to be incorporated into the device. These sensors were not included in scanners of earlier AFMs. However, they are progressively being built into a new generation of commercially available AFMs. The ability to use feedback for lateral positioning brings about a number of exciting possibilities

some of which have already materialized in commercially available AFMs. For example, PI controllers have been used to reduce the effects of hysteresis and creep with considerable success. Apart from the above complicating factors, there are two other issues that hamper the operation of an AFM: 1) the highly resonant nature of the scanner, and 2) the cross coupling between the various axes of the scanner [68]. However, the controllers used in these AFMs are often not designed to deal with these two issues.

The contribution of this chapter is the improvement of the performance of a commercial AFM by using a PPF control scheme to compensate for the vibration and cross-couplings of its piezoelectric tube scanner. The PPF controllers were initially designed to suppress mechanical vibrations of highly resonant aerospace structures [22]. They have been successfully implemented on a range of lightly damped structures [54, 61, 71]. Their effectiveness in improving accuracy and bandwidth of nanopositioning systems was recently investigated in [8]. PPF controllers have a number of important features. In particular, they have a simple structure, are easy to implement and their transfer functions roll off at a rate of 40 dB/decade at higher frequencies. The latter is important in terms of the overall effect of the sensor noise on the scanner's positioning accuracy. The PPF control scheme can be incorporated into most modern AFMs with minimal effort since they can be implemented in software with the existing hardware. At present, the focus of this work is only limited to compensating the vibration and cross-couplings in the lateral axes of the scanner. In this chapter, the performance of this control scheme is assessed by comparing surface topography images of a calibration grating obtained using this control scheme with the one obtained using a well-tuned PI controller in the feedback loop. Experimental results show that by implementing the PPF control scheme, relatively good images in comparison with a well-tuned PI controller can still be obtained up to line-scan of 60 Hz.

4.2 Experimental Setup

The experimental setup consisted of a commercial NT-MDT Ntegra Scanning Probe Microscope (SPM) as shown in Fig. 4.1. This SPM can be used to perform almost all scanning probe microscopy techniques in air and liquid environment. The SPM's operating software limits the highest image resolution to 256×256 pixels. At this resolution the fastest scanning frequency is limited to 31.25 Hz. However, faster scan frequencies are possible by reducing the resolution. For example, by halving the resolution to 128×128 pixels, the fastest scan frequency is doubled to 62.50 Hz.

In the experiments reported in this chapter, the SPM was configured to operate as an AFM and all sample images were scanned in air. The AFM was retrofitted with a home made DC-accurate charge amplifier [26] on the fast axis. The charge amplifier has a constant gain of 68 nC/volt. The use of the charge amplifiers to drive the piezoelectric tube has been shown to result in a reduction of the hysteresis by greater than 90 % as compared with when voltage amplifiers are used [27]. The slow axis was driven by an ACX High Voltage Amplifier with a constant gain of 15. It is sufficient to use the voltage amplifier because the effect of hysteresis on the slow axis is relatively small. The use of high feedback gain at low frequencies can minimize the effect of hysteresis effectively. A dSPACE-1103 rapid prototyping system was used to implement the feedback controllers in real time. The amplifiers and the SPM were interfaced with the dSPACE system using a signal access module (SAM) that allowed direct access to the scanner electrodes. This setup enabled us to directly control the lateral movements of the scanner. However, the scanner vertical positioning was achieved using the standard NT-MDT SPM controller. In other words we replaced the rastering mechanism of the AFM with our own system.

There are two types of scanner that can be incorporated into this SPM, an open-loop scanner (without displacement sensors) and a closed-loop scanner (with displacement sensors). The closed-loop scanner allows accurate position tracking through feedback control.

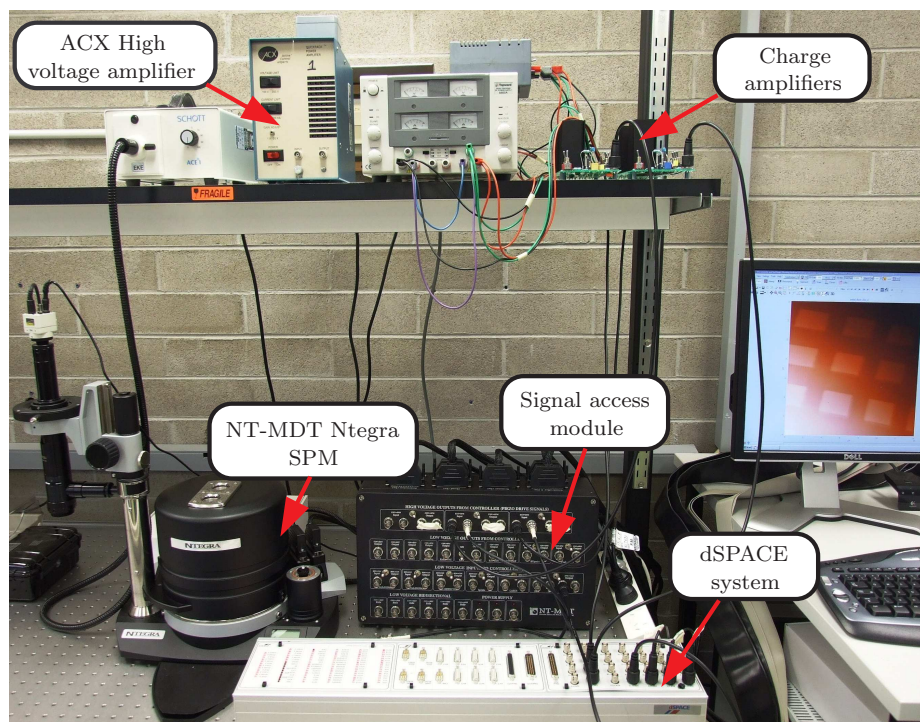


Figure 4.1 : SPM system and experimental setup used in this work.

In these experiments, a closed-loop scanner NT-MDT Z50309cl was used to perform 3D positioning in the SPM. It has a scanning range of $100 \times 100 \times 10 \mu\text{m}$. The capacitive sensors that are incorporated into the scanner apparatus allow for direct measurements of the scanner displacement in x , y and z axes. The bandwidth of these capacitive sensors is tunable and has a maximum value of 10 kHz. In these experiments the bandwidth is set to the maximum in order to minimize the effect of the capacitive sensors dynamics on the displacement measurements. The sensitivity of the capacitive sensors was determined by making the scanner track a 0.5 Hz triangular wave of $100 \mu\text{m}$ amplitude in closed-loop using the standard NT-MDT SPM controller. Simultaneously, the corresponding output voltages from the capacitive sensors were also measured. From these two values, the sensitivity of the capacitive sensors incorporated into the x and y axes was calculated to be $6.33 \mu\text{m/volt}$. In this test, a low frequency triangular wave was used to ensure perfect tracking by the standard NT-MDT SPM controller.

The piezoelectric tube in the scanner has quartered internal and external electrodes. Such an electrode arrangement allows the scanner to be driven in a bridge configuration [27] where the electrodes are wired in pairs as illustrated in Fig. 4.2. These electrode pairs are referred to as $+x$, $-x$, $+y$ and $-y$ electrode pairs. An advantage of using the bridge configuration is that it halves the input voltage requirement as compared to the more widely used grounded internal electrode configuration. Nevertheless, in these experiments the $-x$ and $-y$ electrodes are grounded in order to simplify the experimental setup. Furthermore, the need for a large scanning range does not arise here since the scanner is only made to operate within 10 % of its full lateral scanning range.

A dSPACE rapid prototyping system equipped with ControlDesk software was interfaced to the AFM through an expansion box that allowed direct access to the capacitive sensor measurements and control signals that were to be applied to the piezoelectric actuator. During scans, measurements from the capacitive sensors and the photodiode were

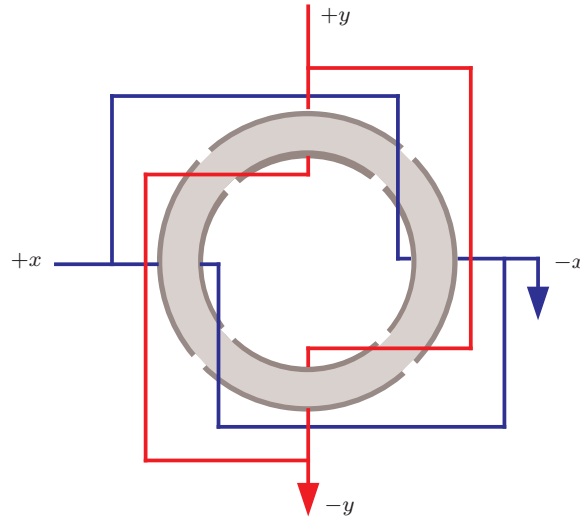


Figure 4.2 : Top view of the piezoelectric tube with the internal and external electrode wired in a bridge configuration.

recorded and processed in Matlab to generate AFM images.

4.3 System Identification

In this section, the procedure used to model the AFM scanner is described. The scanner is treated as a two single-input single-output (SISO) systems in parallel. The inputs being the voltage signals applied to the charge amplifier driving the $+x$ electrode pair, u_x , and to the voltage amplifier driving the $+y$ electrode pair, u_y . The outputs of the system are the scanner displacement measurements from the capacitive sensors in x axis, c_x , and in y axis, c_y . Here, accurate models of the systems were obtained through system identification. System identification is an experimental approach to modeling where mathematical models are obtained from a set of input and output data [59].

Fig. 4.3 illustrates the experimental setup used for the system identification experiment. A dual-channel HP35670A spectrum analyzer was used to obtain the following frequency

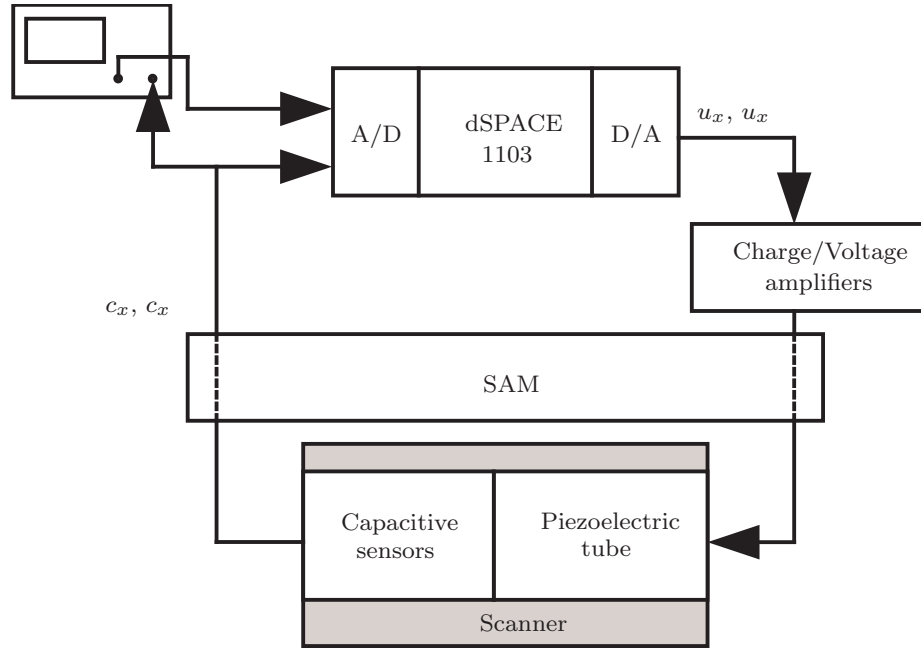


Figure 4.3 : Block diagram of the experimental setup used for system identification of the scanner.

response functions (FRFs) nonparametrically

$$G_{c_x u_x}(i\omega) = \frac{c_x(i\omega)}{u_x(i\omega)} \quad (4.1)$$

and

$$G_{c_y u_y}(i\omega) = \frac{c_y(i\omega)}{u_y(i\omega)}. \quad (4.2)$$

A band-limited random noise signal of amplitude 0.5 Vpk within the frequency range of 1 Hz to 1600 Hz was generated using the spectrum analyzer and applied to the charge amplifiers as the input. The corresponding outputs from the capacitive displacement sensors were also recorded using the spectrum analyzer. These input-output data were processed to generate the FRF (4.1) and (4.2) in a non-parametric form as illustrated in Fig. 4.4. Note that the 0 dB (unity gain) at DC in both FRFs was achieved by introducing appropriate

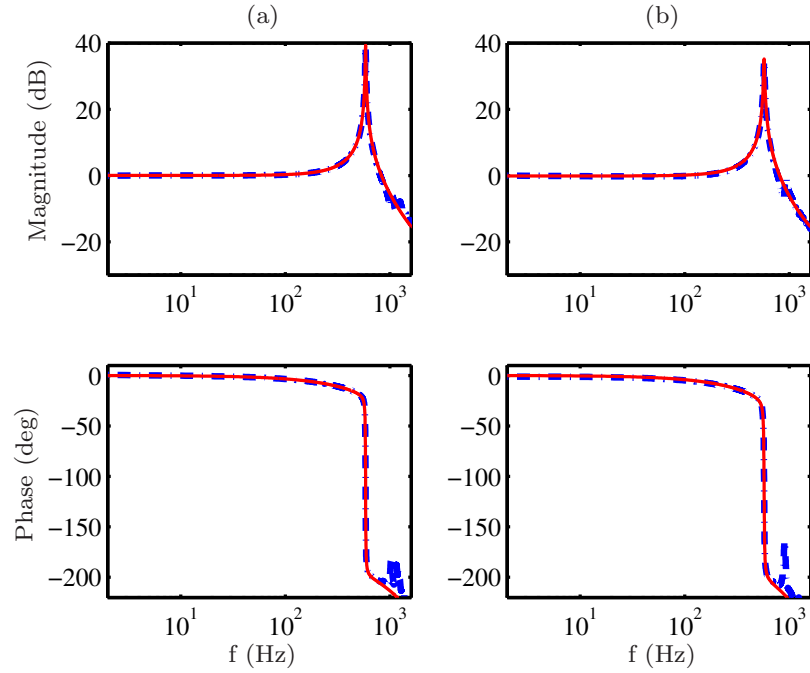


Figure 4.4 : Experimental (dash-dot) and identified model (solid) frequency response of (a) $G_{c_x u_x}(i\omega)$ and (b) $G_{c_y u_y}(i\omega)$.

input gains in the dSPACE system.

Two second-order models were fitted to the FRFs data using the frequency domain subspace-based system identification approach as described in [47] and [48]. The following transfer functions were found to be a good fit as illustrated in Fig. 4.4,

$$G_{c_x u_x}(s) = \frac{0.05311s^2 - 1230s + 1.362 \times 10^7}{s^2 + 40.38s + 1.354 \times 10^7} \quad (4.3)$$

and

$$G_{c_y u_y}(s) = \frac{0.0849s^2 - 1416s + 1.288 \times 10^7}{s^2 + 61.74s + 1.303 \times 10^7}. \quad (4.4)$$

It can be inferred from transfer functions (4.3) and (4.4) that the piezoelectric tube scanner has very weakly damped resonances in x and y axes. In the x axis the resonance is

at 585 Hz with a damping ratio of 0.006 and in the y axis the resonance is at 574 Hz with a damping ratio of 0.009. It must be mentioned here that the non-minimum phase zeros in both transfer functions do not reflect the physical nature of the scanner, but are rather artifacts of the system identification. The subspace-based system identification approach introduces these non-minimum phase zeros in order to model delays which exist in the system due to the capacitive sensor signal processing electronics and dSPACE sampling time.

4.4 Controller Design

To address the issues discussed in Section 4.1, we designed feedback controllers to augment the damping of the scanner's transfer functions to achieve improved lateral positioning. Feedback controllers for the x and y axes were designed independently since the scanner is treated as a two SISO systems in parallel. Structure of the x axis feedback controller is illustrated in Fig. 4.5. The overall control structure consists of two feedback loops. The inner loop contains a PPF controller that works to increase the overall damping of the scanner. The outer loop contains a high-gain integral controller to provide tracking.

4.4.1 PPF Controller

In the current context, the PPF controller can be parameterized as

$$K_{PPF_x}(s) = \frac{a_0}{s^2 + b_1s + b_0} \quad (4.5)$$

where a_0 , b_1 and b_0 are the control parameters. Standard results in control theory, [33], imply that the closed-loop system of the inner loop is given by

$$G_{c_x u_x}^{(cl)} = \frac{G_{c_x u_x}(s)}{1 - G_{c_x u_x}(s) K_{PPF_x}(s)}. \quad (4.6)$$

Equation (4.3) can be rewrite as

$$G_{c_x u_x}(s) = \frac{n_2 s^2 + n_1 s + n_0}{s^2 + d_1 s + d_0}, \quad (4.7)$$

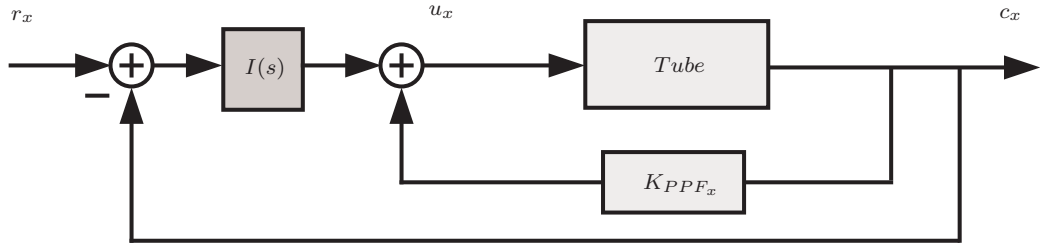


Figure 4.5 : Structure of the x axis feedback controller. The inner feedback loop is a PPF controller designed to damp the highly resonant mode of the tube. Integral action is also incorporated to achieve satisfactory tracking.

where $n_2 = 0.05311$, $n_1 = 1230$, $n_0 = 1.362 \times 10^7$, $d_1 = 61.74$ and $d_0 = 1.354 \times 10^7$. From (4.6), it can be checked that the poles of the closed-loop transfer function $G_{c_x u_x}^{(cl)}$ are roots of the polynomial

$$P(s) = s^4 + (b_1 + d_1)s^3 + (-a_0 n_2 + b_1 d_1 + d_0 + b_0)s^2 + (-a_0 n_1 + b_1 d_0 + b_0 d_1)s - a_0 n_0 + b_0 d_0. \quad (4.8)$$

Damping can be achieved by shifting these closed-loop poles deeper into the left-half plane (LHP). Let $\{p_i\}_{i=1}^4$ be the desired closed-loop pole positions and

$$Q(s) = s^4 + q_3 s^3 + q_2 s^2 + q_1 s + q_0 \quad (4.9)$$

be the corresponding polynomial with $\{p_i\}_{i=1}^4$ as its roots. Matching the coefficients of (4.8) and (4.9) gives us four linear equations that can be used to solve the three control parameters. However, since there are more equations than unknowns, this set of linear equations is considered as an overdetermined system which cannot be solved for a set of exact solution. One method for solving such system is by using the least squares approach where the obtained solutions are “closest” to satisfying all of the linear equations [74].

In this work, the numerator of the PPF controller is augmented with $a_1 s$ to result in four control parameters, i.e., a_1 , a_0 , b_1 and b_0 . This will allow the solution for the linear

equations to be a set of exact solution. The augmented PPF controller is given as

$$\tilde{K}_{PPF_x}(s) = \frac{a_1s + a_0}{s^2 + b_1s + b_0}. \quad (4.10)$$

Consequently, the polynomial given in (4.8) can be rewritten as

$$\begin{aligned} \tilde{P}(s) = & s^4 + (-a_1n_2 + b_1 + d_1)s^3 + (-a_1n_1 - a_0n_2 + b_1d_1 + d_0 + b_0)s^2 \\ & + (-a_1n_0 - a_0n_1 + b_1d_0 + b_0d_1)s - a_0n_0 + b_0d_0. \end{aligned} \quad (4.11)$$

Matching the coefficients of (4.11) and (4.9) gives four linear equations in terms of the control parameters

$$-a_1n_2 + b_1 + d_1 = q_3 \quad (4.12)$$

$$-a_1n_1 - a_0n_2 + b_1d_1 + d_0 + b_0 = q_2 \quad (4.13)$$

$$-a_1n_0 - a_0n_1 + b_1d_0 + b_0d_1 = q_1 \quad (4.14)$$

and

$$-a_0n_0 + b_0d_0 = q_0. \quad (4.15)$$

Rewriting (4.12) - (4.15) in matrix form give

$$AX + C = B \quad (4.16)$$

where

$$A = \begin{bmatrix} -n_2 & 0 & 1 & 0 \\ -n_1 & -n_2 & d_1 & 1 \\ -n_0 & -n_1 & d_0 & d_1 \\ 0 & -n_0 & 0 & d_0 \end{bmatrix} \quad (4.17)$$

$$X = \begin{bmatrix} a_1 & a_0 & b_1 & b_0 \end{bmatrix}^T \quad (4.18)$$

$$C = \begin{bmatrix} d_1 & d_0 & 0 & 0 \end{bmatrix}^T \quad (4.19)$$

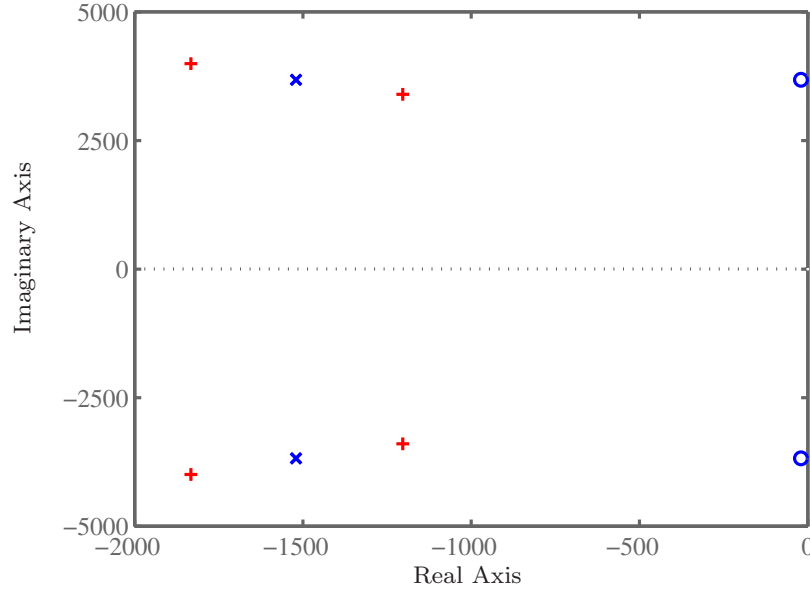


Figure 4.6 : Map of open-loop (o), desired closed-loop (\times) and achieved closed-loop (+) poles for the x axis.

and

$$B = \begin{bmatrix} q_3 & q_2 & q_1 & q_0 \end{bmatrix}^T. \quad (4.20)$$

The control parameters for controller $\tilde{K}_{PPF_x}(s)$ can be obtained by solving

$$X = A^{-1} [B - C]. \quad (4.21)$$

In order for the controller $\tilde{K}_{PPF_x}(s)$ to be stable, b_1 and b_0 have to be positive. Here, the desired closed-loop poles are chosen such that the solutions of (4.21) would result in positive value for b_1 and b_0 .

The locations of the open-loop poles and the desired closed-loop poles are illustrated in Fig. 4.6. Note that, the desired closed-loop poles locations are shifted further into the LHP by 1500 units from the open-loop poles. The coefficients of the polynomial (4.9), calculated from these closed-loop poles, are $q_3 = 6.0808 \times 10^3$, $q_2 = 4.0944 \times 10^7$, $q_1 = 9.6380 \times 10^{10}$ and $q_0 = 2.5122 \times 10^{14}$. By substituting these coefficients and the coefficients defined in

(4.7) into (4.16), the control parameters are solved to obtain the controller

$$\tilde{K}_{PPF_x} = \frac{-163.2s + 9.242 \times 10^6}{s^2 + 6032s + 2.785 \times 10^7}. \quad (4.22)$$

Observe that obtained controller contains a real zero at about 9000 Hz. At such high frequency, this zero has negligible effect on the behavior of the controller at low-frequency regions. In particular, this controller is only designed to damp the scanner's first resonant mode which is at about 580 Hz. Here, this high-frequency zero is conveniently ignored to obtain the PPF controller in the original form as

$$K_{PPF_x}(s) = \frac{9.242 \times 10^6}{s^2 + 6032s + 2.785 \times 10^7}. \quad (4.23)$$

The achieved closed-loop poles with this PPF controller implemented in the feedback loop is checked to see the effects of omitting the high-frequency zero. Fig. 4.6 illustrates the achieved closed-loop poles are stable and shifted further into the LHP around the desired closed-loop poles.

A similar controller was designed for the y axis and therefore, is omitted for the sake of conciseness. The obtained PPF controllers for y axis can be described as

$$K_{PPF_y}(s) = \frac{9.499 \times 10^6}{s^2 + 6062s + 2.753 \times 10^7}. \quad (4.24)$$

4.4.2 High-gain Integral Controller

The designed control system also includes a high-gain integral controller

$$I(s) = \frac{K_I}{s} \quad (4.25)$$

as illustrated in Fig. 4.5. Inclusion of an integrator amounts to applying a high gain at low frequencies that reduces the effects of piezoelectric creep and hysteresis to a minimum. Another important benefit of the proposed combined feedback structure is the significant

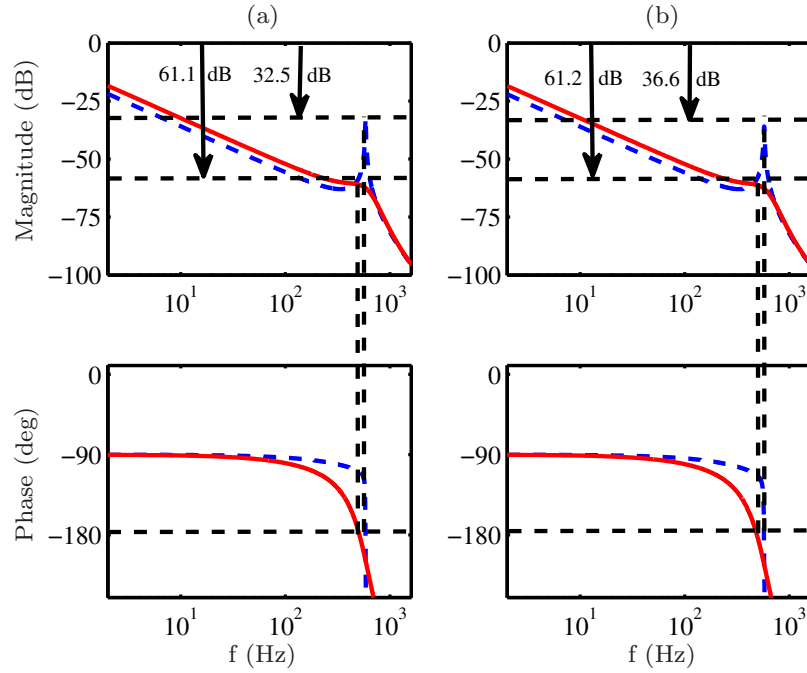


Figure 4.7 : Bode diagrams showing gain margins when a unity gain integral controller is cascaded with undamped (---) and damped (—) scanner's transfer functions in (a) x and (b) y axes.

reduction that can be achieved in cross-coupling between various axes of the scanner.

The use of high gain in the integral controllers is made possible by the suppression of the sharp resonant peaks in the x and y axes due to the PPF controllers. Fig. 4.7 illustrates Bode diagrams showing gain margins when a unity gain integral controller is cascaded with undamped scanner's transfer functions, 1) $G_{c_x u_x}(s)$ and 2) $G_{c_y u_y}(s)$, and with damped scanner's transfer functions 3) $G_{c_x u_x}^{(cl)}$ and 4) $G_{c_y u_y}^{(cl)}$.

The gain margins for the undamped systems are 32.5 dB and 36.6 dB in x and y axes respectively. This implies that the gain of the integrator K_I is limited to less than 42 and 68 in the x and y axes respectively for stability of the closed-loop systems. However, the gain margins for the damped systems are 60.8 dB and 61.0 dB in x and y axes respectively.

This implies that the gain of the integrator K_I can be increased significantly from 1 to up to 1135 and 1148 in the x and y axes respectively, before the closed-loop systems become unstable. In this work, the gain of the integrators were tuned to provide high closed-loop system bandwidth but with reasonable gain and phase margin.

4.5 Experimental Results

4.5.1 Frequency and Time Responses

The performance of the PPF control scheme was first evaluated by measuring the closed-loop frequency responses of the system using the spectrum analyzer. In Fig. 4.8, the measured closed-loop frequency responses are plotted along with the open-loop frequency responses that were obtained in Section 4.3. By inspecting Figs. 4.8 (a) and (d) we observe that the closed-loop system bandwidth of both axes is about 300 Hz. Also, a damping of more than 30 dB at each resonant mode is apparent from the frequency responses. However, in the closed-loop system, the frequency responses exhibit a faster phase drop rate as compared to the open-loop system. Consequently this results in greater phase shifts between the desired and the achieved trajectories. Note that with the current experimental setup, we were not able to measure the closed-loop frequency responses of the AFM scanner with the well-tuned PI controller that is built into the AFM. When this controller is in use, access to the scanner electrodes through the signal access module and the raw signals obtained from the capacitive sensors are not made available to the user.

To appreciate the improvement achieved in lateral positioning of the scanner, we performed a simple experiment. In open-loop, a 2 Hz triangular signal was applied to the x axis of the piezoelectric tube to achieve an 8 μm scan. The displacements in the x and y axes of the tube were measured using the built-in capacitive displacement sensors. A similar experiment was then carried out with the PPF control scheme implemented on the tube. The results are plotted in Fig. 4.9 (a). A similar set of experiments were performed

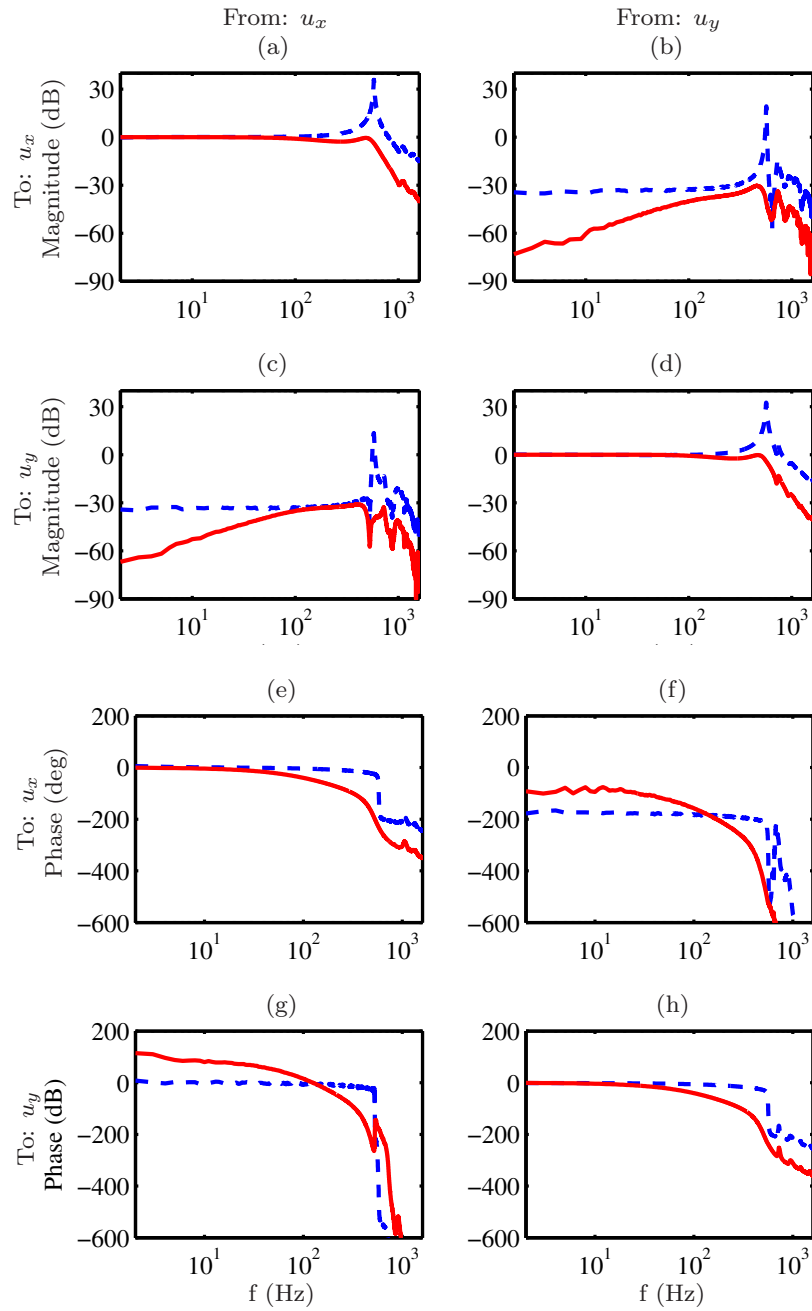


Figure 4.8 : Open-loop (dash) and closed-loop (solid) frequency responses of the scanner. The resonant behavior of the scanner is improved by over 30 dB due to control action. The proposed feedback control strategy results in significant improvement in cross-coupling between the fast and slow axes of the scanner.

at 30 Hz to simulate a fast scan. The results are plotted in Fig. 4.9 (c). A considerable improvement can be observed by comparing the open-loop and closed-loop motions of the tube. During a fast scan we can observe significant distortions due to the excitation of the tube's resonance. By applying the feedback controller, we managed to significantly reduce the distortions and achieved a considerable improvement in tracking performance. In particular, for the 30 Hz scan, the fast axis RMS tracking error was reduced from 280 nm to 46 nm, and the cross-coupling to the slow axis was reduced from 50 nm to 16 nm due to control action. This improvement directly translates into an image with less distortion. A significant component of the closed-loop error is due to the phase shift between the desired and the achieved trajectories. This phase shift has a minimal effect on the image quality and can be handled using a feedforward controller.

The frequency responses for the cross-coupling terms of the AFM scanner were also obtained and illustrated in Fig. 4.8 (b) and (c). In open-loop, significant cross-coupling can be observed between lateral axes of the scanner. For frequency ranges below the tube's resonance frequency, there is approximately 32 dB cross-coupling between the x and y axes of the scanner. This means that an $8\text{ }\mu\text{m}$ amplitude triangular motion of the x axis will translate into approximately $0.2\text{ }\mu\text{m}$ amplitude triangular motion of the y axis and *vice versa*, generating substantial distortion in the resulting image. Also higher cross-coupling exists at, and close to the resonance frequency of the tube. The effect from the cross-coupling can be observed in Fig. 4.9 (b) and (d) where a triangular motion of approximately $0.18\text{ }\mu\text{m}$ amplitude can be seen in the y axis when the x axis is made to produce an $8\text{ }\mu\text{m}$ amplitude triangular motion. Note that at 30 Hz scan, in addition to the cross-coupling, the distortions due to the excitation of the tube's resonance can also be observed in the y axis.

In closed-loop, Fig. 4.8 (b) and (c) illustrate substantial decrease in the cross-coupling between the lateral axes of the scanner. In particular, the cross-coupling is less than 52 dB for low frequency ranges (i.e. $\leq 10\text{ Hz}$). This means that for a low frequency scan, an $8\text{ }\mu\text{m}$

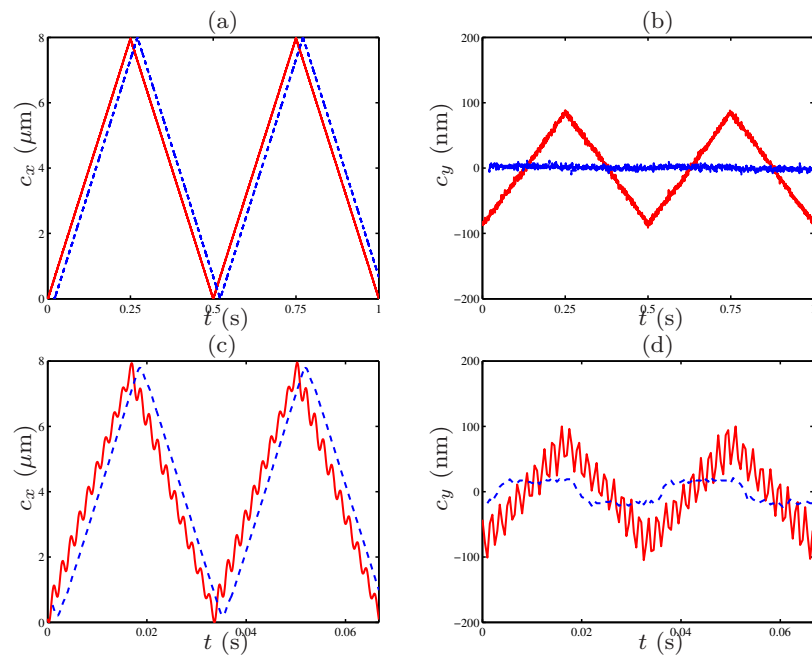


Figure 4.9 : Closed-loop (dash) and open-loop (solid) tracking performance (left) and cross-coupling properties (right) of the scanner for 2 Hz scan (top), and 30 Hz scan (bottom). (A small phase shift was purposely added into the close-loop time responses in order to clearly display the open- and closed-loop time responses.)

amplitude triangular motion of the x axis will only translate into approximately $0.02 \mu\text{m}$ amplitude triangular motion of the y axis. Although there are no direct feedback controls on the cross-coupling terms, the inclusion of high-gain integrator in both axes has indirectly resulted in a significant reduction in the cross-coupling. Nevertheless, the effect of the integral action diminishes as the frequency increases.

4.5.2 AFM Imaging

Having improved the lateral positioning of the scanner, we then moved on to investigate the overall improvement in imaging capability of our modified AFM. During the imaging, the atomic force microscope was operated in constant force mode using a micro-cantilever with spring constant of 0.2 N/m . The sample was a 20 nm feature-height NT-MDT TGQ1 calibration grating with a $3 \mu\text{m}$ pitch. The well-tuned PI was first used to develop $8 \mu\text{m} \times 8 \mu\text{m}$ images of the sample at 2 Hz , 10 Hz and 30 Hz scan frequencies with a resolution of 256×256 pixels. Faster scans beyond 30 Hz with the AFM standard software, at this resolution, were not possible. In each case, a significant amount of time was devoted to tune the AFM so that the best possible image could be generated. We then imaged the sample at identical frequencies, but this time with the PPF control scheme implemented on the scanner. These images are plotted in Fig. 4.10 for comparison, and illustrate a drastic improvement in image quality and sharpness. Furthermore, our modifications enabled us to scan beyond the 30 Hz speed set by the AFM standard software. In particular, we developed scans of the sample at 40 Hz , 50 Hz and 60 Hz with the same resolution. These results are also plotted in Fig. 4.10.

In order to further analyze the AFM images illustrated in Fig. 4.10, we plot the cross-section curves of these images at about $y = 4 \mu\text{m}$ in Fig. 4.11. The cross-section curves were taken in parallel to the square profile of the calibration grating. The scan direction for Fig. 4.11 (a), (b) and (c) is from 0 to $8 \mu\text{m}$ and the scan direction for Fig. 4.11 (d) to (i) is from 8 to $0 \mu\text{m}$. It can be observed that by using the PPF control scheme, the height-

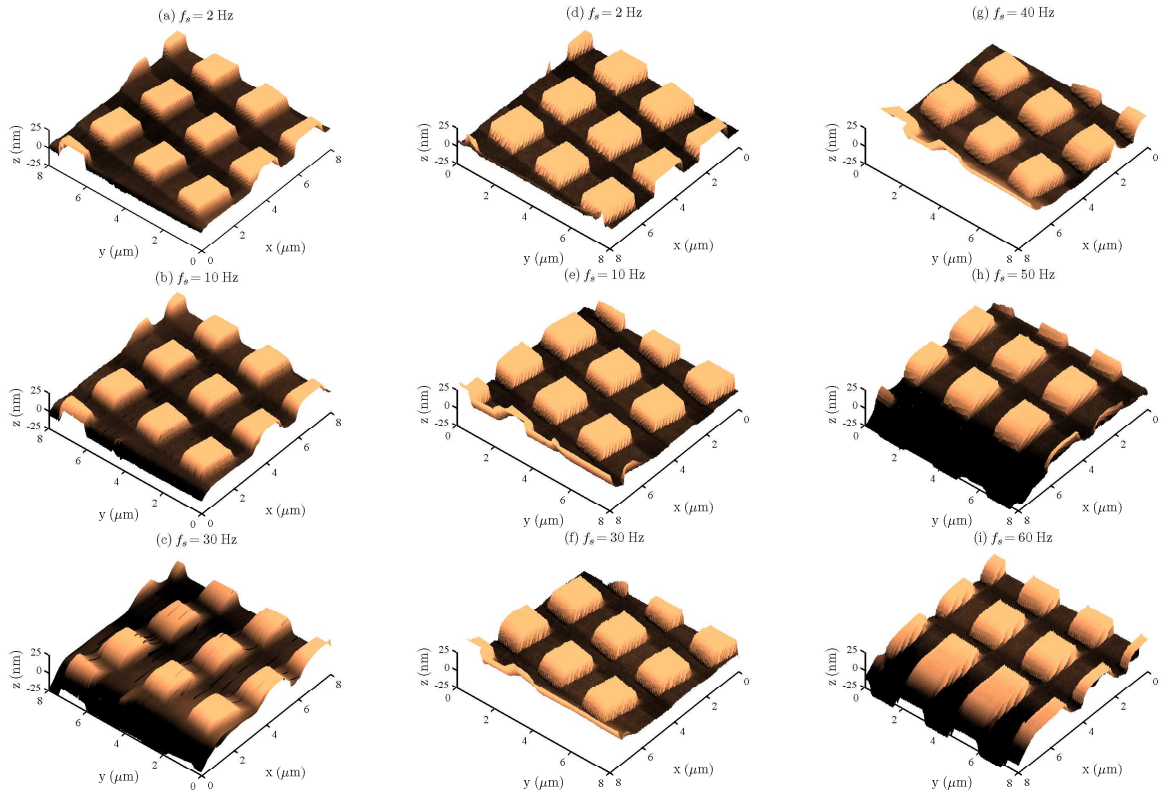


Figure 4.10 : First two columns: AFM images of NT-MDT TGQ1 grating scanned in contact mode constant force at 2, 10 and 30 Hz. Images displayed in (a), (b) and (c) were developed using the well-tuned PI controller. Images displayed in (d), (e) and (f) were generated using the PPF controller. A significant improvement in image quality can be observed. Third column: We were able to generate images at scan frequencies beyond the AFM limit of 30 Hz. 40, 50 and 60 Hz scans are illustrated in (g), (h) and (i) respectively.

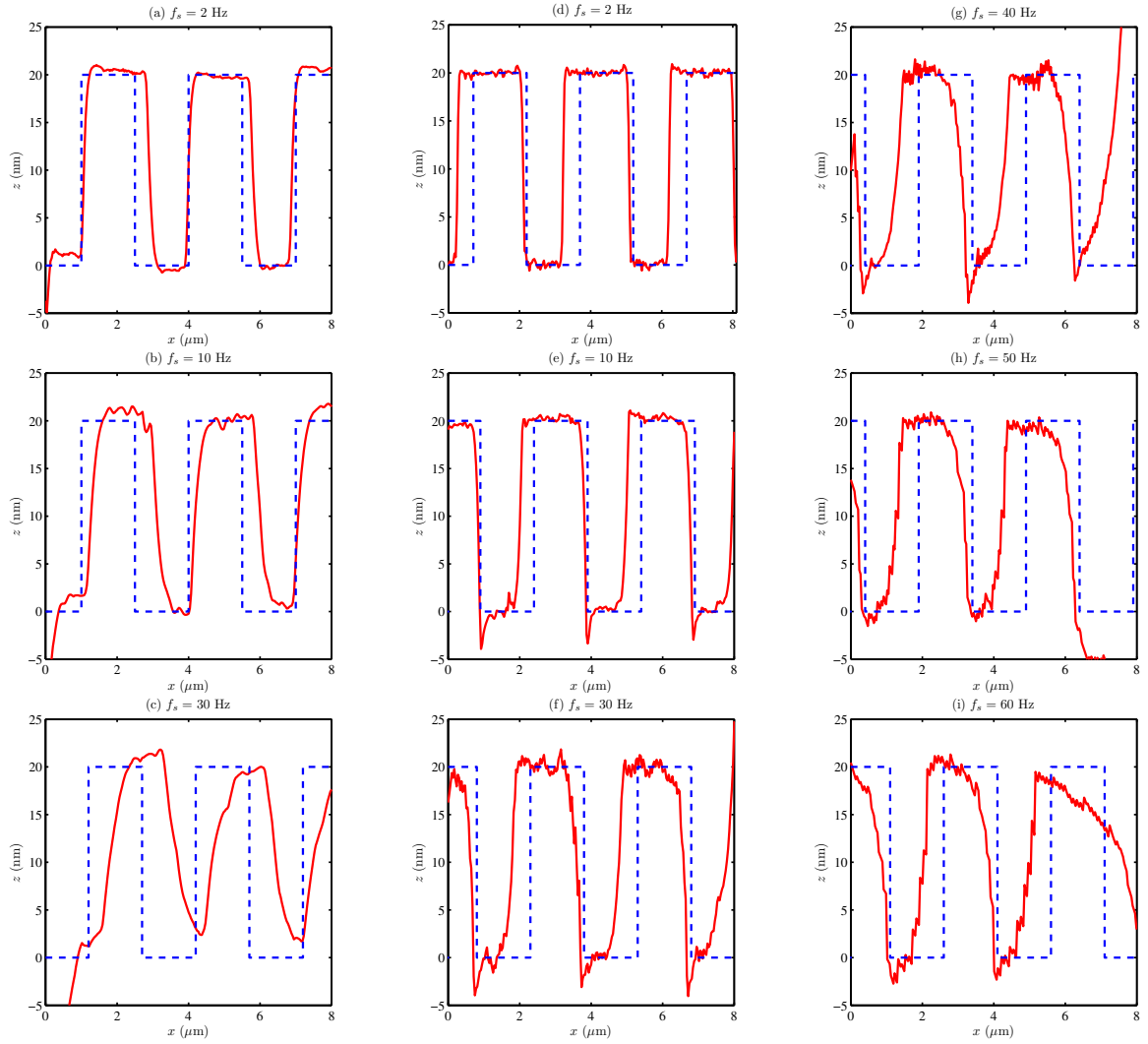


Figure 4.11 : Cross-section (solid) and reference (dash) curves of the AFM images illustrated in Fig. 4.10 (a) to (i). The cross-section curves were taken about the center of the AFM images and parallel to the square profile of the calibration grating. The scan direction of the curves displayed in (a), (b) and (c) are from 0 to 8 μm . The scan direction of the curves displayed in (d) to (i) are from 8 to 0 μm .

profile of the calibration grating was better captured. This controller enables us to set the feedback gain of the z axis significantly higher than the well-tune PI controller, resulting in a better scan. However, the accuracy of the curves representing the true height-profile of the calibration grating decreases with increasing scan frequency. At high scan frequencies, the z axis feedback loop is simply not fast enough to detect changes in the height of the calibration grating. Nevertheless, it can be observed that the PPF control scheme results in better images, even at high scan frequencies.

4.6 Discussion of Results

To this end, we wish to draw comparisons between the implemented PPF control scheme and other existing methods that were mentioned in the previous chapter. The use of H_∞ control for designing feedback controllers to improve the accuracy and speed of AFM scanners has been shown to be quite successful in Refs. [65, 75]. While these H_∞ controllers provide adequate closed-loop robustness, they are often compensators of rather high orders. Thus, these controllers are more complex and their implementation may need a more sophisticated setup, when compared with the proposed PPF controller which has a very simple structure. In our work, the implementation of the PPF control scheme has resulted in a high closed-loop bandwidth, of about 300 Hz, and a damping of more than 30 dB at the scanner's first resonant mode. These improvements were achieved with a third order controller that is very straightforward to implement using either analog or digital methods.

In [39, 42], a feedforward input was used to compensate for vibration in feedback controlled AFM piezoactuator systems. This method can be quite effective in compensating induced structural vibration as proved experimentally in both [39] and [42]. However, it may not be as effective against external vibrations and noise since the piezoactuators are still highly resonant structures. In our work, the overall mechanical damping of the piezoelectric tube was increased by using the PPF controllers. This makes the piezoelectric tube impervious against the induced and the external vibrations. Furthermore, if needed a

feedforward controller can be added to our controller to enable faster scans.

4.7 Summary

In summary, we demonstrated that by augmenting the damping of an AFM scanner using a PPF controller, and minimizing the cross-coupling between its fast and slow axes by incorporating an additional Integral controller, and also by using charge drive on its fast axis, the quality of the developed image could be drastically improved. This is a direct result of the improvement in lateral positioning of the AFM scanner. We were also able to scan at frequencies beyond the limit set by the AFM software. In the following chapter, we introduce a new scanning method that allows fast AFM. In this scanning method, the scanner is scanned in a spiral pattern instead of the well established raster pattern.

Chapter 5

Fast Spiral-Scan Atomic Force Microscopy

Today, the majority of commercially available AFMs use raster scans to image a sample's surface. The improvement of the frequency and precision of raster scans through the use of feedback control approach has been shown to be quite successful in the previous chapters and in the References [7, 17, 43, 44, 72, 75, 78]. In this approach, feedback controllers are used to flatten the frequency response of the scanner, thus allowing for faster scans. However, as the scan frequency is increased closer to the mechanical bandwidth of the scanner in order to realize fast AFM, the positioning precision of the scanner deteriorates considerably. The closed-loop tracking of the triangular waveform typically results in the corners of these waveform to be rounded off and distorted. This is mainly due to the presence of high frequency harmonics of the triangular waveform that are inevitably outside of the bandwidth of the closed-loop system. Consequently, AFM images generated at high speeds often demonstrate significant distortions especially around the edges of the images.

This chapter proposes a new scan technique for fast AFM by forcing the piezoelectric tube scanner to follow a spiral pattern instead of the well established raster pattern, over the surface that is to be imaged. A constant angular velocity (CAV) spiral scan can be produced by applying slowly varying-amplitude single frequency sinusoidal signals to the x and y axes of the piezoelectric tube scanner. The use of the single frequency input signals allows for scanning to be performed at very high speeds without exciting the resonance of the scanner and with relatively small control efforts. An alternative method is to generate the spiral pattern in a constant linear velocity (CLV) approach. The latter method has been implemented in some disk storage devices, such as Compact Disk-Read Only

Memory (CD-ROM) where the information is stored in a continuous spiral track over the disk's surface [36]. The proposed method is an alternative to raster-based sinusoidal scan methods that are used to achieve fast scans in e.g., scanning near-field optical microscopy (SNOM) [34]. In spiral scanning, both axes follow sinusoidal signals of identical frequencies resulting in a smooth trajectory. This avoids the transient behavior that may occur in sinusoidal scans as the probe moves from one line to the next. Furthermore the proposed method does not require specialized hardware, e.g. a tuning fork actuator, and can be implemented on a standard AFM with minor software modifications.

The remainder of this chapter is organized as follows. The generation of input signals to produce the spiral pattern is described in detail in Section 5.1. Control schemes for the AFM scanner are devised in Section 5.2. Finally, in Section 5.3 experimental results are presented to illustrate the drastic improvement in imaging speed that can be achieved with the proposed new scan trajectory.

5.1 Spiral Scan

This section deals with the generation of input signals that are needed to move the AFM scanner in a spiral pattern, illustrated in Fig. 5.1. The pattern is known as the Archimedean spiral. A property of this spiral is that its pitch P , which is the distance between two consecutive intersections of the spiral curve with any line passing through the origin, is constant [64]. Depending on how this trajectory is traced, the shape is referred to as either a Constant Angular Velocity (CAV) spiral, or a Constant Linear Velocity (CLV) spiral. In the former case, the pattern is traced at a constant angular velocity, while in the latter at a constant linear velocity.

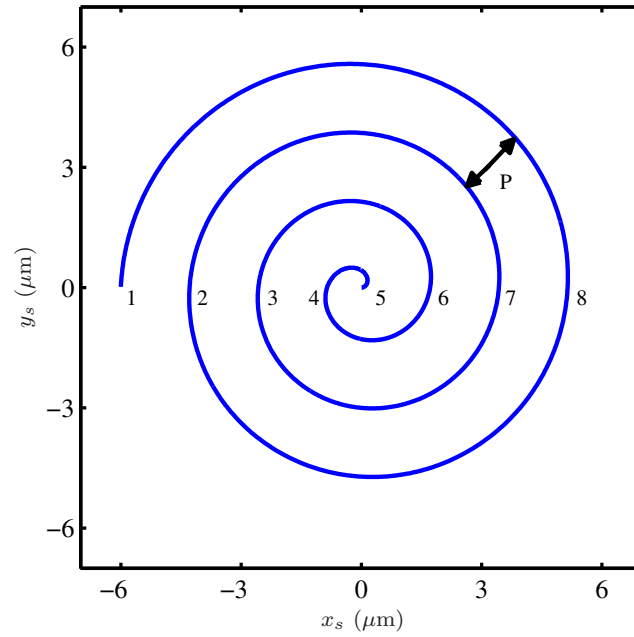


Figure 5.1 : Spiral trajectory of $6.5 \mu\text{m}$ radius with *number of curve* = 8.

5.1.1 The CAV spiral

The equation that generates a CAV spiral of pitch P at an angular velocity of ω can be derived from a differential equation given in [36] as

$$\frac{dr}{dt} = \frac{P\omega}{2\pi} \quad (5.1)$$

where r is the instantaneous radius at time t . Equation (5.1) is solved for r by integrating both sides to obtain

$$\int dr = \frac{P\omega}{2\pi} \int dt. \quad (5.2)$$

For $r = 0$ at $t = 0$,

$$r = \frac{P}{2\pi} \omega t. \quad (5.3)$$

Here, P is calculated as

$$P = \frac{\text{spiral radius} \times 2}{\text{number of curves} - 1} \quad (5.4)$$

where *number of curves* is defined as the number of times the spiral curve crosses through the line $y = 0$. This is exemplified in Fig. 5.1 where the crossing points are numbered. The figure illustrates a spiral scan of $6\ \mu\text{m}$ radius with *number of curves* = 8.

The equation that describes the total scanning time t_{total} associated with a CAV spiral scan can be derived by integrating both sides of equation (5.1) as

$$\int_{r_{start}}^{r_{end}} dr = \frac{P\omega}{2\pi} \int_{t_{start}}^{t_{end}} dt \quad (5.5)$$

where r_{start} and r_{end} are initial and final values of the spiral radius, and t_{start} and t_{end} are initial and final values of the scanning time. From equation (5.5), if $r_{start} = 0$ at $t_{start} = 0$ and $t_{total} = t_{end} - t_{start}$, we obtain

$$t_{total} = \frac{2\pi r_{end}}{P\omega}. \quad (5.6)$$

In order to implement the spiral scans using a piezoelectric tube scanner, equation (5.3) needs to be translated into cartesian coordinates. The transformed equations are

$$x_s = r \cos \theta \quad (5.7)$$

and

$$y_s = r \sin \theta \quad (5.8)$$

where x_s and y_s are input signals to be applied to the scanner in the x and y axes respectively and θ is the angle. From $\omega = \frac{d\theta}{dt}$, θ is obtained as $\theta = \omega t$. An example of input signals x_s and y_s that can generate the spiral in Fig. 5.1 is plotted in Fig. 5.2. The figure illustrates constant phase errors between the input signals and measured outputs. Such errors are due to the non-ideal frequency response of the controlled nanopositioner. For a CAV spiral, these phase errors can be easily eliminated by adding phase constants α_x and α_y to shape the input signals as

$$X_s = r \cos(\theta + \alpha_x) \quad (5.9)$$

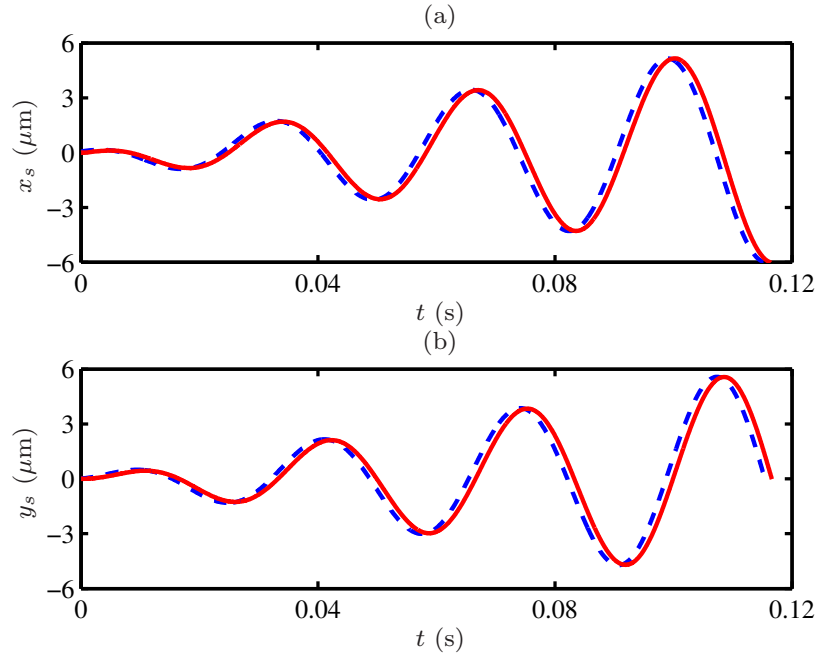


Figure 5.2 : Input signals to be applied to the scanner in the x and y axes of the scanner to generate CAV spiral scan with $\omega = 188.50$ radians/sec. Solid line is the achieved response and dashed line is the desired trajectory.

and

$$Y_s = r \sin(\theta + \alpha_y). \quad (5.10)$$

Here, α_x and α_y are determined by measuring the closed-loop frequency response of the system at the scan frequency. They may also be determined off-line if a model of the system is at hand.

A key advantage of using a CAV spiral is that closed-loop tracking of this pattern when implemented via the cartesian equations only involves tracking single frequency sinusoidal signals with slowly varying amplitudes. This advantage, when combined with the use of the shaped input signals (5.9) and (5.10), enables the AFM's scanner to track a high frequency CAV spiral resulting in fast atomic force microscopy. A drawback of this method is that its linear velocity v is not constant. Thus, it may not be suitable for scanning some samples

where the interaction between the probe and the sample needs to be done at constant linear velocity. The CLV spiral presented next overcomes this problem.

5.1.2 The CLV spiral

In order to generate a CLV spiral, the radius \tilde{r} and angular velocity $\tilde{\omega}$ need to be varied simultaneously in a way that the linear velocity of the nanopositioner is kept constant at all times. The expressions for \tilde{r} and $\tilde{\omega}$ are first derived by substituting $\omega = \frac{v}{r}$ into equation (5.1) to obtain

$$\frac{dr}{dt} = \frac{Pv}{2\pi r} \quad (5.11)$$

where v is the linear velocity of the CLV spiral. Then, equation (5.11) is solved for r by integrating both sides of the equation as

$$\int r dr = \frac{Pv}{2\pi} \int dt. \quad (5.12)$$

For $r = 0$ at $t = 0$, we obtain

$$\tilde{r} = \sqrt{\frac{Pv}{\pi}t}. \quad (5.13)$$

From equation (5.13), by substituting $\tilde{r} = \frac{v}{\tilde{\omega}}$ the expression for $\tilde{\omega}$ is obtained as

$$\tilde{\omega} = \sqrt{\frac{\pi v}{Pt}}. \quad (5.14)$$

It is worth noting that \tilde{r} and $\tilde{\omega}$ are non-linear functions of time, and $\tilde{\omega}$ approaches infinity at $t = 0$. For practical reasons during digital implementation of the CLV spiral, $t = 0$ is approximated with $t = \text{sampling period}$ of the digital system.

The equation for total scanning time \tilde{t}_{total} of a CLV spiral scan can be derived in a similar manner to the CAV spiral. From equation (5.11), \tilde{t}_{total} is derived as

$$\tilde{t}_{total} = \frac{\pi r_{end}^2}{Pv}. \quad (5.15)$$

By choosing $v = \tilde{\omega}_{end} r_{end}$ where $\tilde{\omega}_{end}$ is the instantaneous angular velocity at r_{end} , the equation for \tilde{t}_{total} can be rewritten as

$$\tilde{t}_{total} = \frac{\pi r_{end}}{P\tilde{\omega}_{end}}. \quad (5.16)$$

It can be inferred from equation (5.16) that if $\tilde{\omega}_{end} = \omega$, the total scanning time of a CLV spiral is half of the total scanning time of a CAV spiral. This makes the CAV spiral a more attractive option. However, as we will see later, this gain in scanning time comes at the expense of introducing distortion at the center of the resulting AFM image.

Similar to the CAV spiral, equation (5.13) can be described in cartesian coordinates as

$$\tilde{x}_s = \tilde{r} \cos \tilde{\theta} \quad (5.17)$$

and

$$\tilde{y}_s = \tilde{r} \sin \tilde{\theta} \quad (5.18)$$

where $\tilde{\theta}$ for time varying $\tilde{\omega}$ is obtained as

$$\tilde{\theta} = \sqrt{\frac{4\pi v}{P}} t. \quad (5.19)$$

Fig. 5.3 illustrates the input signals \tilde{x}_s and \tilde{y}_s that can be used to generate a spiral similar to the one shown in Fig. 5.1. However, as illustrated in this figure, the input signals are implemented in a reversed order, that is from r_{end} to r_{start} . To generate a CLV spiral, that starts from $\tilde{r} = 0$, one requires a closed-loop system with extremely high bandwidth (ideally ∞ bandwidth) and a closed loop system with a flat phase and magnitude response. This of course, is not practical. Thus, if the spiral is started from $\tilde{r} = 0$, the initial error that is inevitably generated will propagate all the way through to the end. In the next section, we propose an inversion algorithm that can minimize the tracking error arising from the limited bandwidth and non-ideal frequency response of the closed loop system.

5.1.3 Inversion Technique for CLV spiral

In this section a technique to shape inputs such that the resulting trajectory will be a CLV spiral with minimal tracking error is presented. As the implementation of the entire scheme will be in discrete time, the input shaping method presented here is also described in discrete time.

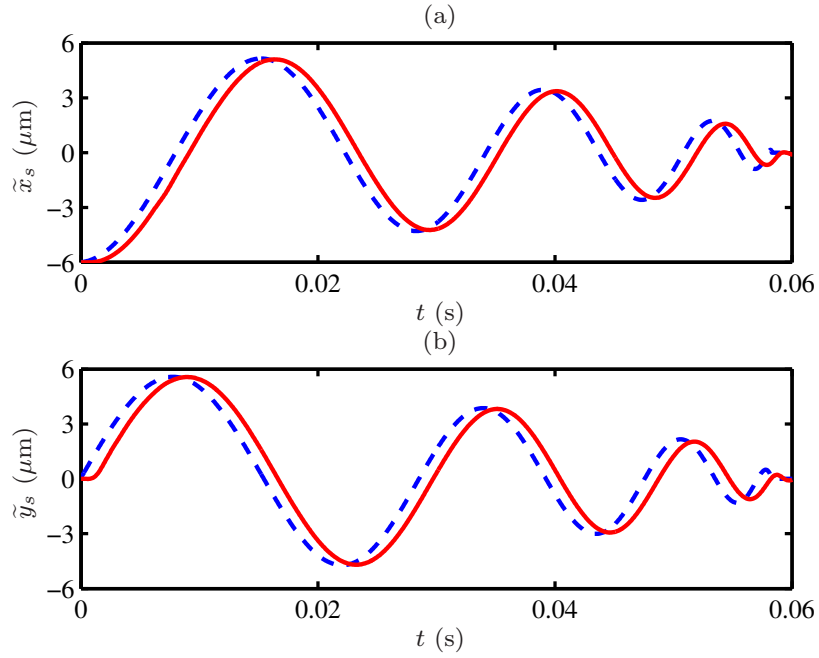


Figure 5.3 : Input signals to be applied to the scanner in the x and y axes of the scanner to generate CLV spiral scan with $v = 1.13$ mm/sec (or $\tilde{\omega}_{end} = 188.50$ radians/sec). Solid line is the achieved response and dashed line is the desired trajectory.

The goal is to design input signals $\{u_x[k]\}_{k=0}^N$ and $\{u_y[k]\}_{k=0}^N$ such that their outputs, along the x and y axis are, $\{x[k] = \tilde{x}(kT)\}_{k=0}^N$ and $\{y[k] = \tilde{y}(kT)\}_{k=0}^N$ respectively. Here, T denotes the sampling interval and \tilde{x} and \tilde{y} are as defined in equations (5.17) and (5.18). In the following only designing of $\{u_x[k]\}_{k=0}^N$ will be described, with the understanding that $\{u_y[k]\}_{k=0}^N$ can be generated by adopting the same procedure.

Assume that the transfer function relating the input and the output along the x direction is given by

$$G_x(z) = \frac{b_0 + b_1 z^{-1} + b_2 z^{-2} + \dots + b_m z^{-m}}{1 + a_1 z^{-1} + a_2 z^{-2} + \dots + a_m z^{-m}}, \quad (5.20)$$

which is stable but has non-minimum phase zeros, i.e. all of zeros are outside the unit circle. As $G_x(z)$ is non-minimum phase, a direct inversion is not possible. Furthermore, as \tilde{x} and \tilde{y} are not periodic, a frequency domain inversion of the type presented in [8] will not

be accurate.

Note that equation (5.20) in the discrete time corresponds to the difference equation

$$\begin{aligned} x[n] + a_1x[n-1] + \dots + a_mx[n-m] \\ = b_0u_x[n] + b_1u_x[n-1] + \dots + b_mu_x[n-m]. \end{aligned} \quad (5.21)$$

This implies

$$\begin{aligned} u_x[n-m] = \frac{1}{b_m} (x[n] + a_1x[n-1] + \dots + a_mx[n-m] \\ - b_nu_x[n] - \dots - b_{m-1}u_x[n-(m-1)]). \end{aligned} \quad (5.22)$$

As $\{x[k]\}_{k=0}^N$ is given, assuming arbitrary values for $u_x[N], u_x[N-1], \dots, u_x[N-(m-1)]$, the input sequence $u_x[N-(m-1)], u_x[N-(m-2)], \dots, u_x[1], u_x[0]$ can be calculated from equation (5.22). As an example consider $m = 2$ in (5.21). This implies

$$\begin{aligned} x[n] + a_1x[n-1] + a_2x[n-2] \\ = b_0u_x[n] + b_1u_x[n-1] + b_2u_x[n-2] \end{aligned} \quad (5.23)$$

and

$$\begin{aligned} u_x[n-2] = \frac{1}{b_2} (x[n] + a_1x[n-1] \\ + a_2x[n-2] - b_0u_x[n] - b_1u_x[n-1]). \end{aligned} \quad (5.24)$$

Setting $u_x[N]$ and $u_x[N-1]$ to arbitrary values, $u_x[N-2]$ can be back calculated from equation (5.24). Similarly, using the calculated $u_x[N-2]$ and the arbitrarily chosen $u_x[N-1]$, $u_x[N-3]$ can be computed. Thus, traversing backwards in time one can compute $u_x[n]$ up to $n = 0$.

The above mentioned procedure can be proved to be stable, and can be shown to converge to an input sequence that would generate the output $\tilde{x}(kT)$. If a user has to deal with a continuous time transfer function $G_x(s)$, he or she could approximate it by a discrete transfer function $G_x(z)$ using the bilinear transformation or any other appropriate approximation technique.

5.1.4 Total scan time: Spiral scan vs. Raster scan

A fair comparison of the total scanning time for a spiral scan and a raster scan can be made by evaluating the time required for both methods to generate images of equal areas and pitch lengths. The area of a circular spiral scanned image A_{spiral} with a radius of r_{end} can be calculated as

$$A_{spiral} = \pi r_{end}^2. \quad (5.25)$$

The area of a rectangular raster scanned image A_{raster} can be calculated using

$$A_{raster} = L^2 \quad (5.26)$$

where L is length of the square image. For both images to have an equal area, equations (5.25) and (5.26) are equated to obtain

$$L = \sqrt{\pi} r_{end}. \quad (5.27)$$

The number of lines in a raster scanned image with pitch P can be calculated as

$$number\ of\ lines = \frac{L}{P} + 1. \quad (5.28)$$

The total scan time to generate a raster scanned image can be obtained using

$$t_{total\ raster} = \frac{number\ of\ lines}{f} \quad (5.29)$$

where f is the scan frequency. Thus, by substituting equations (5.27) and (5.28) into equation (5.29), the total scan time for generating a raster scanned image with an area of πr_{end}^2 can be determined as

$$t_{total\ raster} = \frac{\sqrt{\pi} r_{end}}{Pf} + \frac{1}{f}. \quad (5.30)$$

The total scanning time required to generate a spiral scanned image in a CAV mode can be calculated using equation (5.6) and by substituting $\omega = 2\pi f$ into equation (5.6),

$$t_{total} = \frac{r_{end}}{Pf}. \quad (5.31)$$

It can be deduced from equations (5.30) and (5.31), by ignoring the term $\frac{1}{f}$ in equation (5.30), for the same scan frequency, an image of equal area and pitch can be generated $\sqrt{\pi}$ (≈ 1.77) times faster using a CAV spiral scan than a raster scan.

In order to compare the total scanning time for a CLV spiral scan and a raster scan, the linear velocity of the raster scan $v_r = 2Lf$ is introduced into equation (5.30) to obtain

$$t_{total_raster} = \frac{2\pi r_{end}^2}{Pv_r} \quad (5.32)$$

with the term $\frac{1}{f}$ ignored. It can be deduced from equations (5.32) and (5.15), for the same linear velocity, $v_r = v$, an image of equal area and pitch can be generated two times faster using a CLV spiral scan than a raster scan.

5.1.5 Mapping Spiral Points to Raster Points

In this work, the spiral-scanned images are plotted by mapping the sampling points along the spiral trajectory (called “spiral points”) to points or pixels (called “raster points”) that make up a raster-scanned image placed on top of the spiral points as shown in Fig. 5.4 (a) and (b) for CAV and CLV spirals respectively. A major advantage of mapping the spiral points to the raster points is that it allows the user to utilize existing image processing software developed specifically for raster-scanned images, to modify the generated spiral image.

In this mapping procedure, the dimension of the raster-scanned image is set to *spiral diameter* \times *spiral diameter* where the *spiral diameter* \approx *spiral radius* $\times 2$, and the pitch of the raster-scanned image is chosen to be equal to the pitch P of the spiral. Consequently, the number of lines in the raster-scanned image will be equal to the number of curves in the spiral trajectory. Then, each raster point located within the *spiral radius* is mapped to the nearest spiral point. Since the position of the raster and spiral points are known for any scan frequency and dimension, the nearest spiral point corresponding to each raster point

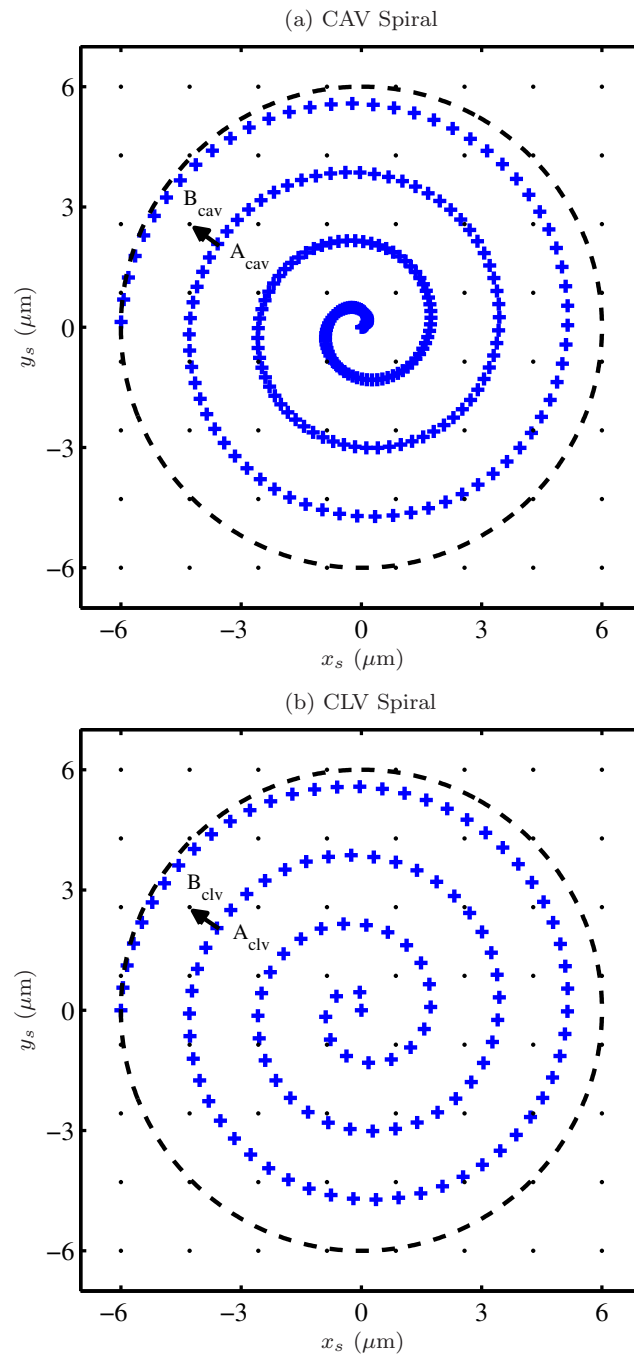


Figure 5.4 : Spiral points (+) for (a) CAV spiral with $\omega_s = 188.5$ radians/s and (b) CLV spiral with $v_s = 1.1$ mm/s. The sampling frequency used for generating these spiral points is 2 kHz. Both spiral trajectories have a $6.5 \mu\text{m}$ radius with *number of curves* = 8. The spiral points are plotted on top of the raster points (.) that make up a $13 \times 13 \mu\text{m}$ raster-scanned image with of 8×8 pixels resolution.

can be identified and stored in an indexed matrix before performing the sample scans. By doing this, the image of the sample can be plotted on the computer in real-time, i.e., as the AFM is scanning the sample.

Fig. 5.4 (a) illustrates that the density of the CAV spiral points increases as r approaches the origin of the spiral. This is because the time taken for the spiral trajectory to make one full spiral circle remains constant due to the constant angular velocity, although the circumference of the spiral circle gets smaller. A disadvantage of this is that, it increases the computing time needed to search for the nearest spiral point corresponding to the each raster point. Nevertheless, Fig. 5.4 (b) shows that the density of the CLV spiral points remain constant for the entire spiral trajectory. This is because in the CLV spiral, the time taken for the spiral trajectory to makes one circle reduces as r approaches the origin of the spiral.

Next, the error introduced by mapping the spiral points to the raster points is analyzed. This mapping error can be determined by calculating the magnitude of the vector between the nearest spiral point corresponding to the each raster point. Fig. 5.4 (a) illustrates an example of the vector between spiral point A_{cav} and raster point B_{cav} which corresponds to raster point (2,6). The magnitude of this vector can be calculated as

$$\left| AB_{cav}^{(i,j)} \right| = \sqrt{(A_{cav}^x - B_{cav}^x)^2 + (A_{cav}^y - B_{cav}^y)^2} \quad (5.33)$$

where $i = 2$ and $j = 6$. Similar calculation can be performed on the CLV spiral to evaluate the magnitude of the vector between spiral point A_{clv} and raster point B_{clv} as shown in Fig. 5.4 (b).

5.2 Controller Design

This section addresses design of feedback controllers undertaken in this work. The feedback controllers for the x and y axes were designed in a similar fashion to the PPF control

scheme described in Chapter 4. However in this work both axes are driven using the home made DC-accurate charge amplifiers. The key objectives of the controller design are to achieve good damping ratio for the first resonant mode of the piezoelectric tube scanner and to achieve a high closed-loop bandwidth to allow accurate tracking of the CAV and CLV spirals. Although the use of CAV spiral allows us to select the frequencies that will not excite the resonance of the scanner, it is still important to actively damp the scanner. External vibration and noise can result in perturbations in the AFM image if scanner's mechanical resonance is not damped. The need to damp the scanner becomes more important when it is used to track a CLV spiral input. This is because the CLV spiral input consists of high frequency components that will inevitably excite the mechanical resonance of the scanner. Additionally, the feedback controller can minimize the effect of piezoelectric creep that can cause further perturbations in the image. Overall, the feedback controllers resulted in a high-bandwidth (540 Hz) closed-loop system. It is worth mentioning that tracking of the spiral trajectory can be done in open-loop by shaping the input signals.

5.3 Results

5.3.1 Tracking Performance

The performance of the closed-loop systems were then evaluated for fast tracking of the CAV and CLV spirals. Both types of spiral were setup to produce spiral scans with $r_{end} = 6.5 \mu\text{m}$ and *number of curves* = 512, i.e. the diameter of the resulting circular image consists of 512 pixels. Fig. 5.5 (a) to (f) illustrate tracking trajectories of the CAV spirals for $\omega_s = 31.4, 94.3, 188.5, 565.5, 754.0$ and 1131.0 radians/s. This corresponds to scanning frequencies of $f_s = 5, 15, 30, 90, 120$ and 180 Hz, respectively. In order to allow visual comparison of the tracking trajectories, plots in Fig. 5.5 (a) to (f) were made to display only the trajectories between $\pm 0.15 \mu\text{m}$. It can be observed that the use of the designed feedback controllers and the shaped input have resulted in excellent tracking performance of the CAV spirals. In order to quantify the tracking performance, the RMS tracking errors between the

Table 5.1 : RMS values of tracking error and total scanning time for CAV and CLV spiral scans. Images have a resolution of 512×512 pixels.

CAV Spiral			CLV Spiral		
ω_s (radians/s)	E_{RMS} (nm)	t_{total} (s)	v_s (mm/s)	E_{RMS} (nm)	\tilde{t}_{total} (s)
31.4	2.81	51.10	0.19	3.60	25.55
94.3	4.60	17.03	0.57	7.26	8.52
188.5	5.19	8.52	1.13	10.67	4.26
565.5	10.38	2.84	-	-	-
754.0	11.30	2.13	-	-	-
1131.0	18.16	1.42	-	-	-

desired and the achieved trajectories were calculated and are tabulated in Table 5.1. The RMS tracking error is defined as

$$E_{RMS} = \sqrt{\frac{1}{t_{total}} \int_0^{t_{total}} (r(t) - r_a(t))^2 dt} \quad (5.34)$$

where r is the desired trajectory (or the radius) and $r_a = \sqrt{c_x^2 + c_y^2}$ is the achieved trajectory.

Table 5.1 shows that E_{RMS} increases as the spiral frequency increases. This increase is mainly due to the inability of the feedback controller to accurately track the rapid changes in the amplitude of the spiral inputs as ω_s is increased. Nevertheless, at $\omega_s = 1130.97$ radians/s, E_{RMS} still remains relatively low, i.e. only 0.15 % of the maximum scanning range (spiral's diameter).

Fig. 5.5 (g), (h) and (i) illustrate the tracking trajectories between $\pm 0.30 \mu\text{m}$ of the CLV spirals for $v_s = 0.2, 0.6$ and 1.1 mm/s. The values of v_s were calculated using $v_s = \tilde{\omega}_{end} r_{end}$ where $\tilde{\omega}_{end} = 31.4, 94.3$ and 188.5 radians/s. As mentioned earlier, the CLV spiral scans were implemented in a reversed order, that is from r_{end} to r_{start} . Fig. 5.5 (g) shows

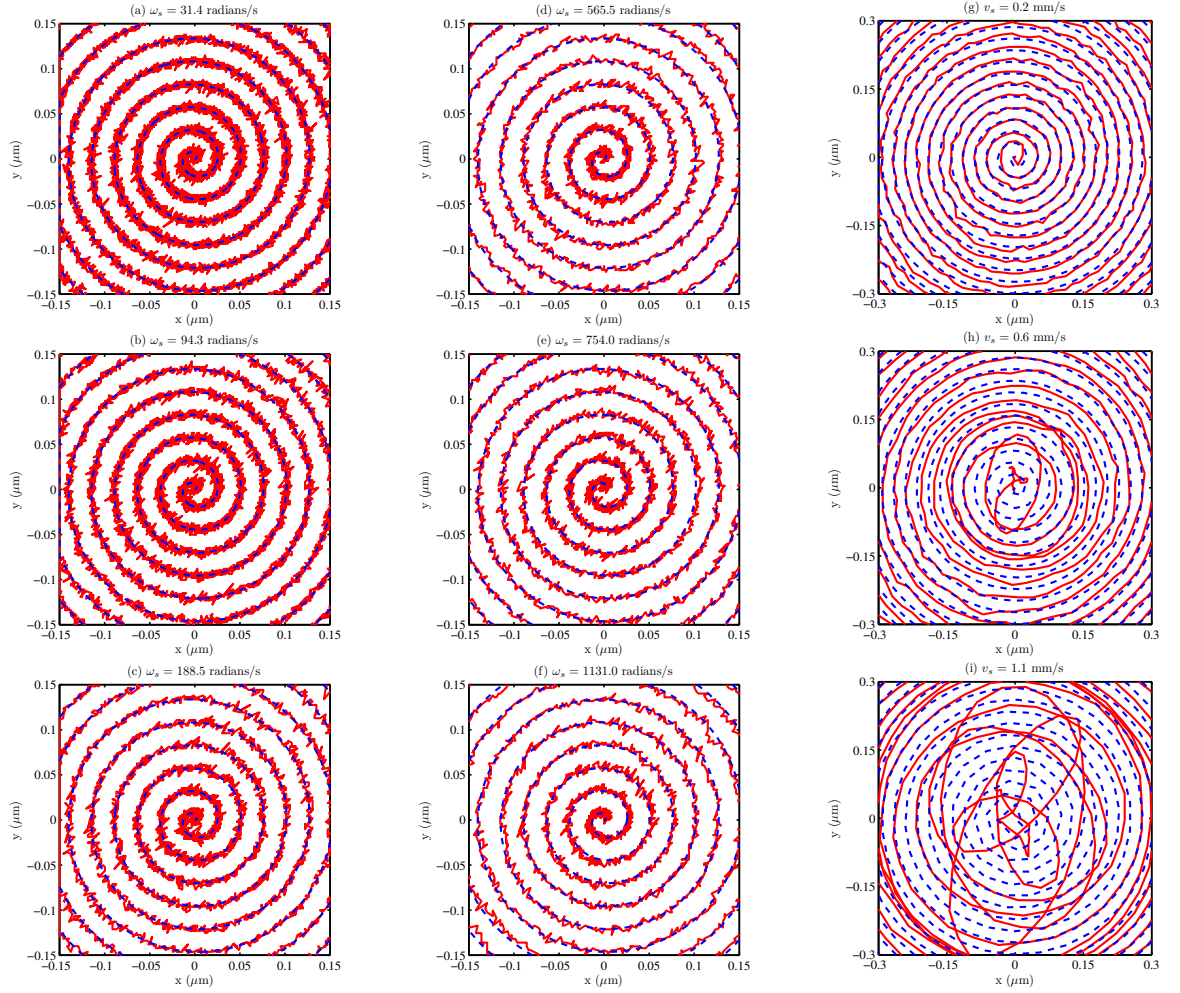


Figure 5.5 : First two columns: (a) - (f) Tracking trajectories of CAV spirals between $\pm 0.15 \mu\text{m}$ in closed-loop for $\omega_s = 31.4, 94.3, 188.5, 565.5, 754.0$ and 1131.0 radians/s. Third column: (g) - (i) Tracking trajectories of CLV spirals between $\pm 0.30 \mu\text{m}$ in closed-loop for $v_s = 0.2, 0.6$ and 1.1 mm/s. The pitch of the spirals was set at 25.44 nm. Solid line is the achieved response and dashed line is the desired trajectory.

that relatively good tracking was obtained for $v_s = 0.2$ mm/s. However for $v_s = 0.6$ and 1.1 mm/s, Fig. 5.5 (h) and (i) illustrate very little tracking were achieved in a small region surrounding the center of the spirals where the frequency components of the input signals have increased to well beyond the bandwidth of the closed-loop system. Nonetheless, Table 5.1 shows that the E_{RMS} for the CLV spirals is still relatively small since most of the tracking errors were limited only to the center of the resulting spiral scan.

5.3.2 AFM Imaging

Having analyzed the performance of the closed-loop system in tracking the CAV and CLV spirals, we then moved on to investigate the use of spiral scanning in generating AFM images. The spiral scans were setup to produce images with $r_{end} = 6.5 \mu\text{m}$ and *number of curves* = 512, i.e., the diameter of the resulting circular image consists of 512 pixels. However before performing the spiral scans, the RMS of mapping errors $E_{map_{RMS}}$ for the CAV and CLV spirals scans at different angular and linear velocities are calculated and tabulated in Table 5.2. Note that, different sampling frequencies f_{samp} were used in order to minimize the computing time for searching the nearest spiral point corresponding the each raster point. Additionally, the sampling frequency is also limited by computational power of the dSPACE rapid prototyping system. Table 5.2 shows that the $E_{map_{RMS}}$ are very small and less than the pitch of the spiral trajectory and the raster points, i.e., 25.44 nm. Thus, they can be ignored.

A calibration grating NT-MDT TGQ1 with a 20 nm feature-height and a 3 μm period was used as an imaging sample. The AFM was setup to scan the sample in constant-height contact mode using a contact AFM probe with a nominal spring constant of 0.2 N/m and resonance frequency of about 12 kHz. The constant-height contact mode was used here as the commercial AFM controller that controls the vertical positioning of the scanner is not fast enough to track the sample topography for fast scans. During each scan, the AFM probe is deflected due to its interactions with the sample. The probe deflection was measured and

Table 5.2 : RMS values of spiral to raster points mapping error for CAV and CLV spiral scans.

CAV Spiral			CLV Spiral		
ω_s (radians/s)	f_{samp} (kHz)	E_{mapRMS} (nm)	v_s (mm/s)	f_{samp} (kHz)	E_{mapRMS} (nm)
31.4	10	2.49	0.19	10	2.61
94.3	20	2.64	0.57	20	2.83
188.5	20	3.12	1.13	20	3.49
565.5	40	3.42	-	-	-
754.0	60	3.51	-	-	-
1131.0	60	3.75	-	-	-

later used to construct AFM images of the sample topography. Figs. 5.6 (a) to (f) illustrate AFM images generated using the CAV spiral scans with $\omega_s = 31.4, 94.3, 188.5, 565.5, 754.0$ and 1131.0 radians/s.

Figs. 5.7 (a) to (c) illustrate the cross-section curves of these spiral scanned images at about $y = 0 \mu\text{m}$. The cross-section curves were taken in parallel to the square profile of the calibration grating. Note that, we used the probe deflection measurement of $f_s = 5$ Hz scan to calibrate the probe deflection measurements of other scan frequencies to the height of the calibration grating. This is possible because the probe deflection is very small and thus linear. It can be observed from Figs. 5.6 and 5.7 that the obtained images are of a good quality and the lateral and vertical profiles of the calibration grating are well captured. In particular, the images are free from typical distortions caused by tracking errors, scanner vibrations, hysteresis and creep. It is also worth mentioning that the area around the edges of the images was also well imaged. However, during fast scans with $\omega_s = 565.5$ radians/s and above, a wave-like artifact can be observed around the outer edges of the AFM images.

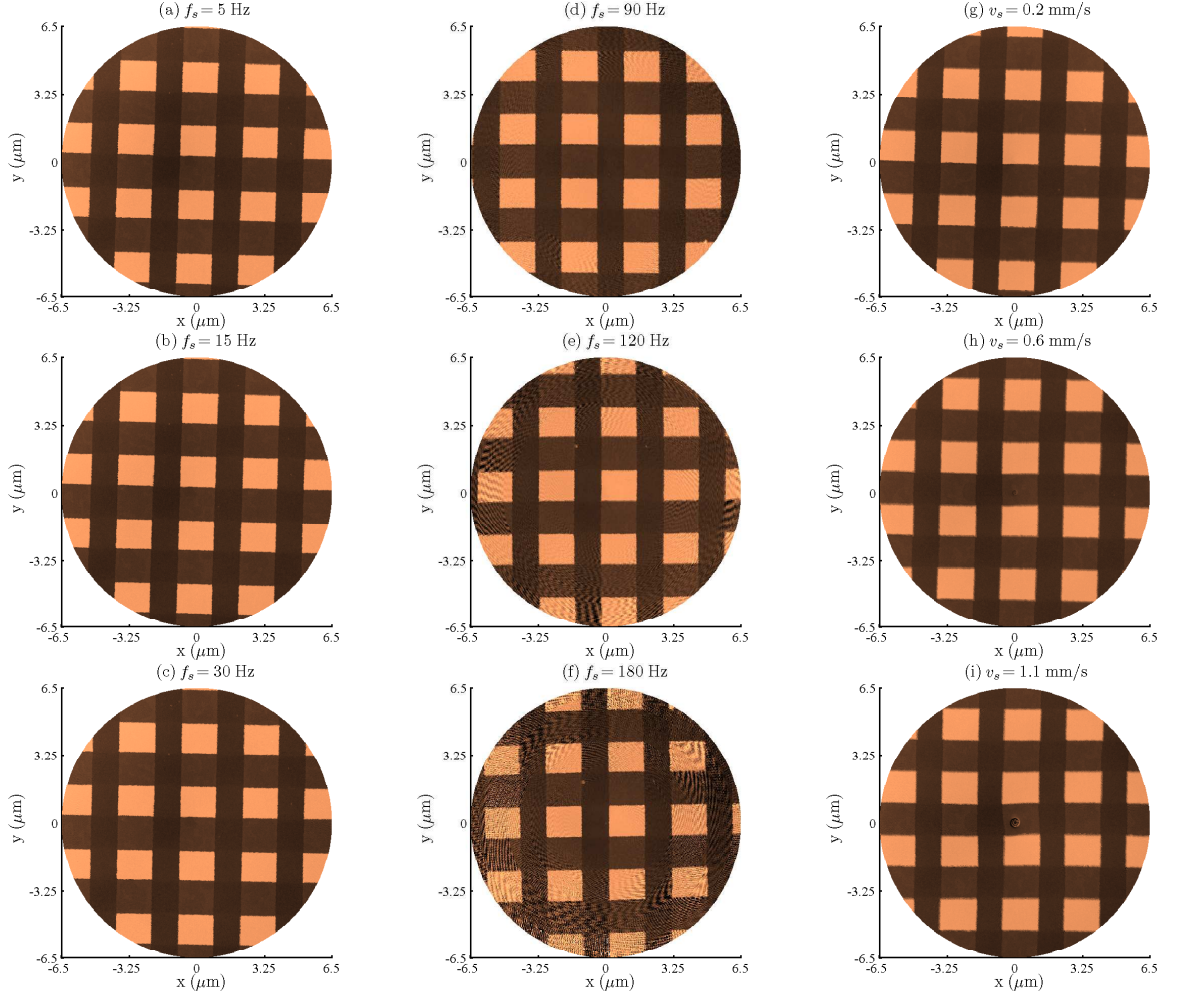


Figure 5.6 : AFM images of NT-MDT TGQ1 grating scanned in closed-loop using the CAV spiral scanning mode for (a) - (f) $f_s = 5, 15, 30, 90, 120$ and 180 Hz (which corresponds to $\omega_s = 31.4, 94.3, 188.5, 565.5, 754.0$ and 1131.0 radians/s) and using the CLV spiral scanning mode for (g) - (i) $v_s = 0.2, 0.6$ and 1.1 mm/s. The *number of curves* for these AFM images was set to 512.

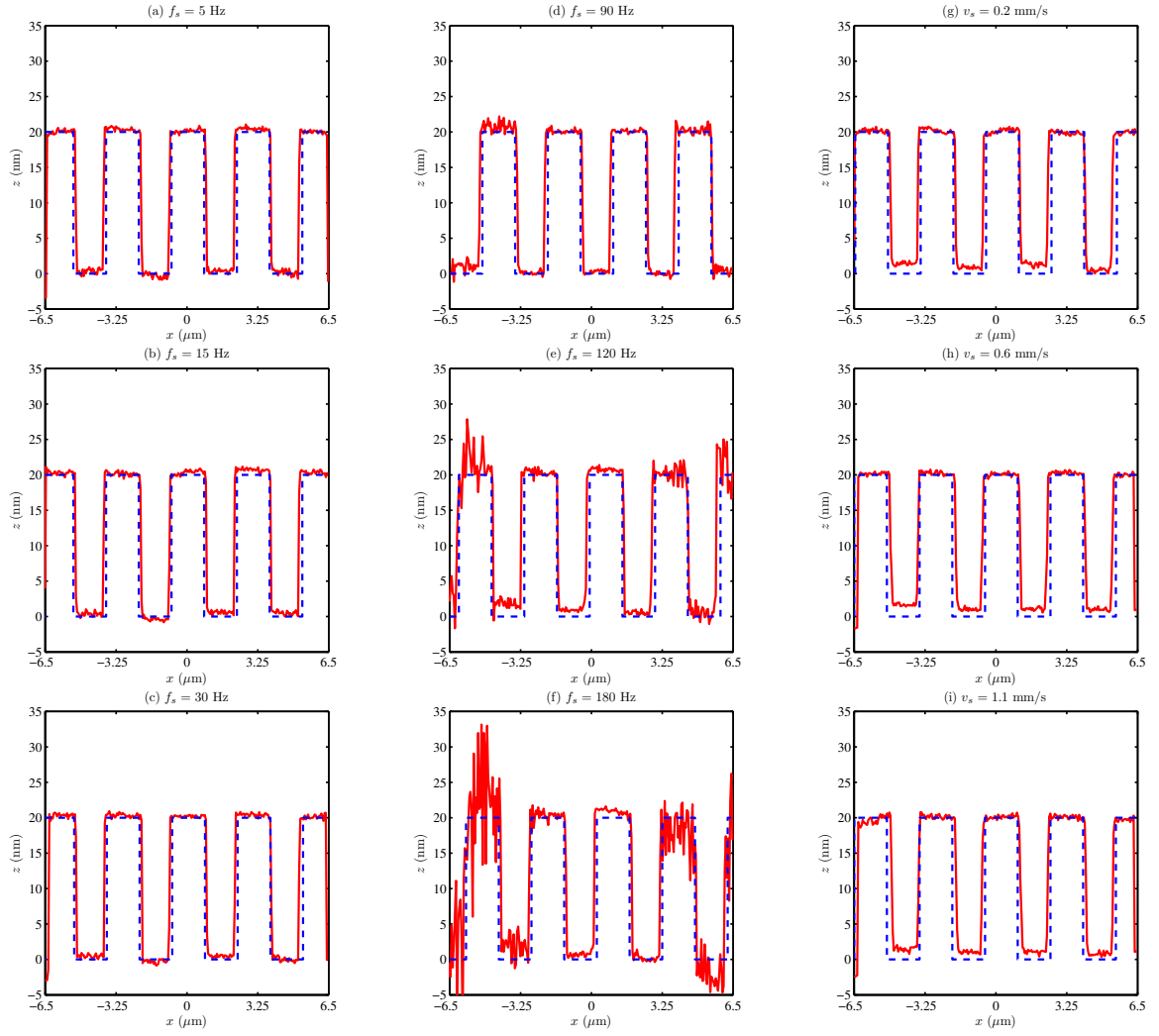


Figure 5.7 : Cross-section (solid) and reference (dash) curves of the AFM images illustrated in Fig. 5.6 (a) to (i). The cross-section curves were taken about the center of the AFM images and parallel to the square profile of the calibration grating.

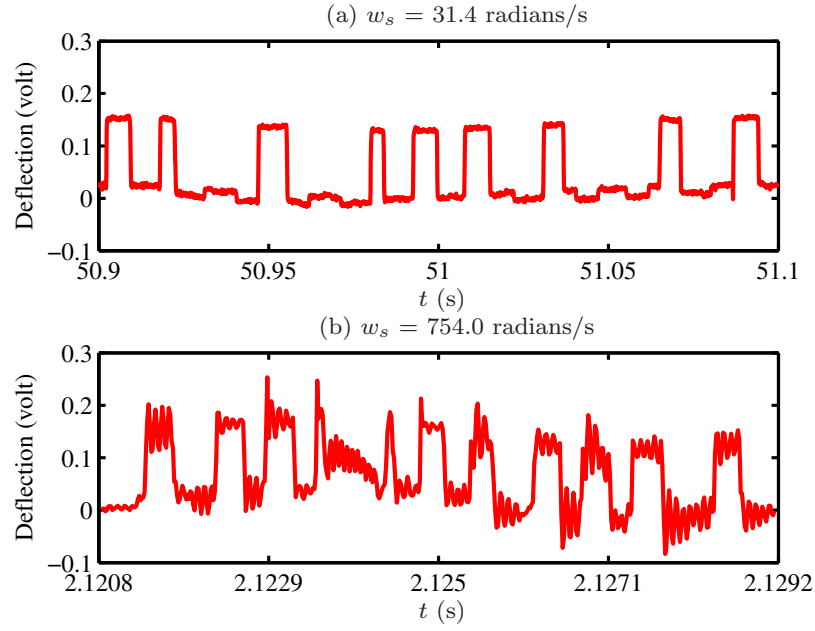


Figure 5.8 : Probe deflection signals showing the profile of the calibration grating for (a) $\omega_s = 31.4$ radians/s and (b) $\omega_s = 754.0$ radians/s.

Upon a closer examination of the probe deflection signals, we found that the wave-like artifacts were a result of the excitation of the probe's resonance (≈ 12 kHz). Fig. 5.8 illustrates the probe deflection signals between $r = 5.98$ and $6.00 \mu\text{m}$ for $\omega_s = 31.4$ and 754.0 radians/s. Fig. 5.8 (a) shows that during a low-speed scan the probe deflection signal is free of probe's vibrations. However, at a fast scan, Fig. 5.8 (b) shows that due to the existence of sharp corners in the topography of the sample, as the probe goes through a full circle, it faces step-like changes that tend to excite its resonance frequency. This effect is much more profound when the sample is scanned at high frequencies. Thus, the image quality can be improved by using a stiffer micro-cantilever. This should allow for much higher scan frequencies, approaching the first resonance of the scanner.

Next, a similar AFM setting was used to generate similar images using the CLV spiral scanning mode. Fig. 5.6 (g), (h) and (i) illustrate the generated AFM images for $v_s = 0.2$,

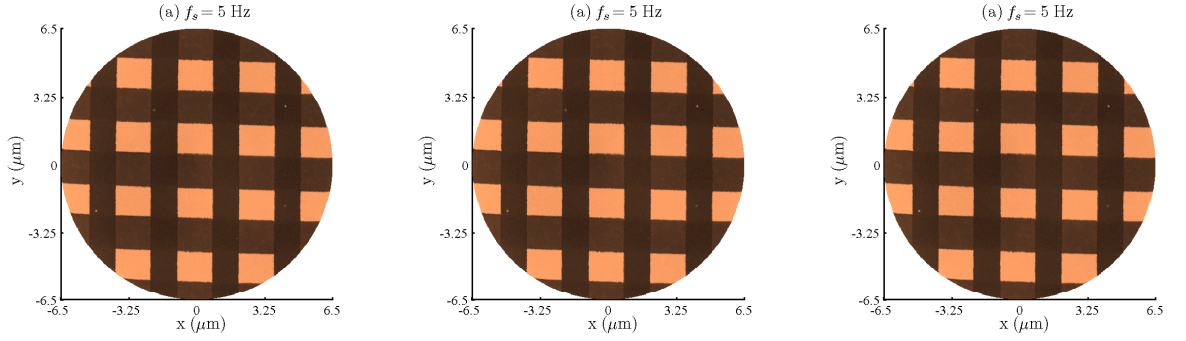


Figure 5.9 : AFM images of NT-MDT TGQ1 grating scanned in open-loop using the CAV spiral for (a) - (c) $f_s = 5, 30$, and 90 Hz. The *number of curves* for these AFM images was set to 512.

0.6 and 1.1 mm/s. For $v_s = 0.2$ mm/s, it can be observed that the profile of the calibration grating was well imaged. This is in agreement with the good tracking performance achieved at this scanning speed as illustrated in Fig. 5.5 (g). However, for higher values of v_s , Fig. 5.6 (h) and (i) illustrate that a small hole-like artifact is formed at the center of each image. This is due to the loss of tracking control when the frequency components of the input signals have increased to well beyond the bandwidth of the closed-loop system. The lack of tracking control has also resulted in a slightly skewed AFM image around the center of the spiral for $v_s = 1.1$ mm/s.

Finally, we would like to evaluate the capability of the CAV spiral scans in generating the AFM images when operated in open loop . The use of single frequency input as mentioned in Section 5.1.1 would allow the open-loop tracking of the CAV spirals to be performed rather accurately. However, to achieve this, one has to deal with the nonlinearities of the piezoelectric tube scanner, particularly with hysteresis and creep. In this work, the effect of hysteresis was significantly reduced by the use of the charge amplifiers instead of voltage amplifiers to drive both axes of the scanner. As for the creep, its effect was minimized by simply waiting a considerable amount of time for it to disappear before performing the scans. Fig. 5.9 (a), (b) and (c) illustrate AFM images generated using the CAV

spiral scans operated in open loop for $f_s = 5, 30$ and 90 Hz. It can be observed from these images that the spiral scanning method works surprisingly well when operated in open-loop. This could be partially due to the fact that by controlling charge, we have managed to substantially minimize the effect of hysteresis. However, even if the scanner were driven with voltage amplifiers, the hysteresis nonlinearity could have been compensated for by perturbing the input signal. This would be rather straight forward due to the single-tone nature of signals applied to the x - and y - electrodes of the piezoelectric tube scanner.

5.4 Summary

In this chapter, we demonstrated how CAV and CLV spiral scans can be used to obtain AFM images. It is possible to achieve fast atomic force microscopy using the CAV spiral scanning, but other issues like the vibrations in the AFM probe need to be considered and addressed. The use of CLV mode spiral scanning requires a high-bandwidth controller for accurate tracking of the input signals. Apart from the above mentioned artifacts formed at the center of the CLV spiral, the obtained AFM images have good qualities. We also demonstrated that the proposed method could work well without using a feedback controller around the AFM scanner. The possibility of using spiral scanning in other SPM applications such as STM should also be explored in the future.

Chapter 6

Conclusions

This thesis explored several ways of improving the speed and accuracy of piezoelectric tube scanners, in particular, for the use in atomic force microscopy. First, a high-bandwidth low-noise controller was designed for a prototype piezoelectric tube scanner by utilizing displacement measurements from a capacitive sensor and voltage signals induced in the piezoelectric tube. Here, a two-input one-output H_∞ controller was designed to utilize the capacitive sensor measurements at low frequencies (below 100 Hz), including at DC, and the induced piezoelectric voltage signal for higher frequency measurements. By keeping the capacitive sensor bandwidth low, the effect of sensor noise on the overall system is significantly reduced. For RMS value of the sensor noise below 1 nm, the designed H_∞ controller achieves a closed-loop bandwidth more than three times that can be obtained from a controller utilizing the low frequency capacitive sensor measurement alone.

Second, the focus of this thesis was shifted from a prototype piezoelectric tube scanner to one used in a commercially available AFM. The use of the AFM allow for a more thorough and a reliable evaluation of performance of our control schemes. The implementation of controllers in the commercial AFM was not a trivial task as it involved integration of a dSPACE rapid prototyping system and external voltage and charge sources into the electronic components of the device. Additionally, development of Matlab codes for generating raster inputs and plotting the scanned images were also need to be done. Here, a PPF control scheme was designed and implemented for vibration and cross-coupling compensation in the lateral axes of the AFM's piezoelectric tube scanner. The implementation of the PPF control scheme resulted in a high closed-loop bandwidth (300 Hz), and a damping of more

than 30 dB at the scanner's first resonant mode. These improvements were achieved with a third order controller that is very straightforward to implement using either analog or digital methods. Experimental results show that by implementing the PPF control scheme, relatively good AFM images in comparison with a well-tuned PI controller (the AFM standard controller) can still be obtained up to line-scan of 60 Hz, i.e., beyond the 30 Hz scan frequency set by the AFM standard software.

Finally, a spiral scanning method for fast atomic force microscopy was described in this thesis. The equations needed to generate the spiral scans in CAV and CLV modes were derived. Comparison between the CAV and CLV modes were made in order to evaluate the advantages and disadvantages of each mode. In the CAV spiral scan, the use of the single frequency input signals allows for scanning to be performed at very high speeds without exciting the resonance of the scanner. In this work, experimental results obtained by implementing this scanning method on a commercial AFM indicate that the obtained images are of a good quality and the profile of the calibration grating is well captured up to scan frequency of 180 Hz with a scanner where the first resonance frequency is 580 Hz. It was found that the accuracy and quality of the images obtained at higher scanning speed were limited by the resonance frequency of the micro-cantilever. By using a stiffer micro-cantilever, much higher scan frequencies approaching the mechanical bandwidth of the piezoelectric tube scanner are possible. Nevertheless, in the CAV mode, the linear velocity of the spiral trajectory is not constant. This may not be suitable for scanning samples where the interaction between the probe and the sample needs to be done at constant linear velocity.

In the CLV spiral scan, the linear velocity is kept constant by varying the input frequency according the position of the spiral trajectory with respect to the origin of the spiral. In order to perform fast scanning in CLV spiral scan, a high bandwidth feedback controller is needed to track the spiral trajectory. Tracking error as a result of limited bandwidth of

the feedback controller can be constrained to a small region around the origin of the spiral, where the frequency of the input signal is very high, by implementing the scan in a reversed order. That is, starting from the outer radius through to the origin of the spiral. A comparison in terms of the total scanning time between the spiral scan and the raster scan was also performed. It was derived that for the same scan frequency, an image of equal area and pitch could be generated $\sqrt{\pi}$ (≈ 1.77) times faster using a CAV spiral scan than a raster scan. As for the CLV spiral, for the same linear velocity, an image of equal area and pitch can be generated two times faster using a CLV spiral scan than a raster scan.

Future works of this thesis should include studies of ways to compensate unwanted motions along the vertical axis of the piezoelectric tube during the scanning motion in the x - y plane. The main sources of these motions are the vertical translations due to the lateral deflection of the piezoelectric tube and the induced vibrations due to the excitation of the out-of-plane resonant modes. It is important to minimize the unwanted motions because they will interact directly with the measuring probe and cause errors in the scanned images. The idea of using “complementary” sensor for achieving high-bandwidth low-noise controller should be evaluated further by using the scanner to obtain AFM images. The possibility of obtaining atomic resolution AFM images at high speed by using this scanner in closed-loop should be sufficient to motivate this evaluation. The use of spiral scanning in AFM should be expanded. Experiments should be carried out to evaluate the effect of using stiffer micro-cantilever in order to generate accurate and high quality AFM images at higher scanning speeds. The prospect of using spiral scanning in dynamic AFM mode and other SPM applications such as STM should also be explored in the future.

Bibliography

- [1] T. R. Albrecht, P. Grutter, D. Horne, and D. Rugar, *Frequency modulation detection using high- q cantilevers for enhanced force microscope sensitivity*, J. Appl. Phys. **69** (1991), no. 2, 668–673.
- [2] W. T. Ang, F.A. Garmon, P.K. Khosla, and C.N. Riviere, *Modeling rate-dependent hysteresis in piezoelectric actuators*, Intelligent Robots and Systems, 2003. (IROS 2003). Proceedings. 2003 IEEE/RSJ International Conference on, vol. 2, Oct. 2003, pp. 1975 – 1980 vol.2.
- [3] S. S. Aphale, S. Devasia, and S. O. R. Moheimani, *High-bandwidth control of a piezoelectric nanopositioning stage in the presence of plant uncertainties*, Nanotechnology **19** (2008), no. 12, 125503 (9pp).
- [4] S.S. Aphale, B. Bhikkaji, and S.O.R. Moheimani, *Minimizing scanning errors in piezoelectric stack-actuated nanopositioning platforms*, Nanotechnology, IEEE Transactions on **7** (2008), no. 1, 79–90.
- [5] R. C. Barrett and C. F. Quate, *Optical scan-correction system applied to atomic force microscopy*, Review of Scientific Instruments **62** (1991), no. 6, 1393 – 1399.
- [6] R. Ben Mrad and H. Hu, *A model for voltage-to-displacement dynamics in piezoelectric actuators subject to dynamic-voltage excitations*, Mechatronics, IEEE/ASME Transactions **7** (2005), no. 4, 479 – 489.
- [7] B. Bhikkaji and S. O. R. Moheimani, *Integral resonant control of a piezoelectric tube actuator for fast nanoscale positioning*, Mechatronics, IEEE/ASME Transactions on **13** (2008), no. 5, 530 – 537.

- [8] B. Bhikkaji, M. Ratnam, A.J. Fleming, and S.O.R. Moheimani, *High-performance control of piezoelectric tube scanners*, Control Systems Technology, IEEE Transactions on **15** (2007), no. 5, 853 – 866.
- [9] B. Bhikkaji, M. Ratnam, and S. O. R. Moheimani, *Pvpf control of piezoelectric tube scanners*, Sensors and Actuators A: Physical **135** (2007), no. 2, 700 – 712.
- [10] B. Bhushan, *Springer handbook of nanotechnology*, Springer, 2006.
- [11] G. Binnig, C. F. Quate, and Ch. Gerber, *Atomic force microscope*, Phys. Rev. Lett. **56** (1986), no. 9, 930–933.
- [12] G. Binnig and H. Rohrer, *Scanning tunneling microscopy*, Helv. Phys. Acta **55** (1982), 726–735.
- [13] G. Binnig, H. Rohrer, Ch. Gerber, and E. Weibel, *7 x 7 Reconstruction on Si(111) Resolved in Real Space*, Phys. Rev. Lett. **50** (1983), no. 2, 120–123.
- [14] G. Binnig and D. P. E. Smith, *Single-tube threedimensional scanner for scanning tunneling microscopy*, Rev. Sci. Instrum. **57** (1986), no. 8, 1688–1689.
- [15] R. Comstock, *Charge control of piezoelectric actuators to reduce hysteresis effect*, U.S. Patent 4.263,527, 1981.
- [16] D. Croft, G. Shed, and S. Devasia, *Creep, hysteresis, and vibration compensation for piezoactuators: Atomic force microscopy application*, J. Dyn. Sys., Meas., Control **123** (2001), no. 1, 35 – 43.
- [17] A. Daniele, S. Salapaka, M.V. Salapaka, and M. Dahleh, *Piezoelectric scanners for atomic force microscopes: Design of lateral sensors, identification and control*, American Control Conference, 1999. Proceedings of the 1999, vol. 1, 1999, pp. 253 – 257 vol.1.

- [18] S. Devasia, E. Eleftheriou, and S.O.R. Moheimani, *A survey of control issues in nanopositioning*, Control Systems Technology, IEEE Transactions on **15** (2007), no. 5, 802 – 823.
- [19] D. M. Eigler and E. K. Schweizer, *Positioning single atoms with a scanning tunneling microscope*, Nature **344** (1990), 524–526.
- [20] O.M. El Rifai and K. Youcef-Toumi, *Coupling in piezoelectric tube scanners used in scanning probe microscopes*, American Control Conference, 2001. Proceedings of the 2001, vol. 4, 2001, pp. 3251 – 3255 vol.4.
- [21] R. Erlandsson, L. Olsson, and P. Martensson, *Inequivalent atoms and imaging mechanisms in ac-mode atomic-force microscopy of si(111)7 x 7*, Phys. Rev. B **54** (1996), no. 12, R8309–R8312.
- [22] J. L. Fanson and T. K. Caughey, *Positive position feedback-control for large space structures*, AIAA Journal **28** (1990), no. 4, 717 – 724.
- [23] T. Fett and G. Thun, *Determination of room-temperature tensile creep of pzt*, Journal of Materials Science Letters **17** (1998), no. 22, 1929 – 1931.
- [24] A. J. Fleming and S. O. R. Moheimani, *Improved current and charge amplifiers for driving piezoelectric loads, and issues in signal processing design for synthesis of shunt damping circuits*, Journal of Intelligent Material Systems and Structures **15** (2004), no. 2, 77 – 92.
- [25] A. J. Fleming and S. O. R. Moheimani, *A grounded-load charge amplifier for reducing hysteresis in piezoelectric tube scanners*, Review of Scientific Instruments **76** (2005), no. 7, 073707.
- [26] ———, *Sensorless vibration suppression and scan compensation for piezoelectric tube nanopositioners*, Control Systems Technology, IEEE Transactions on **14** (2006), no. 1, 33 – 44.

- [27] A.J. Fleming and K.K. Leang, *Charge drives for scanning probe microscope positioning stages*, Ultramicroscopy **108** (2008), no. 12, 1551 – 1557.
- [28] A.J. Fleming and S.O.R. Moheimani, *Precision current and charge amplifiers for driving highly capacitive piezoelectric loads*, Electronics Letters **39** (2003), no. 3, 282 – 284.
- [29] A.J. Fleming, A. Wills, and S.O.R. Moheimani, *Sensor fusion for improved control of piezoelectric tube scanners*, Advanced Intelligent Mechatronics, 2007 IEEE/ASME International Conference on, Sept. 2007, pp. 1 – 6.
- [30] A.J. Fleming, A.G. Wills, and S. Moheimani, *Sensor fusion for improved control of piezoelectric tube scanners*, Control Systems Technology, IEEE Transactions on **16** (2008), no. 6, 1265 – 1276.
- [31] P. Ge and M. Jouaneh, *Modeling hysteresis in piezoceramic actuators*, Precision Engineering **17** (1995), no. 3, 211–221.
- [32] F. J. Giessibl, *Atomic resolution of the silicon (111)-(7 x 7) surface by atomic force microscopy*, Science **267** (1995), no. 5194, 68–71.
- [33] G. C. Goodwin, S. F. Graebe, and M. E. Salgado, *Control system design*, Prentice Hall International, New Jersey, 2001.
- [34] A. D. L. Humphris, J. K. Hobbs, and M. J. Miles, *Ultrahigh-speed scanning near-field optical microscopy capable of over 100 frames per second*, Applied Physics Letters **83** (2003), no. 1, 6 – 8.
- [35] H. Jung, J. Y. Shim, and D. Gweon, *New open-loop actuating method of piezoelectric actuators for removing hysteresis and creep*, Review of Scientific Instruments **71** (2000), no. 9, 3436–3440.

- [36] A. N. Labinsky, G. A. J. Reynolds, and J. Halliday, *A disk recording system and a method of controlling the rotation of a turn table in such a disk recording system*, WO **93/13524** (2001).
- [37] B. P. Lathi, *Linear systems and signals*, 2nd ed, Oxford University Press, 2004.
- [38] K. Leang and S. Devasia, *Hysteresis, creep, and vibration compensation for piezoactuators: Feedback and feedforward control*, Dec. 2002, pp. 283 – 289.
- [39] K.K. Leang and S. Devasia, *Feedback-linearized inverse feedforward for creep, hysteresis, and vibration compensation in AFM piezoactuators*, Control Systems Technology, IEEE Transactions on **15** (2007), no. 5, 927 – 935.
- [40] C. Lee and S. M. Salapaka, *Robust broadband nanopositioning: Fundamental trade-offs, analysis, and design in a two-degree-of-freedom control framework*, Nanotechnology **20** (2009), no. 3, 035501 (16pp).
- [41] S.-H. Lee and T. J. Royston, *Modeling piezoceramic transducer hysteresis in the structural vibration control problem*, J. Acoust. Soc. Am. **108** (2000), no. 6, 2843 – 2855.
- [42] Y Li and Y. Bechhoefer, *Feedforward control of a closed-loop piezoelectric translation stage for atomic force microscope*, Review of Scientific Instruments **78** (2007), no. 1, 013702.
- [43] I. A. Mahmood and S. O. R. Moheimani, *Making a commercial atomic force microscope more accurate and faster using positive position feedback control*, Review of Scientific Instruments **80** (2009), no. 6, 063705.
- [44] I.A. Mahmood, S. O. R. Moheimani, and K. Liu, *Tracking control of a nanopositioner using complementary sensors*, Nanotechnology, IEEE Transactions on **8** (2009), no. 1, 55 – 65.

- [45] Y. Martin and H. K. Wickramasinghe, *Magnetic imaging by “force microscopy” with 1000 resolution*, Appl. Phys. Lett. **50** (1987), no. 20, 1455–1457.
- [46] Y. Martin, C. C. Williams, and H. K. Wickramasinghe, *Atomic force microscope force mapping and profiling on a sub 100-Å scale*, J. Appl. Phys. **61** (1987), no. 10, 4723–4729.
- [47] T. McKelvey, H. Akcay, and L. Ljung, *Subspace-based multivariable system identification from frequency response data*, Automatic Control, IEEE Transactions on **41** (1996), no. 7, 960 – 979.
- [48] T. McKelvey, A. Fleming, and S. O. R. Moheimani, *Subspace-based system identification for an acoustic enclosure*, Journal of Vibration and Acoustics **124** (2002), no. 3, 414 – 419.
- [49] M. L. Meade, *Lock-in amplifiers: Principles and applications*, P. Peregrinus on behalf of the Institution of Electrical Engineers, 1983.
- [50] E. Meyer, H. J. Hug, and R. Bennewitz, *Scanning probe microscopy*, Springer, Germany, 2004.
- [51] V. L. Mironov, *Fundamentals of scanning probe microscopy*, Nizhniy Novgorod, 2004.
- [52] S. O. R. Moheimani, *Invited review article: Accurate and fast nanopositioning with piezoelectric tube scanners: Emerging trends and future challenges*, Rev. Sci. Instrum. **79** (2008), no. 7, 071101(1–11).
- [53] S. O. R. Moheimani and A. J. Fleming, *Piezoelectric transducers for vibration control and damping*, Springer, Germany, 2006.
- [54] S.O.R. Moheimani, B.J.G. Vautier, and B. Bhikkaji, *Experimental implementation of extended multivariable ppf control on an active structure*, Control Systems Technology, IEEE Transactions on **14** (2006), no. 3, 443 – 455.

- [55] B. Mokaberi and A.A.G. Requicha, *Compensation of scanner creep and hysteresis for AFM nanomanipulation*, Automation Science and Engineering, IEEE Transactions on **5** (2008), no. 2, 197 – 206.
- [56] C.V. Newcomb and I. Flinn, *Improving the linearity of piezoelectric ceramic actuators*, Electronics Letters **18** (1982), no. 11, 442 – 444.
- [57] N. Oyabu, Y. Sugimoto, M. Abe, and O. Custance, *Lateral manipulation of single atoms at semiconductor surfaces using atomic force microscopy*, Nanotechnology **16** (2005), 112–117.
- [58] A. Pantazi, A. Sebastian, H. Pozidis, and E. Eleftheriou, *Two-sensor-based h_∞ control for nanopositioning in probe storage*, Decision and Control, 2005 and 2005 European Control Conference. CDC-ECC '05. 44th IEEE Conference on, Dec. 2005, pp. 1174 – 1179.
- [59] R. Pintelon and J. Schoukens, *System identification: A frequency domain approach*, IEEE Press, New York, 2001.
- [60] D. W. Pohl, W. Denk, and M. Lanz, *Optical stethoscopy - image recording with resolution $\lambda/20$* , Appl. Phys. Lett. **44** (1984), no. 20, 651–653.
- [61] K. H. Rew, J. H. Han, and I. Lee, *Multi-modal vibration control using adaptive positive position feedback*, Journal of Intelligent Material Systems and Structures **13** (2002), no. 1, 13 – 22.
- [62] R. S. Robinson, *Interactive computer correction of piezoelectric creep in scanning tunneling microscopy images*, Journal of Computer-Assisted Microscopy **2** (1996), no. 1, 53–58.
- [63] D. Rugar, H. J. Mamin, P. Guethner, S. E. Lambert, J. E. Stern, I. McFadyen, and Yogi T., *Magnetic force microscopy: General principles and application to longitudinal recording media*, J. Appl. Phys. **68** (1990), no. 3, 1169–1183.

- [64] J. W. Rutter, *Geometry of curves*, Chapman and Hall/CRC, Boca Raton, 2000.
- [65] S. Salapaka, A. Sebastian, J. P. Cleveland, and M. V. Salapaka, *High bandwidth nano-positioner: A robust control approach*, Rev. Sci. Instrum. **73** (2002), no. 9, 3232–3241.
- [66] S. Salapaka, A. Sebastian, J.P. Cleveland, and M.V. Salapaka, *Design, identification and control of a fast nanopositioning device*, American Control Conference, 2002. Proceedings of the 2002, vol. 3, 2002, pp. 1966–1971 vol.3.
- [67] G. Schitter, P. Menold, H. F. Knapp, F. Allgower, and A. Stemmer, *High performance feedback for fast scanning atomic force microscopes*, Review of Scientific Instruments **72** (2001), no. 8, 3320 – 3327.
- [68] G. Schitter and M. J. Rost, *Scanning probe microscopy at video-rate*, Material Today **11** (2008), no. 1, 40–48.
- [69] G. Schitter and A. Stemmer, *Identification and open-loop tracking control of a piezo-electric tube scanner for high-speed scanning-probe microscopy*, Control Systems Technology, IEEE Transactions on **12** (2004), no. 3, 449 – 454.
- [70] A. Sebastian and S.M. Salapaka, *Design methodologies for robust nano-positioning*, Control Systems Technology, IEEE Transactions on **13** (2005), no. 6, 868–876.
- [71] G. Song, S. P. Schmidt, and B. N. Agrawal, *Experimental robustness study of positive position feedback control for active vibration suppression*, Journal of Guidance, Control and Dynamics **25** (2002), no. 1, 179 – 182.
- [72] A. Stemmer, G. Schitter, J. M. Rieber, and F. Allgower, *Control strategies towards faster quantitative imaging in atomic force microscopy*, European Journal of Control **11** (2005), 4 – 5.

- [73] Y. Sugimoto, M. Abe, S. Hirayama, N. Oyabu, O. Custance, and S. Morita, *Atom inlays performed at room temperature using atomic force microscopy*, Nature Mater. **4** (2005), 156–160.
- [74] J. E. Szymanski, *Basic mathematics for electronic engineers: Models and applications*, Van Nostrand Reinhold International, London, 1989.
- [75] N. Tamer and M. Dahleh, *Feedback control of piezoelectric tube scanners*, Decision and Control, 1994., Proceedings of the 33rd IEEE Conference on, vol. 2, Dec 1994, pp. 1826 – 1831 vol.2.
- [76] T. Uchihashi, M. Tanigawa, M. Ashino, Y. Sugawara, K. Yokoyama, S. Morita, and M. Ishikawa, *Identification of b-form dna in an ultrahigh vacuum by noncontact-mode atomic force microscopy*, Langmuir **16** (2000), 1349–1353.
- [77] B. J. G. Vautier and S. O. R. Moheimani, *Charge-driven piezoelectric actuators for structural vibration control: Issues and implementation*, Smart Materials and Structures **14** (2005), no. 4, 575 – 586.
- [78] Wenlin Zhang, Lei Miao, Yunhui Zheng, Zaili Dong, and Ning Xi, *Feedback control implementation for AFM contact-mode scanner*, Nano/Micro Engineered and Molecular Systems, 2008. NEMS 2008. 3rd IEEE International Conference on, Jan. 2008, pp. 617–621.
- [79] Q. Zhonga, D. Innissa, K. Kjollerb, and V.B. Elingsb, *Fractured polymer/silica fiber surface studied by tapping mode atomic force microscopy*, Surface Science **290** (1993), no. 1-2, L688–L692.

Appendix

This appendix consists three publications that are outcomes from the author's early PhD studies. However, the results from these publications are not included in the main body of this thesis as they are in a different field. The inclusion of these publications here is to provide a complete picture of his PhD work.

Precise Tip Positioning of a Flexible Manipulator Using Resonant Control

Iskandar A. Mahmood, S. O. Reza Moheimani, *Senior Member, IEEE*, and Bharath Bhikkaji

Abstract—A single-link flexible manipulator is fabricated to represent a typical flexible robotic arm. This flexible manipulator is modeled as an SIMO system with the motor torque as the input and the hub angle and the tip position as the outputs. The two transfer functions are identified using a frequency-domain system identification method, and the resonant modes are determined. A feedback loop around the hub angle response with a resonant controller is designed to damp the resonant modes. A high-gain integral controller is also implemented to achieve zero steady-state error in the tip position response. Experiments are performed to demonstrate the effectiveness of the proposed control scheme.

Index Terms—Flexible manipulator, integral controller, resonant controller, tip positioning.

I. INTRODUCTION

INCREASING demands for high-speed manipulation and high payload-to-weight ratio in robot manipulators has triggered a significant growth in research and development activities on flexible manipulators. These manipulators constitute a suitable choice to realize such demands since they are light in weight, require only small-sized actuators and consume low energy for actuation [1]. However, designing feedback controllers to operate these systems at high speeds is a challenging task. The control system must be designed not only for precise tip positioning but also for suppressing vibrations associated with the flexible nature of the manipulator.

In order to achieve higher precision in the tip positioning, the use of tip position measurement is essential. In [2], Cannon and Schmitz initiated the experiment to control the tip positioning of a flexible manipulator by using measurements from a tip position sensor as a feedback input. They designed an linear quadratic Gaussian (LQG) controller and the obtained results suggested a satisfactory step response with accurate tip positioning. However, the LQG controller was not robust with respect to modeling errors. Since then many researchers, such as [3]–[8], have used the tip position measurement as feedback input to control the positioning of flexible manipulators.

In [6], the authors presented a two-feedback-loop control scheme to improve the closed-loop system robustness of the controller proposed in [2]. The controllers in the inner and outer loop were of LQG and H_∞ designs, respectively. The LQG controller was designed to introduce sufficient damping to the

flexural modes and the H_∞ controller was designed for the purpose of increasing robustness and disturbance attenuation. Their simulation results illustrated an improvement in the closed-loop system robustness. However, the control scheme resulted in a high-order controller. A two-feedback-loop control scheme was also implemented by Feliu *et al.* in [4]. The inner and outer loops were used to control the motor position and tip position, respectively. In the outer loop, in contrast to [2], the motor position was used as the control signal instead of the current. As a result, the motor response needs to be significantly fast in order to counter the motion produced by the vibrational modes of the arm, making this method ineffective to suppress high-frequency vibrations. In [9] and [10], direct strain feedback (DSFB) control strategy was used to suppress the vibrations in a flexible manipulator. This control strategy managed to increase the stiffness of the flexible manipulator and caused it to undergo smaller vibration levels while in motion. It was noted in [9] that from a practical engineering perspective, this control strategy is only suitable for speed reference motor, where only the strain signal is needed for feedback. However, if a torque control motor is used, the time rate of change of strain, which is difficult to measure, is needed for feedback.

In this paper, an experimental flexible manipulator setup is fabricated to represent a typical flexible robotic arm. Frequency-domain system identification is used to model the flexible manipulator, and a control scheme is developed such that vibrations are suppressed using a collocated measurement while tip positioning is achieved using a noncollocated measurement. The control scheme consists of two feedback loops with each feedback loop having a specific purpose. The inner loop contains a resonant controller that adds damping to the flexible manipulator. It utilizes the hub angle measurement provided by a shaft encoder and guarantees that the closed-loop system remains stable in the presence of out-of-bandwidth dynamics, as described in [11] and [12]. In the outer loop, an integral controller is implemented for precise tip positioning using measurements of the tip deflection and hub angle. The integral controller ensures zero steady-state error for a step input.

Successful utilizations of resonant controllers for vibration suppression in flexible structures have been reported in [11] and [12]. This paper reports the first-time application of this control design approach to flexible manipulators. At the time of this writing, it is not known how an optimal resonant controller can be designed. This is mainly due to the nonconvex nature of the optimization problem associated with the minimization of a specific performance index. In this paper a graphical approach is proposed, which results in resonant controllers with satisfactory performance.

Manuscript received March 18, 2007; revised September 13, 2007. Recommended by Technical Editor S. Chiaverini. This work was supported by the Australian Research Council.

The authors are with the School of Electrical Engineering and Computer Science, University of Newcastle, Callaghan, NSW 2308, Australia (e-mail: iskandar.mahmood@newcastle.edu.au; reza.moheimani@newcastle.edu.au; bharath.bhikkaji@newcastle.edu.au).

Digital Object Identifier 10.1109/TMECH.2008.918494



Fig. 1. Flexible manipulator.

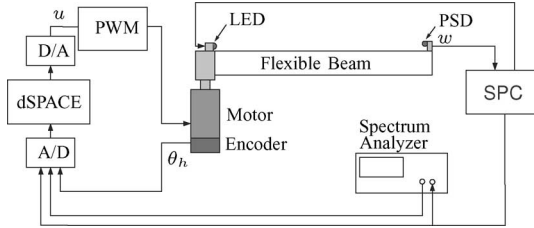


Fig. 2. Experimental setup for the flexible manipulator.

The remainder of the paper is arranged as follows. Section II provides a description of the experimental setup. Modeling and identification of the system transfer functions are presented in Section III. Control schemes are devised in Section IV. In Section V, simulation and experimental results are presented to illustrate the effectiveness of the proposed control schemes. Finally, conclusions are drawn in Section VI.

II. EXPERIMENTAL SETUP

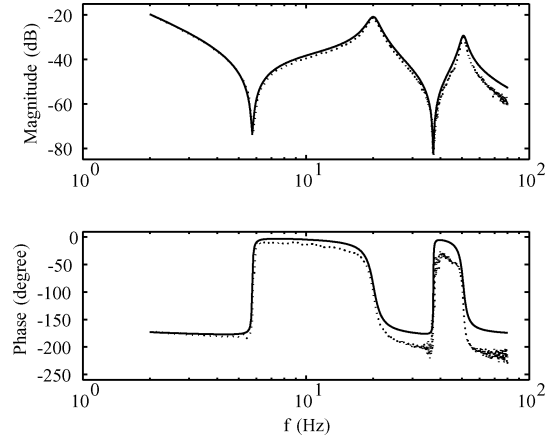
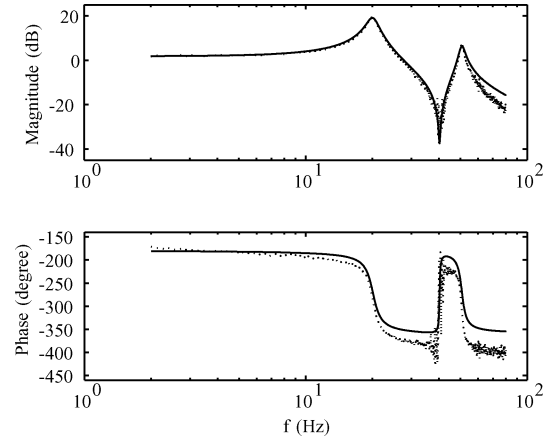
The flexible manipulator used here consists of an aluminum beam ($0.6 \text{ m} \times 0.05 \text{ m} \times 0.003 \text{ m}$) clamped directly to the shaft of a Glentek GM4040-41 dc brush servo motor. An illustration of the experimental setup is presented in Figs. 1 and 2. The motor was driven by a Glentek GA377 pulse width modulation (PWM) servomotor amplifier. The motor has a continuous stall torque of $3.54 \text{ N}\cdot\text{m}$ and a maximum bandwidth of 58 Hz . The shaft encoder of the motor was used to measure the hub angle of rotation. It has a count of 5000 per revolution, i.e., a resolution of 0.072° .

An infrared light-emitting diode (LED) and a Hamamatsu S1352 position sensitive detector (PSD) were used for measuring the tip deflection of the beam. The LED was fixed on top of the hub. A Hamamatsu C5923 signal processing circuit (SPC) was used to drive the infrared LED and also to convert the photocurrents into a voltage signal, the magnitude of which is proportional to the spot light position on the sensor surface. A dSPACE DS1103 controller board was used for real-time controller implementation. A sampling frequency of 20 kHz was used in order to avoid aliasing.

III. MODELING AND SYSTEM IDENTIFICATION

In order to accurately model the system for control design, an experimental approach to modeling (system identification) is taken. The following frequency response functions (FRFs) are determined for designing the control system:

$$G_{\theta_h u}(i\omega) \triangleq \frac{\theta_h(i\omega)}{u(i\omega)} \quad (1)$$


Fig. 3. Identified model (—) and experimental (···) frequency response of amplifier input voltage u to hub angle θ_h .

Fig. 4. Identified model (—) and experimental (···) frequency response of amplifier input voltage u to tip deflection w_{tip} .

and

$$G_{w_{\text{tip}} u}(i\omega) \triangleq \frac{w_{\text{tip}}(i\omega)}{u(i\omega)} \quad (2)$$

where $u(t)$ is the input voltage, $\theta_h(t)$ is the hub angle measured by the shaft encoder, $w_{\text{tip}}(t) = w(L, t)$ is the flexural tip deflection measured by the PSD. It is worth noting that the tip position $y_{\text{tip}}(t) \triangleq y(L, t)$ can be described by $y(L, t) = w(L, t) + L\theta_h(t)$, which leads to the expression

$$G_{y_{\text{tip}} u}(i\omega) = G_{w_{\text{tip}} u}(i\omega) + LG_{\theta_h u}(i\omega). \quad (3)$$

A dual-channel HP35670A spectrum analyzer was used for determining the FRFs. A band-limited random noise signal ($2\text{--}102 \text{ Hz}$) was generated using the spectrum analyzer and applied to the motor as the input, $u(t)$. The corresponding outputs $\theta_h(t)$ and $w_{\text{tip}}(t)$ were also recorded using the spectrum analyzer. The input–output data was processed to generate the FRFs (1) and (2) in a nonparametric form. In Figs. 3 and 4 the nonparametric FRFs of (1) and (2) are plotted along with the corresponding

parametric fits

$$G_{\theta_h u}(s) = \frac{420.73(s^2 + 0.5028s + 1305)}{s(s + 1.65)s^2 + 15.35s + 1.596 \times 10^4} \times \frac{s^2 + 1.437s + 5.462 \times 10^4}{s^2 + 20.9s + 1.015 \times 10^5} \quad (4)$$

and

$$G_{w_{tip} u}(s) = \frac{-31153.01}{s^2 + 15.35s + 1.596 \times 10^4} \times \frac{s^2 + 3.108s + 6.386 \times 10^4}{s^2 + 20.9s + 1.015 \times 10^5}. \quad (5)$$

Note that the poles characterizing flexible modes of the beam in $G_{\theta_h u}(s)$ and $G_{w_{tip} u}(s)$ are identical. This property is common to all flexible structures. Data beyond 80 Hz were discarded in Figs. 3 and 4 as these frequencies were far beyond the maximum bandwidth of the motor. Fig. 3 illustrates the collocated nature of $G_{\theta_h u}(s)$, where the phase is always between 0° and -180° .

IV. CONTROLLER DESIGN

This section discusses and details the control design scheme proposed in this paper. The control scheme consists of two negative feedback loops. The inner loop is designed to add damping to the flexible manipulator and the outer loop provides precise tip positioning.

A. Resonant Controller Design (Inner Loop Controllers)

Feedback controllers that increase the effective damping and at the same time guarantee unconditional stability of the closed-loop system are always preferred since they avoid closed-loop instabilities due to spillover effects [13]. It is known that collocated velocity feedback controllers [13] possess such properties. However, the implementation of this controller requires the realization of a differentiator, which is not possible for systems with large bandwidth. Another drawback of the velocity feedback controller is that it results in a high control effort over all frequencies. Ideally, for vibration damping purposes, the control effort should be restricted to the resonance frequencies only. Resonant controllers are a class of feedback controllers that guarantee unconditional closed-loop stability of collocated systems, [11], [14]. The model structure of resonant controllers is such that they approximate a differentiator over a narrow bandwidth around the resonance frequencies of the structure. The motivations for their model structure comes from passive RL network controllers used for piezoelectric shunt damping, see [15] and [16]. A detailed discussion on the connections between passive RL network controllers and resonant controllers can be found in [17].

As the poles characterizing the flexible modes of $G_{\theta_h u}(s)$ and $G_{y_{tip} u}(s)$ are identical, system resonances can be damped by designing a feedback loop around either $G_{\theta_h u}(s)$ or $G_{y_{tip} u}(s)$. Here, $G_{\theta_h u}(s)$ is chosen as its collocated nature guarantees an unconditional closed-loop stability with resonant controllers. Damping can be achieved by shifting the closed-loop poles of $G_{\theta_h u}(s)$ deeper into the left-half plane (LHP).

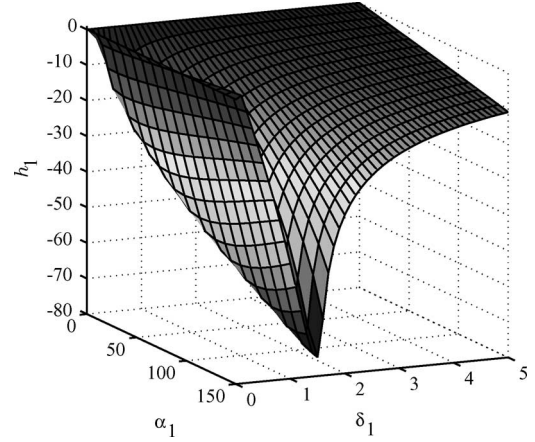


Fig. 5. Plot of the distance between the open-loop and closed-loop poles h_1 versus α_1 and δ_1 , for the first flexible mode.

In the current context, the resonant controller can be parameterized as

$$K^\alpha(s) = \sum_{i=1}^N \frac{\alpha_i s^2}{s^2 + 2\delta_i \omega_i s + \omega_i^2} \quad (6)$$

where $\alpha_i, \beta_i, \delta_i$, and ω_i are the design parameters and N is the number of modes that need to be controlled [12]. As only the first two resonant modes are considered, N is set to 2, which implies

$$K^\alpha(s) = K_1^\alpha(s) + K_2^\alpha(s) \quad (7)$$

where

$$K_i^\alpha(s) = \frac{\alpha_i s^2}{s^2 + 2\delta_i \omega_i s + \omega_i^2}, \quad i = 1, 2. \quad (8)$$

As mentioned in Section I, an optimal resonant controller design has not yet been reported. The approach taken here to determine the parameters is similar to the one mentioned in [11], where each resonant filter is determined independently. It is possible to do so since interactions of the resonant filters are marginally coupled. As the filters $K_1^\alpha(s)$ and $K_2^\alpha(s)$ are targeted to damp the first and the second resonant modes of the plant, the values of ω_1 and ω_2 are set to the first and second resonance frequencies of the beam, respectively. In order to determine the other parameters, the following method is adopted. Assume that only $K_1^\alpha(s)$ exists in the feedback loop. The values of α_1 and δ_1 are chosen such that the absolute value of the difference h_1 between the real parts of the open-loop and closed-loop poles corresponding to the first resonant mode is maximized. Fig. 5(a) shows that for a given range of α_1 ($0 \leq \alpha_1 \leq 150$), there exists a value of δ_1 that maximizes the absolute value of h_1 . Similarly to determine α_2 and δ_2 , it is assumed that the filter $K_1^\alpha(s)$ is not part of the feedback loop and α_2 and δ_2 are chosen such that the difference h_2 , between the real parts of the open-loop and closed-loop poles corresponding to the second resonant mode, is maximized. Fig. 5(b) illustrates that for a given range of α_2 ($0 \leq \alpha_i \leq 150$), there exists a value of δ_2 that maximizes the absolute value of h_2 . The controller obtained by using the

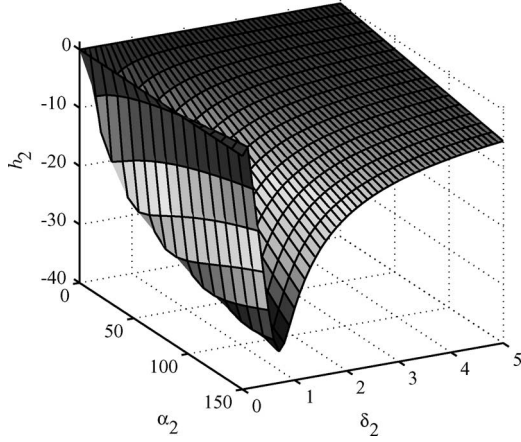


Fig. 6. Plot of the distance between the open-loop and closed-loop poles h_2 versus α_2 and δ_2 , for the second flexible mode.

aforesaid method is

$$K^\alpha(s) = \frac{150s^2}{s^2 + 378.3s + 1.59 \times 10^4} + \frac{150s^2}{s^2 + 445.8s + 1.014 \times 10^5}. \quad (9)$$

Note that in closed loop, the resonant controller $K^\alpha(s)$ will not shift the pole located at the origin. This can be seen by setting $G_{\theta_h u}(s) = a(s)/sb(s)$, $G_{y_{tip} u}(s) = m(s)/sb(s)$, and $K^\alpha(s) = s^2 p(s)/q(s)$, where $a(s)$, $b(s)$, $m(s)$, $p(s)$, and $q(s)$ are appropriately defined, and noting that

$$\begin{aligned} G_{\theta_h u_o}^{(cl)}(s) &= \frac{G_{\theta_h u}(s)}{1 + K^\alpha(s) G_{\theta_h u}(s)} \\ &= \frac{1}{s} \left(\frac{a(s)q(s)}{q(s)b(s) + sp(s)a(s)} \right) \end{aligned} \quad (10)$$

and

$$\begin{aligned} G_{y_{tip} u_o}^{(cl)}(s) &= \frac{G_{y_{tip} u}(s)}{1 + K^\alpha(s) G_{\theta_h u}(s)} \\ &= \frac{1}{s} \left(\frac{m(s)q(s)}{q(s)b(s) + sp(s)a(s)} \right). \end{aligned} \quad (11)$$

B. Outer Loop for Positioning

Here, an integral controller $K_{Int} = K_I/s$ is designed for the outer feedback loop to achieve precise tip positioning. The controller is designed such that the tip response to a step input would satisfy the following specifications: 1) zero steady-state tip position error, 2) rise time and settling time of less than 1 and 1.5 seconds, respectively; and 3) overshoot of less than 2%. However, direct application of an integral controller to $G_{y_{tip} u_o}^{(cl)}(s)$ can be problematic (11). This can be verified by observing the root locus of the net closed-loop tip response

$$\frac{K_I/s G_{y_{tip} u_o}^{(cl)}(s)}{1 + K_I/s G_{y_{tip} u_o}^{(cl)}(s)} \quad (12)$$

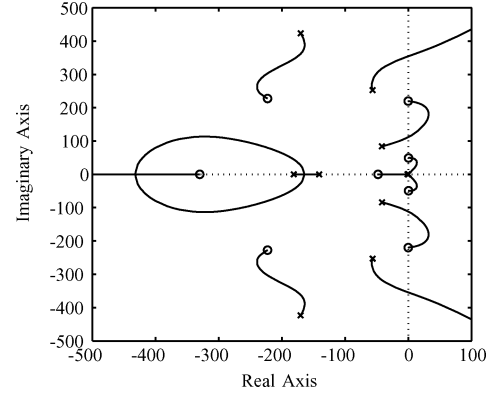


Fig. 7. Roots locus for $G_{y_{tip} u}(s)$ with resonant controller $K^\alpha(s)$ and integral controller K_I/s in the feedback loops, as K_I increases.

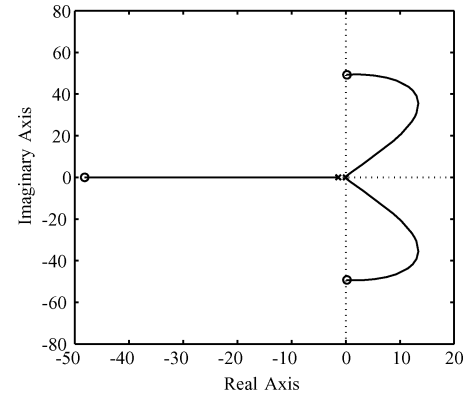


Fig. 8. Enlarged roots locus for $G_{y_{tip} u}(s)$ with resonant controller $K^\alpha(s)$ and integral controller K_I/s in the feedback loops, as K_I increases.

obtained by varying K_I . The locus plot is presented in Fig. 7(a) and shows that for any $K_I \geq 0$, the closed-loop transfer function (12) is unstable. In Fig. 7(b), an enlarged version of Fig. 7(a) around the origin is presented. It shows two locus paths starting from the origin and lying entirely in the right-half plane (RHP) thereafter, demonstrating instability.

A standard way to correct this problem is to add a compensator $C(s)$ to the resonant controller, *i.e.*, replace the resonant controller $K^\alpha(s)$ by $K_a(s) = K^\alpha(s) + C(s)$, so that the pole at the origin is shifted into the LHP; see Fig. 9 for an illustration. In order to avoid a large increase in the model order of the controller and, at the same time push the pole at the origin well into the LHP, a phase-lead compensator, $C(s) = K_{pl}(s + z)/(s + p)$ where K_{pl} , z , and p are the design parameters, is used. Here, the parameters are determined through pole placement, following guidelines in [18, Ch. 10]. Here we set the compensator, $C(s) = 70(s + 10)/s + 70$, which implies that the augmented resonant controller is equal to

$$K_a(s) = \frac{70(s + 10)}{s + 70} + \frac{150s^2}{s^2 + 378.3s + 1.59 \times 10^4} + \frac{150s^2}{s^2 + 445.8s + 1.014 \times 10^5}. \quad (13)$$

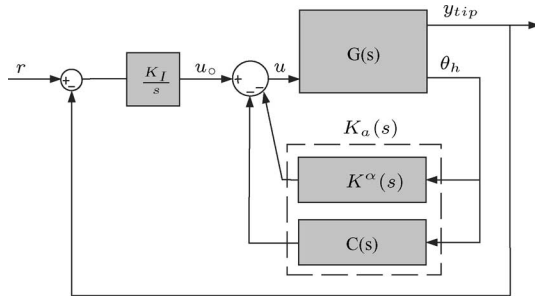


Fig. 9. Augmented resonant controller $K_a(s)$ and integral controller.

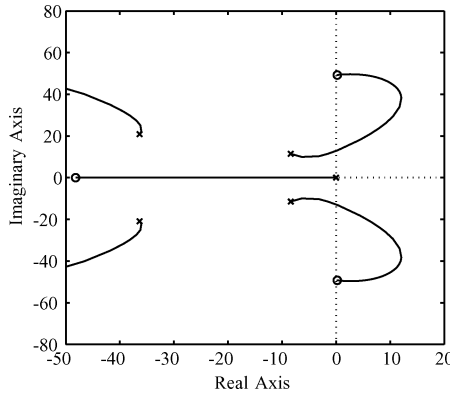


Fig. 10. Enlarged roots locus for $G_{y_{tip}u}(s)$ with augmented resonant controller $K_a(s)$ and integral controller in the feedback loops, as K_I is varied.

Fig. 10 shows an enlarged root locus of (12) with $K^\alpha(s)$ replaced by $K_a(s)$. It can be seen that by shifting the system pole at the origin into the LHP, some parts of the two locus paths are in the LHP, allowing for some values of K_I to result in a stable closed-loop system.

V. SIMULATIONS AND EXPERIMENTAL RESULTS

This section presents simulation and experimental results obtained from the control scheme proposed in this paper.

A. Resonant and Integral Controller

The performance of the augmented resonant controller $K_a(s)$ was evaluated first. Fig. 11 shows the simulated and measured closed-loop frequency responses of $G_{\theta_h u}(s)$. It is evident that the experimental results match the simulations except near the second resonant mode. This is due to the fact that the second resonance is very close to the maximum bandwidth of the motor. The frequency range of the simulated frequency response was extended to cover 1–100 Hz range to illustrate that the pole at $s = 0$ has been shifted to the left by the phase-lead compensator.

In Fig. 12, experimentally determined closed-loop frequency responses of $G_{\theta_h u}(s)$ and $G_{w_{tip}u}(s)$ are plotted along with their corresponding open-loop frequency responses. A significant damping in the first and second resonances of both $G_{\theta_h u}(s)$ and $G_{w_{tip}u}(s)$ is evident from the plots. In particular, Fig. 12(a) illustrates 20 and 19 dB damping on the first and second resonant modes of $G_{\theta_h u}(s)$, respectively. Furthermore,

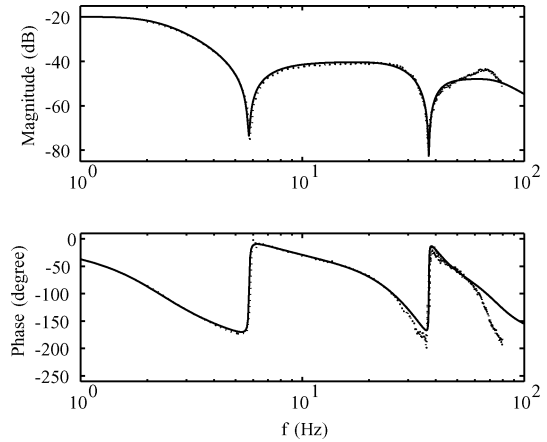


Fig. 11. Simulated (—) and experimental (···) closed-loop frequency responses of amplifier input voltage u to hub angle θ_h using augmented resonant controller $K_a(s)$.

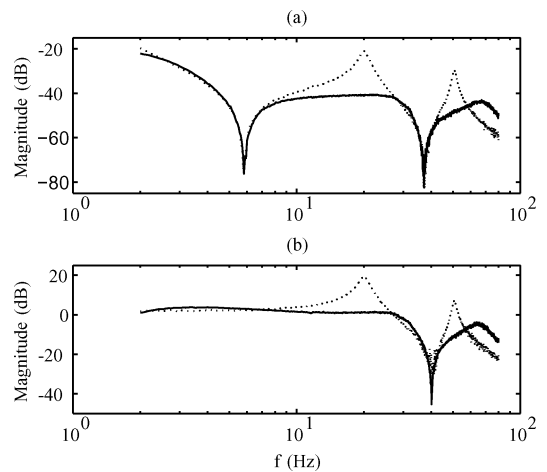


Fig. 12. Open-loop (···) and closed-loop (—). Frequency responses using augmented resonant controller $K_a(s)$. (a) Amplifier input voltage u to hub angle θ_h . (b) Amplifier input voltage u to tip deflection w_{tip} .

Fig. 12(b) shows damping of 18 dB on the first and second resonant modes of $G_{w_{tip}u}(s)$.

Having the flexible manipulator significantly damped by the resonant controller, experiments were performed to slew the tip to a set point $y_{tip} = \pi L/4$ m, with the initial position being set to zero. Initially, the tip was slewed in open-loop to obtain the open loop time response of the tip position and tip deflection. The amount of time taken and the input voltage u needed to be applied to the motor in order to slew the tip to the set point was determined through simulation. Fig. 13 illustrates that the open-loop control resulted in a tip position response with a large steady-state error, long rise and settling times, and a highly oscillating tip.

Similar slewing experiments were performed with an integral controller in the outer feedback loop. Here, the root locus approach was used in selecting the integral controller gain K_I , such that the tip response of the flexible manipulator satisfied the necessary specifications. Fig. 14(a) shows the closed-loop time response of tip position y_{tip} with $K_I = 30$. It is apparent

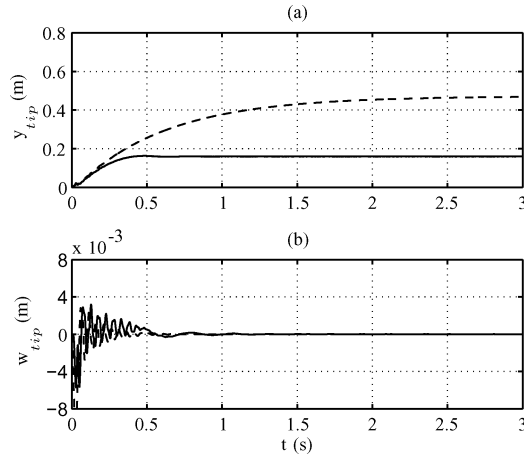


Fig. 13. Experimental (—) and simulated (---). Time response of (a) tip position y_{tip} and (b) tip deflection w_{tip} , in open loop.

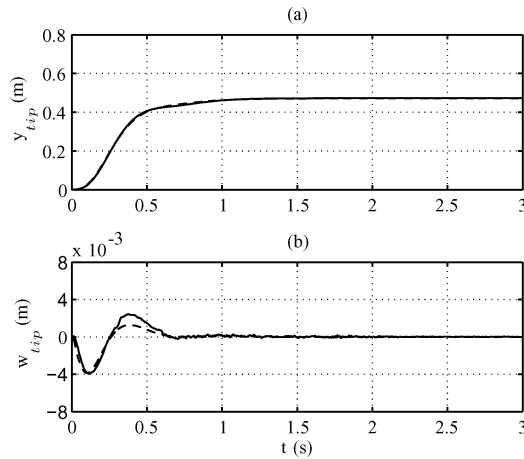


Fig. 14. Experimental (—) and simulation (---). Time response of (a) tip position y_{tip} and (b) tip deflection w_{tip} , using augmented resonant controller $K_a(s)$ and integral controller for $K_I = 30$.

from the plot that y_{tip} has a zero steady-state error, a zero overshoot, a rise time of 0.5 s, and a settling time of 1.0 s. The high gain in K_I has allowed the tip position to have zero steady-state error in 1.3 s. Fig. 14(b) illustrates that the resonant controller completely suppresses the tip vibrations during, and at the end of the slewing maneuver.

A faster response of y_{tip} can be obtained by increasing the K_I , but this comes at the expense of a higher overshoot. Fig. 15(a) shows the response y_{tip} when K_I is increased to 45. The rise and settling times have decreased to 0.2 and 0.6 s, respectively, while the overshoot has increased from 0 to 6.6%. It is worth noting that, even for a faster tip position response, Fig. 15(b) does not show any indication of tip vibrations.

B. Illustration of Robustness

The first robustness test was performed by attaching a certain amount of mass to the tip to alter the dynamics and natural frequencies of the flexible manipulator. This test is performed to study closed-loop performance of the controller with a change

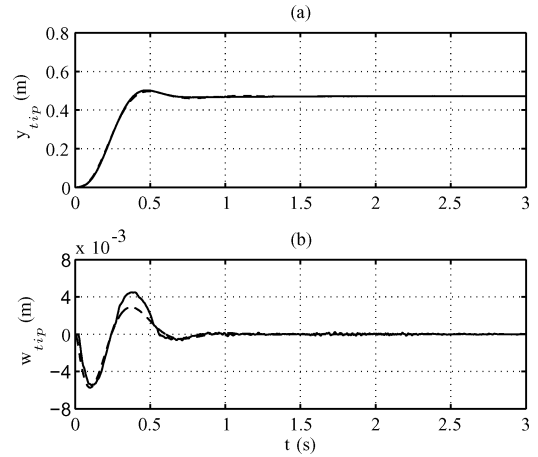


Fig. 15. Experimental (—) and simulation (---). Time response of (a) tip position y_{tip} and (b) tip deflection w_{tip} , using augmented resonant controller $K_a(s)$ and integral controller for $K_I = 45$.

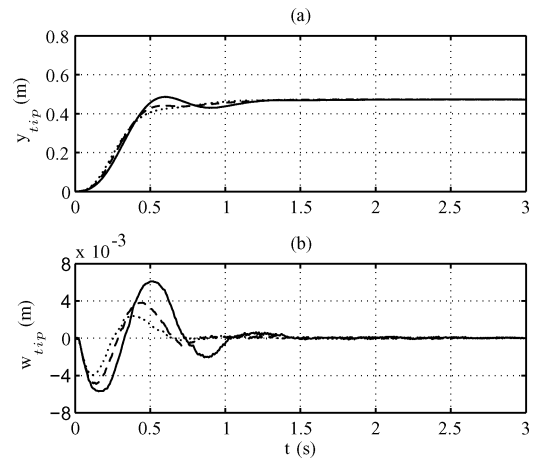


Fig. 16. Time response of (a) tip position y_{tip} and (b) Tip deflection w_{tip} , using augmented resonant controller $K_a(s)$ and integral controller with tip mass = 92 g (—), tip mass = 35 g (---), and no mass (...).

in payload. Two masses are used here; the first has a weight of 35 g (which is 14% of the flexible beam weight) and a second one has a weight of 92 g (which is 35% of the flexible beam weight). With these masses at the tip, no elevation in the tip vibrations was observed, but there was a small overshoot in the y_{tip} response (Fig. 16). However, the overshoot is still within the given specifications.

The second robustness test was performed against the size of input commands. Fig. 17 demonstrates no loss of performance in the y_{tip} and w_{tip} responses when the larger input command of $\pi L/2$ m was used. The y_{tip} response still has similar rise time, settling time, and overshoot regardless of the larger input command.

VI. CONCLUSION

In this paper, frequency-domain system identification was used to model a single-link flexible manipulator. The identified models have accurately predicted the frequency and time responses of the flexible manipulator in open and closed loop.

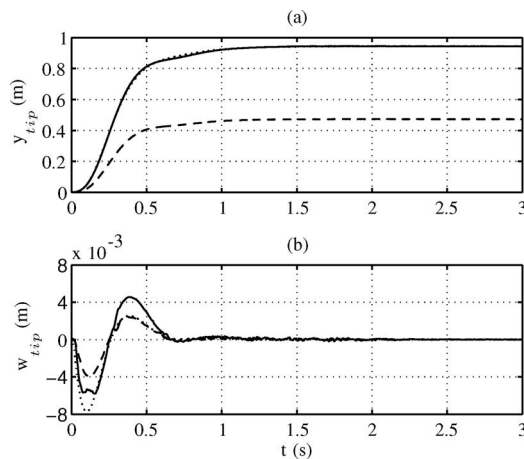


Fig. 17. Time response of (a) tip position y_{tip} and (b) tip deflection w_{tip} , using augmented resonant controller $K_a(s)$ and integral controller for large-step input command, $\pi L/2$ m experimental (—), simulation (\cdots) and for small-step input command $\pi L/4$ (---) m.

The transfer functions characterizing the collocated hub angle $\theta_h(t)$ response to the input $u(t)$ and the noncollocated tip position $y_{tip}(t)$ response to the input $u(t)$ were found to have the same dynamic modes. This allows for the damping of the tip position $y_{tip}(t)$ response, indirectly, by damping the collocated hub angle $\theta_h(t)$ response. A resonant controller was designed to damp the highly resonant modes of the flexible manipulator. The resonant controller performed successfully in damping those modes. The resonant controller was also augmented with a phase-lead compensator to enable it to be used with a high-gain integral controller to achieve precise tip positioning. It was also found that the proposed control scheme was robust to perturbations in the resonance frequencies of the flexible manipulator and the size of the input command.

REFERENCES

- [1] A. R. Fraser and R. W. Daniel, *Perturbation Techniques for Flexible Manipulators*. Norwell, MA: Kluwer, 1991.
- [2] R. H. Cannon and E. Schmitz, "Initial experiments on the end-point control of a flexible one-link robot," *Int. J. Robot. Res.*, vol. 3, no. 3, pp. 62–75, 1984.
- [3] W. T. Qian and C. C. H. Ma, "A new controller design for a flexible one-link manipulator," *IEEE Trans. Autom. Control*, vol. 37, no. 1, pp. 132–137, Jan. 1992.
- [4] V. Feliu, K. S. Rattan, and H. B. Brown, "Control of flexible arms with friction in the joints," *IEEE Trans. Robot. Autom.*, vol. 9, no. 4, pp. 467–475, Aug. 1993.
- [5] J.-H. Park and H. Asada, "Dynamic analysis of noncollocated flexible arms and design of torque transmission mechanisms," *J. Dyn. Syst., Meas., Control*, vol. 116, pp. 201–207, 1994.
- [6] R. N. Banavar and P. Dominic, "An LQG/ H_∞ controller for a flexible manipulator," *IEEE Trans. Control Syst. Technol.*, vol. 3, no. 4, pp. 409–416, Dec. 1995.
- [7] H. Krishnan and M. Vidyasagar, "Control of single-link flexible beam using hankel-norm-based reduced-order model," *Proc. Inst. Elect. Eng. Control Theory Appl.*, vol. 145, no. 2, pp. 151–158, Mar. 1998.
- [8] M.-T. Ho and Y.-W. Tu, "Position control of a single-link flexible manipulator using H_∞ -based PID control," *Proc. Inst. Elect. Eng.—Control Theory Appl.*, vol. 153, no. 5, pp. 615–622, Sep. 2006.
- [9] Z.-H. Luo, "Direct strain feedback control of flexible robot arms: New theoretical and experimental results," *IEEE Trans. Autom. Control*, vol. 38, no. 11, pp. 1610–1622, Nov. 1993.
- [10] S. S. Ge, T. H. Lee, and G. Zhu, "Improving regulation of a single-link flexible manipulator with strain feedback," *IEEE Trans. Robot. Autom.*, vol. 14, no. 14, pp. 179–185, Feb. 1998.
- [11] H. R. Pota, S. O. R. Moheimani, and M. Smith, "Resonant controllers for smart structures," *Smart Mater. Struct.*, vol. 11, no. 1, pp. 1–8, 2002.
- [12] S. O. R. Moheimani and B. J. G. Vautier, "Resonant control of structural vibration using charge-driven piezoelectric actuators," *IEEE Trans. Control Syst. Technol.*, vol. 13, no. 6, pp. 1021–1035, Nov. 2005.
- [13] M. J. Balas, "Feedback control of flexible structures," *IEEE Trans. Autom. Control*, vol. 23, no. 4, pp. 673–679, Aug. 1978.
- [14] D. Halim and S. O. R. Moheimani, "Spatial resonant control of flexible structures—Application to a piezoelectric laminate beam," *IEEE Trans. Control Syst. Technol.*, vol. 9, no. 1, pp. 37–53, Jan. 2001.
- [15] N. W. Hagood, W. H. Chung, and A. v. Flotow, "Modelling of piezoelectric actuator dynamics for active structural control," *J. Intell. Mater. Syst. Struct.*, vol. 21, no. 3, pp. 327–354, 1990.
- [16] K. W. Wang *Structural Vibration Suppression Via Parametric Control Actions—Piezoelectric Materials With Real-Time Semi-Active Networks*, A. Guran and D. J. Inman, Eds., Singapore: World Scientific, 1995.
- [17] S. O. R. Moheimani, A. J. Fleming, and S. Behrens, "On the feedback structure of wideband piezoelectric shunt damping systems," *Smart Mater. Struct.*, vol. 12, pp. 49–56, Feb. 2003.
- [18] R. C. Dorf and R. H. Bishop, *Modern Control Systems*. Reading, MA: Addison-Wesley, 1998.



Iskandar A. Mahmood was born in Malaysia in 1975. He received the B. Eng. and M.Sc. degrees in mechatronics engineering from the International Islamic University Malaysia, Kuala Lumpur, Malaysia, in 1999 and 2004, respectively. He is currently working toward the Ph.D. degree in electrical engineering at the University of Newcastle, Callaghan, Australia.

Since 2005, he has been with the Laboratory of Dynamics and Control of Nanosystems, University of Newcastle.



S. O. Reza Moheimani (SM'01) received the Ph.D. degree in electrical engineering from the University of New South Wales at Australian Defence Force Academy, Canberra, Australia, in 1996.

Since 1997, he has been with the University of Newcastle, Callaghan, Australia, where he is a Professor with the School of Electrical Engineering and Computer Science. He also serves as the Assistant Dean (Research) for the Faculty of Engineering, and an Associate Director of the Centre for Complex Dynamic Systems and Control, an Australian Government Centre of Excellence. He has published two books, several edited volumes, and over 150 refereed articles. His current interests include applications of control and estimation in nanoscale positioning systems for scanning probe microscopy, control of electrostatic micro-actuators in MEMS, and data storage systems.

Prof. Moheimani is a recipient of the 2007 IEEE TRANSACTIONS ON CONTROL SYSTEMS TECHNOLOGY Outstanding Paper Award, and a Fellow of the Institute of Physics, U.K. He is an Associate Editor of several international journals, and has chaired a number of international workshops and conferences.



Bharath Bhikkaji received the Ph.D. degree in signal processing from Uppsala University, Uppsala, Sweden, in 2004.

He is currently a Research Academic in the School of Electrical Engineering and Computer Science, University of Newcastle, Callaghan, Australia. His current research interests include system identification, robust control, and active noise and vibration control of flexible structures.

Precise Tip Positioning of a Flexible Manipulator using Resonant Control

I. A. Mahmood, S. O. R. Moheimani and B. Bhikkaji

Abstract—A single-link flexible manipulator is fabricated to represent a typical flexible robotic arm. This flexible manipulator is modeled as a SIMO system with the motor-torque as the input and the hub angle and the tip position as the outputs. The two transfer functions are identified using a frequency-domain system identification method. A feedback loop around the hub angle response with a Resonant controller is designed to damp the resonant modes. A high gain integral controller is also designed to achieve zero steady-state error in the tip position response. Experiments are performed to demonstrate the effectiveness of the proposed control scheme.

I. INTRODUCTION

Increasing demands for high speed manipulation and high payload to weight ratio in robot manipulators has triggered a significant growth in research and development activities on flexible manipulators. These manipulators constitute a suitable choice to realize such demands since they are light in weight, require small sized actuators and consume low energy for actuation [1]. However, designing feedback controllers to operate these systems at high speeds is a challenging task. The control system must be designed not only for precise tip positioning but also for suppressing vibrations associated with the flexible nature of the manipulator.

A wide range of control schemes such as linear quadratic gaussian (LQG) [2], linear quadratic regulator (LQR) [3], H_∞ control [4] and μ -synthesis [5] have been used for the positioning of flexible manipulators. In [2], Cannon and Schmitz designed an LQG controller and used measurements from a noncollocated tip position sensor as the controller input. Their results suggested a satisfactory step response with accurate tip positioning. However, the LQG controller was not robust with respect to modeling errors and was of a very high order. In [6], the authors improved the closed-loop system robustness of [2] by wrapping a second feedback loop, consisting of an H_∞ controller around the controlled system. The H_∞ controller was designed for the purpose of incorporating robustness and also for attenuating disturbances. Simulation results suggested that the control scheme was more robust to uncertainties such as modeling errors. The lack of robustness demonstrated in [2], and [6] is believed to be due to the use of noncollocated sensors which result in non-minimum phase systems [7]. Nevertheless, the noncollocated sensors are often used as they are needed for precise tip positioning.

The authors are with the School of Electrical Engineering and Computer Science, The University of Newcastle, Callaghan, NSW 2308, Australia. R. Moheimani is the corresponding author. Reza.Moheimani@newcastle.edu.au

In contrast to the research reported in the above references, vibration control was given precedence over tip positioning in [8] and [9]. In [8] the author proposed a direct strain feedback (DSFB) control strategy to introduce a damping term into the differential equation governing the vibration of the flexible manipulator. This control strategy managed to increase the stiffness of the flexible manipulator and caused it to undergo smaller vibration levels while in motion. In [9], a sliding mode controller was formulated to control the tip position of a flexible manipulator subjected to parameter variations. The authors showed via simulations that the controller performed better in regulating vibrations when initial conditions were incorporated into the designed controller.

In this work, an experimental flexible manipulator setup is fabricated to represent a typical flexible robotic arm. A control scheme is developed such that the vibration suppression is achieved using a collocated measurement and tip positioning is done using a noncollocated measurement. The control scheme consists of two feedback loops with each feedback loop having a specific purpose. The inner loop contains a Resonant controller to add damping to the flexible manipulator. The Resonant controller utilizes the hub angle measurement provided by a shaft encoder and guarantees that the closed-loop system remains stable in the presence of out-of-bandwidth dynamics, [10] and [11]. In the outer loop, using tip position measurements, an integral controller is implemented for precise tip positioning. The integral controller ensures zero steady-state error for a step input.

Successful utilizations of Resonant controllers for vibration suppression in flexible structures have been reported in [10], [11] and [12]. This paper reports the first-time application of this control design approach to flexible manipulators. At the time of this writing it is not known how an optimal Resonant controller can be designed. This is mainly due to the non-convex nature of the optimization problem associated with minimization of a specific performance index. In this paper a graphical approach is proposed, which results in Resonant controllers with satisfactory performance.

The remainder of the paper is arranged as follows. Section II provides a description of the experimental setup. System identification of the system transfer-functions are presented in Section III. Control schemes are devised in Section IV. In Section V, simulation and experimental results are presented to illustrate the effectiveness of the proposed control schemes. Finally, the paper is concluded in Section VI.

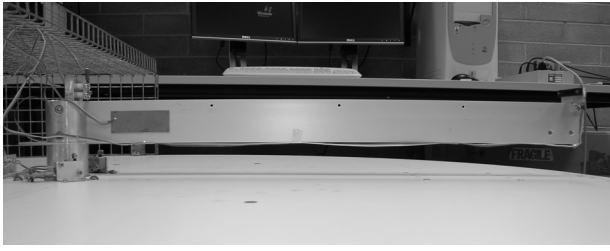


Fig. 1. Flexible manipulator

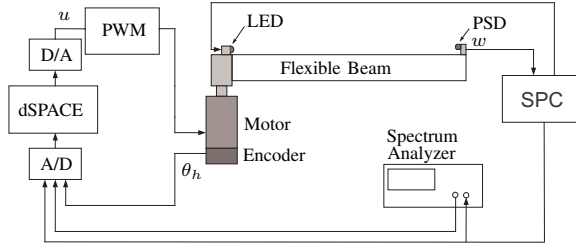


Fig. 2. Experimental setup for the flexible manipulator

TABLE I

MECHANICAL PROPERTIES OF THE FLEXIBLE MANIPULATOR

Properties	Values
Length, L	0.6 m
Thickness, h	0.003 m
Width, v	0.05 m
Linear density, ρ	0.3975 kg/m
Radius of hub, r	0.025 m
Modulus of elasticity, E	6.894×10^{10} Pa
Hub moment of inertia (including motor), I_h	1.850×10^{-3} Kg.m ²

II. EXPERIMENTAL SETUP

The experiments were performed in the Laboratory for Dynamics and Control of NanoSystems at The University of Newcastle, Australia. The flexible manipulator used here consists of an aluminum beam clamped directly to the shaft of a Glentek GM4040-41 DC brush servo motor. A detailed illustration of the experimental setup is presented in Fig. 1 and 2. The dimensions and the mechanical properties of the beam are given in Table I. The motor was driven by a Glentek GA377 pulse width modulation (PWM) servomotor amplifier. The shaft encoder of the motor was used to measure the hub angle of rotation. The shaft encoder has a count of 5000 per revolution, i.e. a resolution of 0.072 degrees.

An infrared light-emitting diode (LED) and a Hamamatsu S1352 position sensitive detector (PSD) were used for measuring the deflection of the tip of the beam. A dSPACE DS1103 controller board was used for real-time controller implementation. A sampling frequency of 20 kHz was used in order to avoid aliasing.

III. SYSTEM IDENTIFICATION

In this work, an experimental approach is taken to model the dynamics of the flexible manipulator. The following

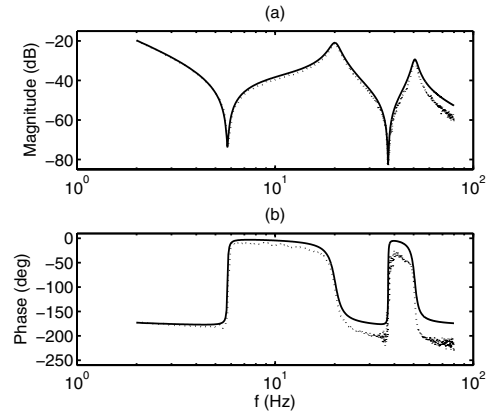


Fig. 3. Identified model (—) and experimental (···) frequency response of amplifier input voltage u to hub angle θ_h .

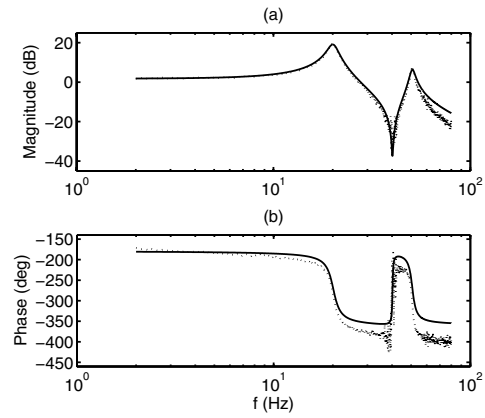


Fig. 4. Identified model (—) and experimental (···) frequency response of amplifier input voltage u to tip deflection w_{tip} .

frequency response functions (FRFs) are determined for designing the control system:

$$G_{\theta_h u}(i\omega) \triangleq \frac{\theta_h(i\omega)}{u(i\omega)}, \quad (1)$$

$$G_{w_{tip} u}(i\omega) \triangleq \frac{w_{tip}(i\omega)}{u(i\omega)} \quad (2)$$

and

$$G_{y_{tip} u}(i\omega) = G_{w_{tip} u}(i\omega) + LG_{\theta_h u}(i\omega) \quad (3)$$

where $u(t)$ is the input voltage, $\theta_h(t)$ is the hub angle measured by the shaft encoder, $w_{tip}(t) = w(L, t)$ is the flexural tip deflection measured by the PSD. It is worth noting that the tip position $y_{tip}(t) \triangleq y(L, t) = w(L, t) + L\theta_h(t)$, which leads to the expression (3) for the FRF $G_{y_{tip} u}(i\omega)$.

A dual channel HP35670A spectrum analyzer was used for determining the FRFs. A band limited random noise signal (2 to 102 Hz) was generated using the spectrum analyzer and applied to the motor as the input, $u(t)$. The corresponding outputs $\theta_h(t)$ and $w_{tip}(t)$ were also recorded using the spectrum analyzer. The input-output data was processed to generate the FRFs (1) and (2) in a non-parametric form. In Fig. 3 and 4 the nonparametric FRFs of (1) and (2) are plotted

along with corresponding parametric fits,

$$G_{\theta_{hu}}(s) = \frac{420.73(s^2 + 0.5028s + 1305)}{s(s + 1.65)(s^2 + 15.35s + 1.596 \times 10^4)} \times \frac{(s^2 + 1.437s + 5.462 \times 10^4)}{(s^2 + 20.9s + 1.015 \times 10^5)} \quad (4)$$

and

$$G_{w_{tipu}}(s) = \frac{-31153.01}{(s^2 + 15.35s + 1.596 \times 10^4)} \times \frac{(s^2 + 3.108s + 6.386 \times 10^4)}{(s^2 + 20.9s + 1.015 \times 10^5)}. \quad (5)$$

Note that the poles characterizing the flexible modes of the beam in $G_{\theta_{hu}}(s)$ and $G_{w_{tipu}}(s)$ are identical. Data beyond 80 Hz were discarded as these frequencies were far beyond the maximum bandwidth of the motor (which is close to 60 Hz). Fig. 3, clearly illustrates the collocated nature of $G_{\theta_{hu}}(s)$.

IV. CONTROLLER DESIGN

This section discusses and details the control design scheme proposed in this paper. The control scheme consists of two negative feedback loops.

A. Resonant controller design (Inner loop controller)

Feedback controllers which increase the effective damping and at the same time guarantee unconditional stability of the closed-loop system are always preferred, as they avoid closed-loop instabilities due to spill-over effects [13]. It is known that a collocated velocity feedback controller [13] possess such properties. However, the implementation of this controller requires the realization of a differentiator, which is not possible for systems with large bandwidth. Another drawback of the velocity feedback controller is that it results in a high control effort at all frequencies. Ideally, for vibration damping purposes, the control effort should be restricted to the resonance frequencies only. Resonant controllers are a class of controllers that guarantee unconditional closed-loop stability of collocated systems. The model structure of Resonant controllers are such that they approximate a differentiator over a narrow bandwidth around the resonance frequencies. Resonant controllers were first proposed in [10]. The motivations for their model structure comes from passive RL network controllers for piezoelectric shunt damping, see [14], [15] and [16].

As the poles characterizing the flexible modes of $G_{\theta_{hu}}(s)$ and $G_{y_{tipu}}(s)$ are identical, system resonances can be damped by designing a feedback loop around either $G_{\theta_{hu}}(s)$ or $G_{y_{tipu}}(s)$. Here, $G_{\theta_{hu}}(s)$ is chosen due to its collocated nature. Damping can be achieved by shifting the closed-loop poles of $G_{\theta_{hu}}(s)$ deeper into the left half plane.

In general, a resonant controller is defined as

$$K(s) = \sum_{i=1}^N \frac{\alpha_i s^2}{s^2 + 2\delta_i \omega_i s + \omega_i^2} \quad (6)$$

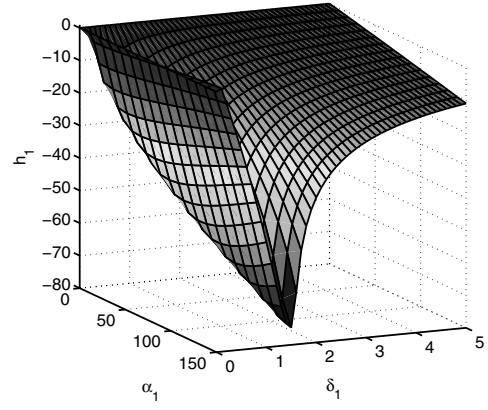


Fig. 5. Plot of distance between the real parts of the open-loop and close-loop poles h_1 versus α_1 and δ_1 , for the 1st flexible mode.

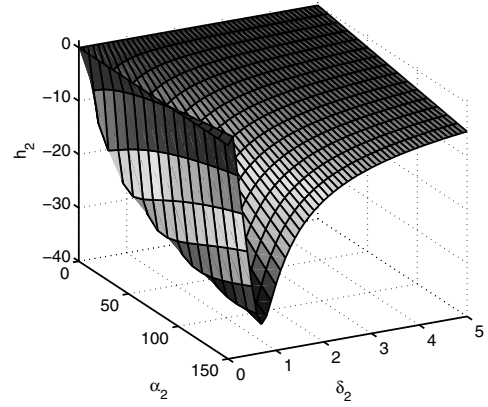


Fig. 6. Plot of distance between the real parts of the open-loop and close-loop poles h_2 versus α_2 and δ_2 , for the 2nd flexible mode.

where α_i , δ_i and ω_i are the design parameters, and N is the number of modes that need to be controlled. In the current context $N = 2$, which implies

$$K(s) = K_1(s) + K_2(s), \quad (7)$$

where

$$K_1(s) = \frac{\alpha_1 s^2}{s^2 + 2\delta_1 \omega_1 s + \omega_1^2} \quad (8)$$

and

$$K_2(s) = \frac{\alpha_2 s^2}{s^2 + 2\delta_2 \omega_2 s + \omega_2^2}. \quad (9)$$

Here, the resonant filters $K_1(s)$ and $K_2(s)$ are determined independently. Each ω_i is set to the i^{th} natural frequency of the flexible manipulator and the value of α_i and δ_i are varied such that the absolute distance between the real parts of the open-loop and closed-loop poles, h_i , is maximized. Fig. 5 and 6 show that for a given range of α_i ($0 \leq \alpha_i \leq 150$), there exists a value of δ_i which maximizes the absolute value of h_i . The controller obtained for this range of α is

$$K(s) = \frac{150s^2}{s^2 + 378.3s + 1.59 \times 10^4} + \frac{150s^2}{s^2 + 445.8s + 1.014 \times 10^5}. \quad (10)$$

Better damping can be achieved by increasing the range of α . However, this would result in a controller that has a higher gain. The high magnitude could amplify high-frequency noise which could lead to degradation of the closed-loop performance. Here, it is possible to determine the resonant filters independently because there is sufficient frequency spacing between the system poles and zeros and the action of the resonant filters is mostly uncoupled [10].

It is worth noting that in closed-loop, the Resonant controller $K(s)$ will not shift the pole located at the origin. This can be seen by setting

$$G_{\theta_{hu}}(s) = \frac{a(s)}{s \times b(s)} \quad (11)$$

and

$$K(s) = \frac{s^2 \times p(s)}{q(s)} \quad (12)$$

and noting that

$$\begin{aligned} G_{\theta_{hu}}^{(cl)}(s) &= \frac{G_{\theta_{hu}}(s)}{1 + K(s)G(s)} \\ &= \frac{1}{s} \left(\frac{a(s)}{q(s)b(s) + sp(s)a(s)} \right). \end{aligned} \quad (13)$$

B. Outer loop for positioning

Integral controller was implemented in the outer feedback loop to provide precise tip positioning. In designing the integral controllers, the gross response of the flexible manipulator to a step input needs to satisfy the following specifications: 1) Zero steady-state tip position error, 2) Rise time and settling time of less than 1 and 1.5 s, respectively and 3) Overshoot of less than 2 %.

An important property of an integral controller is that a positive error will always result in increasing the control signal while a negative error will result in a decreasing control signal, regardless of the magnitude of the error, [17]. This property is desirable because the error introduced by the motor friction, which becomes visible when the tip is nearing the given set-point or moving at a very slow speed, can be eliminated.

In order to wrap an integral controller around $G_{y_{tip}u}(s)$ such that the resulting closed-loop has an acceptable stability margin, $G_{\theta_{hu}}^{(cl)}(s)$ must not have a pole at the origin. This can be checked using the standard root-locus criterion. A simple way to correct this problem would be to add or augment the Resonant controller with a rational function $C(s)$. In other words the pure Resonant controller in the inner feedback loop is replaced by

$$K_a(s) = K(s) + C(s), \quad (14)$$

see also the illustration in Fig. 7. In order to avoid a large increase in the model order of the controller and at the same time push the pole at $s = 0$ well into the left half plane, a phase-lead compensator is used,

$$C(s) = \frac{K_{pl}(s + \alpha)}{s + \beta} \quad (15)$$

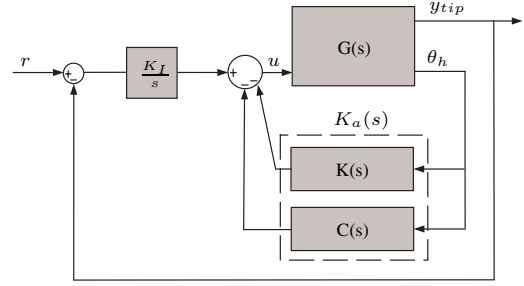


Fig. 7. Augmented Resonant controller $K_a(s)$ and integral controller $\frac{K_I}{s}$.

where K_{pl} , α and β are the design parameters. The parameters can be chosen using root-locus approach. The use of phase-lead compensator and guidelines on pole placement using them are given in detail in [18].

Here we set

$$C(s) = \frac{70(s + 10)}{s + 70}, \quad (16)$$

which implies that the augmented Resonant controller is equal to

$$\begin{aligned} K_a(s) &= \frac{70(s + 10)}{s + 70} + \frac{150s^2}{s^2 + 378.3s + 1.59 \times 10^4} \\ &\quad + \frac{150s^2}{s^2 + 445.8s + 1.014 \times 10^4}. \end{aligned} \quad (17)$$

V. SIMULATION AND EXPERIMENTAL RESULTS

This section presents simulation and experimental results obtained from the control schemes proposed in this paper.

A. Resonant and Integral controller

The effect of damping introduced by the augmented Resonant controller $K_a(s)$ on the resonant modes were first evaluated. In Fig. 8 the simulated closed-loop frequency response of $G_{\theta_{hu}}(s)$ is plotted along with its experimental counterpart. It is evident that the experimental results match the simulations except near the second resonant mode. This is due to the fact that the second resonance is very close to the maximum bandwidth of the motor.

In Fig. 9, experimentally determined closed-loop frequency responses of $G_{\theta_{hu}}(s)$ and $G_{w_{tip}u}(s)$ are plotted along with their corresponding open-loop frequency responses. A significant damping in the first and the second resonances of both $G_{\theta_{hu}}(s)$ and $G_{w_{tip}u}(s)$ is evident from the plots. In particular, Fig. 9 (a) illustrates 20 dB and 19 dB damping on the 1st and 2nd modes of $G_{\theta_{hu}}(s)$ respectively. Furthermore, Fig. 9 (b) shows damping of 18 dB on the 1st and 2nd mode of $G_{w_{tip}u}(s)$, respectively.

Having the flexible manipulator significantly damped by the augmented Resonant controller, experiments were performed to slew the tip to a set-point $y_{tip} = \frac{\pi L}{4}$ m, with the present position being set to zero. For the sake of comparison, initially, the tip was slewed in open-loop to obtain the open-loop time response of the tip position and tip deflection. The amount of time the input voltage u needed

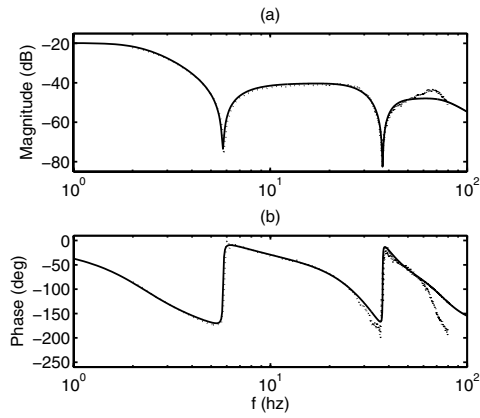


Fig. 8. Simulated (—) and experimental (···) closed-loop frequency responses of amplifier input voltage u to hub angle θ_h using augmented Resonant controller $K_a(s)$.

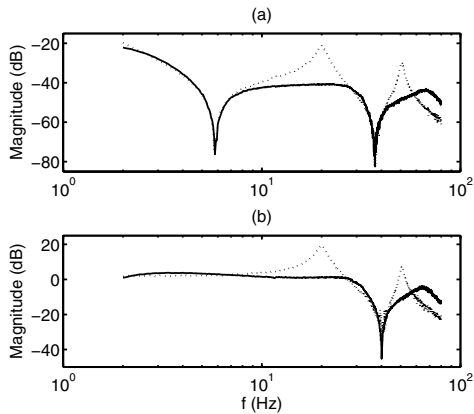


Fig. 9. Open-loop (···) and closed-loop (—): Frequency responses of (a) amplifier input voltage u to hub angle θ_h , (b) amplifier input voltage u to tip deflection w_{tip} using augmented Resonant controller $K_a(s)$.

to be applied to the motor in order to slew the tip to the set-point was determined through simulation. Fig. 10 illustrates that the open-loop control resulted in a tip position response with a large steady-state error, slow rise and settling times, and a highly oscillating tip.

Similar slewing experiments were performed with an integral controller in the outer feedback loop. Here, root-locus approach was used in selecting the integral controller gain K_I . Fig. 11 (a) shows the closed-loop time response of tip position y_{tip} with $K_I = 30$. It is apparent from the plot, that y_{tip} has a zero steady-state error, a zero overshoot, a rise time of 0.5 s and a settling time of 1.0 s. The high gain in K_I has allowed the tip position to have zero steady-state error in 1.3 s. Fig. 11 (b) illustrates that the Resonant controller completely suppresses the tip vibrations during, and at the end of the slewing maneuver.

A faster response of y_{tip} can be obtained by increasing the value of K_I , but this comes at the expense of a higher overshoot. Fig. 12 (a) shows the response y_{tip} when K_I is increased to 45. It can be observed that the rise and settling times have decreased to 0.2 s and 0.6 s respectively, while the overshoot has increased from 0 to 6.6 %. It is worth noting

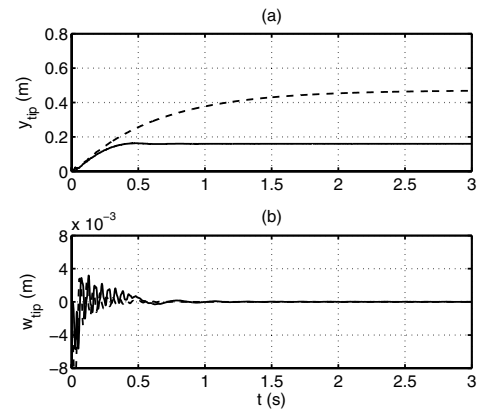


Fig. 10. Experimental (—) and simulated (---): Time response plots of (a) Tip position y_{tip} , (b) Tip deflection w_{tip} , in open-loop.

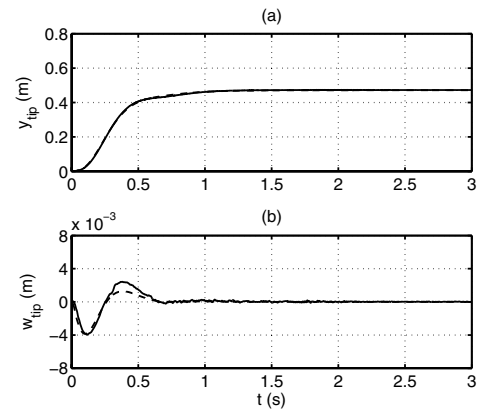


Fig. 11. Experimental (—) and simulation (---): Time response plots of (a) Tip position y_{tip} , (b) Tip deflection w_{tip} , using augmented Resonant controller $K_a(s)$ and integral controller for $K_I = 30$.

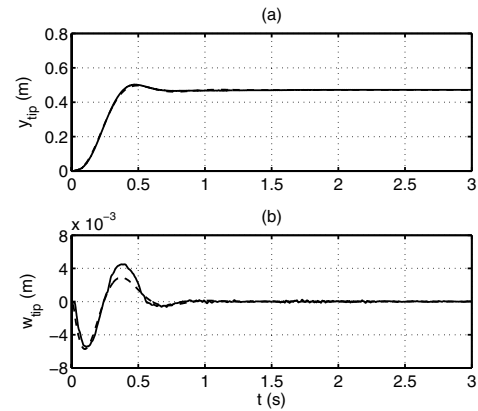


Fig. 12. Experimental (—) and simulation (---): Time response plots of (a) Tip position y_{tip} , (b) Tip deflection w_{tip} , using augmented Resonant controller $K_a(s)$ and integral controller for $K_I = 45$.

that, even for a faster tip position response, Fig. 12 (b) does not show any indication of tip vibrations.

B. Robustness analysis

The robustness of the proposed controller scheme is analyzed here. The first robustness test was performed by

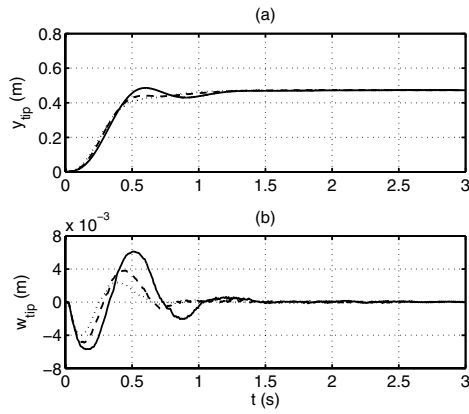


Fig. 13. Time response plots of (a) Tip position y_{tip} , (b) Tip deflection w_{tip} , using augmented Resonant controller $K_a(s)$ and integral controller with tip mass = 92 g (—), tip mass = 35 g (---) and no mass (...).

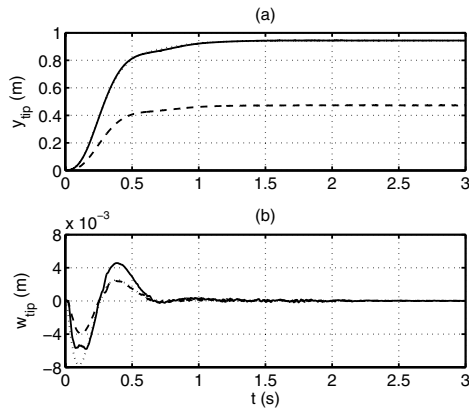


Fig. 14. Time response plots of (a) Tip position y_{tip} , (b) Tip deflection w_{tip} , using augmented Resonant controller $K_a(s)$ and integral controller for large step input command, $\frac{\pi L}{2}$ m. Experimental (—), simulation (...) and small step input command $\frac{\pi L}{4}$ m (---).

attaching a certain amount of mass to the tip to alter the dynamics and natural frequencies of the flexible manipulator. This test is performed to study closed-loop performance of the controller with a change in payload. Two masses are used here, the first has a weight of 35 g (which is 14 % of the flexible beam weight) and a second set has a weight of 92 g (which is 35 % of the flexible beam weight). With these masses at the tip, Fig. 13 shows no elevation in the tip vibrations, but a small overshoot in the y_{tip} response.

The second robustness test was performed against the size of input commands. Fig. 14 shows no loss of performance in the y_{tip} and w_{tip} responses when a larger input command of $\frac{\pi L}{2}$ m was used. The y_{tip} response still has similar rise time, settling time and overshoot regardless of the size of input commands.

VI. CONCLUSIONS

In this paper frequency-domain system identification was used to model a single link flexible manipulator. The identi-

fied models have accurately predicted the frequency and time responses of the flexible manipulator. The transfer-functions characterizing the collocated hub angle $\theta_h(t)$ response to the input $u(t)$ and the noncollocated tip position $y_{tip}(t)$ response to the input $u(t)$ were found to have the same dynamic modes. This allows for the damping of the tip position $y_{tip}(t)$ response, indirectly, by damping the collocated hub angle $\theta_h(t)$ response. A Resonant controller was designed to damp the highly resonant modes of the flexible manipulator. The Resonant controller performed successfully in damping those modes. It was also found that the proposed control scheme was robust to perturbations in the resonance frequencies of the flexible manipulator and the size of input command.

REFERENCES

- [1] A. R. Fraser and R. W. Daniel, *Perturbation techniques for flexible manipulators*. Kluwer Academic Publisher, 1991.
- [2] R. H. Cannon and E. Schmitz, "Initial experiments on the end-point control of a flexible one-link robot," *The International Journal of Robotics Research*, vol. 3, no. 3, pp. 62–75, Fall 1984.
- [3] V. Etxebarria, A. Sanz and I. Lizarraga, "Real-time experimental control of a flexible robotic manipulator using a composite approach," in *Proceeding of the 2004 IEEE International Conference on Control Applications*, September 2004, pp. 955–960.
- [4] D. Farruggio and L. Menini, "Two degrees of freedom H_∞ control of a flexible link," in *Proceedings of the American Control Conference*, June 2000, pp. 2280–2284.
- [5] M. Karkoub and K. Tamma, "Modelling and μ -synthesis control of flexible manipulators," *Computers and Structures*, vol. 79, pp. 543–551, 2001.
- [6] R. N. Banavar and P. Dominic, "An LQG/ H_∞ controller for a flexible manipulator," *IEEE Transactions on Control Systems Technology*, vol. 3, no. 4, pp. 409–416, December 1995.
- [7] V. A. Spector and H. Flashner, "Modeling and design implications of noncollocated control in flexible systems," *Transactions of the ASME Journal of Dynamic Systems, Measurement, and Control*, vol. 112, pp. 186–193, June 1990.
- [8] Z.-H. Luo, "Direct strain feedback control of flexible robot arms: new theoretical and experimental results," *IEEE Transaction on Automatic Control*, vol. 38, no. 11, pp. 1610–1622, November 1993.
- [9] S. -B. Choi, C. -C. Cheong and H. -C. Shin, "Sliding mode control of vibration in a single-link flexible arm with parameter variations," *Journal of Sound and Vibration*, vol. 179, no. 5, pp. 737–748, 1995.
- [10] H. R. Pota, S. O. R. Moheimani and M. Smith, "Resonant controllers for smart structures," *Smart Materials and Structures*, vol. 11, pp. 1–8, 2002.
- [11] S.O. R. Moheimani and B. J. G. Vautier, "Resonant control of structural vibration using charge-driven piezoelectric actuators," *IEEE Transaction on Control System Technology*, vol. 13, pp. 1021–1035, 2005.
- [12] D. Halim and S. O. R. Moheimani, "Spatial resonant control of flexible structures – application to a piezoelectric laminate beam," *IEEE Transactions on Control System Technology*, vol. 9, pp. 37–53, 2001.
- [13] M. J. Balas, "Feedback control of flexible structures," *IEEE Transactions on Automatic Control*, vol. AC-23, no. 4, 1978.
- [14] N. W. Hagood, W. H. Chung and A. v. Flotow, "Modelling of piezoelectric actuator dynamics for active structural control," *Journal of Intelligent Material Systems and Structures*, vol. 21, 1990.
- [15] K. W. Wang, *Structural vibration suppression via parametric control actions – piezoelectric materials with real-time semi-active networks*, A. Guran and D. J. Inman, Eds. Singapore: World Scientific, 1995.
- [16] S. O. R. Moheimani, A. J. Fleming, and S. Behrens, "On the feedback structure of wideband piezoelectric shunt damping systems," *Smart Materials and Structures*, vol. 12, pp. 49–56, February 2003.
- [17] K. Astrom and T. Hagglund, *PID Controllers: Theory, Design, and Tuning*. Instrument Society of America, 1995.
- [18] R. C. Dorf and R. H. Bishop, *Modern Control Systems*. Addison Wesley Longman, Inc., 1998.

Vibration and Position Control of a Flexible Manipulator

I. A. Mahmood¹, B. Bhikkaji² and S. O. R. Moheimani^{3#}

^{1,2,3} School of Electrical Engineering and Computer Science, The University of Newcastle
Callaghan, NSW, Australia, Reza.Moheimani@newcastle.edu.au

Abstract

A single-link flexible manipulator is fabricated. This flexible manipulator is modeled as a SIMO system with the motor-torque as the input and the hub angle and the tip position as the outputs. The two transfer functions are identified using frequency-domain system identification. A polynomial based feedback controller is designed to damp hub angle response. This controller also damps the tip position response. Apart from damping the system, the feedback controller also provides substantial robustness. Finally, an integral controller is also designed to achieve zero-steady state error in the tip position.

1. INTRODUCTION

Over the past two decades the need for high speed manipulation and high payload to weight ratio in robot manipulators has triggered a significant growth in the research and development of the flexible manipulators [1]. Flexible manipulators are a suitable choice to realize such needs since they are light in weight, require small sized actuators and consume low energy for actuation [2]. However, the use of these flexible manipulators at a high speed poses challenging problems in designing their control system. The control system must be designed not only for precise tip positioning but also for suppressing the vibrations arising due to the flexible nature of the manipulator. Thus, for developing such a control system, advanced control techniques are generally required.

In an early work, [3], Cannon and Schmitz employed a control scheme where a Linear Quadratic Gaussian (LQG) controller was designed with measurements from the noncollocated tip position sensor used as the controller input. Their results suggested a satisfactory step response and accurate tip positioning. However, the LQG controller designed was not robust to modeling errors and was of very high order. In [4] an LQG controller was designed based on a reduced-order model obtained using Hankel-norm minimization. The closed-loop performance obtained using this controller closely matched the one obtained from an LQG designed based on the full-order model. Nevertheless this does not guarantee robustness. The noncollocated control approach introduced in [3] and [4] was further studied in [5] with an aim to improve the closed-loop system's robustness. In [5], the authors presented a control scheme with two

feedback loops. The controller in the inner loop was an LQG design and the controller in outer loop was an H_∞ design. The H_∞ controller was designed for the purpose of incorporating robustness and also for attenuating the disturbances. Experimental results in [5] suggested that the control scheme was more robust to uncertainties. The use of noncollocated measurements have resulted in non-minimum phase systems whose close-loop stability can be sensitive to errors in the model parameters [6]. Nevertheless the noncollocated measurements are used because they give precise tip position control [3], [4], [5].

Collocated sensors such as a shaft encoder or a strain gauge placed at the root end of the flexible manipulator have also been used in the control of flexible manipulators [7], [8]. The main advantage of using collocated sensors is that their measurements result in a passive transfer function, and hence requires simpler controllers to stabilize the system [9]. In [8], measurements from the shaft encoder and a strain gauge, placed at the root end of the flexible manipulator, were used to measure the hub angle and strain, respectively. The measurements from the shaft encoder were used for positioning the flexible manipulator, while the strain gauge measurements were used for damping the vibrations. A control strategy based on these measurements increased the stiffness of the flexible manipulator and caused the flexible manipulator to undergo smaller vibration levels while in motion.

In this work an experimental flexible manipulator setup was fabricated to represent a typical flexible manipulator. A control strategy using both collocated and noncollocated measurements was developed for vibration suppression as well as for the position control of the flexible manipulator. A shaft encoder and a position sensitive detector (PSD) were used for obtaining collocated and noncollocated measurements respectively. The use of each measurement would provide a specific benefit. The control strategy consists of two feedback loops. In the first loop, a polynomial-based pole placement controller, was designed to add damping to the flexible manipulator. And in the second loop, an integral controller was designed for precise tip positioning. The input to the polynomial-based controller is the collocated hub angle measurement, and the input to the integral controller is the tip position (hub angle

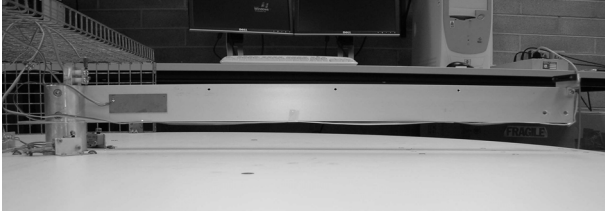


Fig. 1: Flexible manipulator

plus the noncollocated tip deflection measurement).

The remainder of the paper is arranged as follows. Section 2 provides a description of the experimental setup. Modelling and identification of the system transfer-functions are presented in Section 3. Control strategies are devised in Section 4. In Section 5, simulation and experimental results are presented to illustrate the effectiveness of the control strategies. Finally, the paper is concluded in Section 6.

2. EXPERIMENTAL SETUP

The flexible manipulator used here consists of an aluminum beam clamped directly to the shaft of a Glentek GM4040-41 DC brush servo motor, see Figures 1 and 2 for illustrations of the experimental setup. The dimensions and the mechanical properties of the beam are given in Table 1. The motor is driven by a Glentek GA377 pulse width modulation (PWM) servomotor amplifier. The motor has a continuous stall torque of 3.54 Nm and a maximum bandwidth of 58 Hz. The tachogenerator and the shaft encoder of the motor are used to measure the hub angular speed and hub angle of rotation, respectively. The shaft encoder has a count of 5000 per revolution or alternatively it has a resolution of 0.072 degrees.

An infrared light-emitting diode (LED) and a Hamamatsu S1352 position sensitive detector (PSD) are used for measuring the deflection of tip of the beam. The infrared LED is fixed on top of the hub and the PSD is fixed at the tip. The infrared LED emits a signal with a typical wavelength of 880 nm and a typical output power of 2 mW. The PSD is comprised of two electrodes that generate photocurrents depending on position of the infrared spot light on the sensor. A Hamamatsu C5923 signal processing circuit (SPC) is used to drive the infrared LED and also to convert the photocurrents into a voltage signal the magnitude of which is proportional to the spot light position.

A dSPACE DS1103 PPC controller board is used for real-time control implementation. A sampling frequency of 20 kHz is used in order to avoid aliasing. Simulink is used to download the controller into the controller board.

3. MODELING AND SYSTEM IDENTIFICATION

Analytical characterizations of the dynamics of flexible manipulators have been investigated by many authors. Hastings and Book [10] were among the first to present a

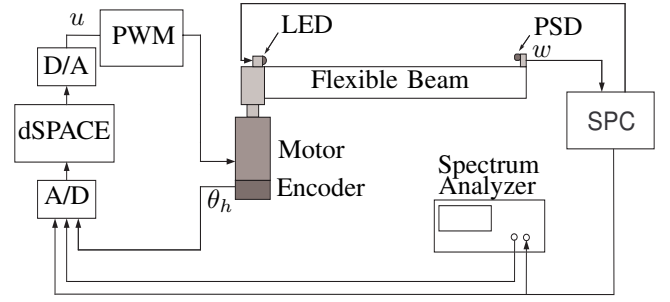


Fig. 2: Experimental setup for the flexible manipulator

TABLE 1: MECHANICAL PROPERTIES OF THE FLEXIBLE MANIPULATOR

Properties	Values
Length, L	0.6 m
Thickness, h	0.003 m
Width, v	0.05 m
Linear density, ρ	0.3975 kg/m
Radius of hub, r	0.025 m
Modulus of elasticity, E	6.894×10^{10} Pa
Cross-sectional area-moment of inertia, I	1.125×10^{-10} m ⁴
Hub moment of inertia (including motor), I_h	1.850×10^{-3} Kg.m ²
Beam moment of inertia, I_b	2.862×10^{-2} Kg.m ²

PDE model for an undamped single-link flexible manipulator. In [4] the authors presented finite order models based on the PDE model presented in [10]. These finite order models include additional terms to account for damping.

The flexible manipulator studied in [9] is modeled as a pinned-free beam with the pinned end attached to the rotating hub. The authors assumed that the beam deflection satisfies the Euler-Bernoulli beam theory. Therefore position of any arbitrary point y on the manipulator can be written as, see Figure 3,

$$y(x, t) = w(x, t) + x\theta_h(t), \quad (1)$$

where $w(x, t)$ is the beam flexural deflection and $\theta_h(t)$ is the hub angle of rotation at time t . Using Hamilton's Principle along with the associated energy equations it was shown that $y(x, t)$ satisfies the fourth order partial differential equation

$$EI \frac{\partial^4 y}{\partial x^4} + \rho \frac{\partial^2 y}{\partial t^2} = 0 \quad (2)$$

with boundary conditions

$$\begin{aligned} EI \frac{\partial^2 y}{\partial x^2} \Big|_{x=0} + T - I_h = 0, w(0) = 0 \\ EI \frac{\partial^2 y}{\partial x^2} \Big|_{x=L} = 0, EI \frac{\partial^3 y}{\partial x^3} \Big|_{x=L} = 0. \end{aligned} \quad (3)$$

Here T denotes the torque input and the other parameters as defined in Table 1.

The first three natural frequencies of the flexible manipulator calculated from the PDE model are tabulated in Table 2. Details on how to calculate the natural frequencies from (2) are not presented here. Interested readers can refer to [4]. Also presented in Table 2 are the experimentally determined natural frequencies of the manipulator. The third elastic mode could not be excited as it was out of the motor bandwidth. The analytical and experimental results differ by about 6%. This error could be due to reasons such as the presence of the PSD at the tip of the manipulator. This amounts to addition of a tip mass to the beam, which is not accounted for in the PDE (2) and its associated boundary conditions (3). In order to accurately model the system for control design, here an experimental approach to modelling (system identification) is taken.

The following frequency response functions (FRFs) are determined for designing the control system:

$$G_{\theta_h u}(i\omega) \triangleq \frac{\theta_h(i\omega)}{u(i\omega)} \quad (4)$$

$$G_{w_{tip} u}(i\omega) \triangleq \frac{w_{tip}(i\omega)}{u(i\omega)} \quad (5)$$

and

$$G_{y_{tip} u}(i\omega) \triangleq G_{w_{tip} u}(i\omega) + LG_{\theta_h u}(i\omega), \quad (6)$$

where $u(s)$ is the input voltage, $\theta_h(t)$ is the hub angle measured using the shaft encoder, $w_{tip}(t) = w(L, t)$ is the flexural tip deflection measured using the PSD and the tip displacement $y_{tip}(t) = y(L, t)$ is computed using (1). The FRFs are first determined non-parametrically and parametric models are later fit to them.

A HP35670A spectrum analyzer is used for the non-parametric determination of the FRFs. A random noise signal from 2 - 75 Hz generated using the spectrum analyser is applied as the input $u(t)$. The output measurements $\theta_h(t)$ and $w_{tip}(t)$ are fed into the spectrum analyser. The spectrum analyser processes the input output data and generates the FRFs (4) and (5) in the non-parametric form. In Figures 4 and 5 the nonparametric FRFs of (4) and (5) are plotted along with corresponding parametric fits. The parametric models fit to data are

$$G_{\theta_h u}(s) = \frac{b(s)}{a(s)} \quad (7)$$

and

$$G_{w_{tip} u}(s) = \frac{p(s)}{q(s)}, \quad (8)$$

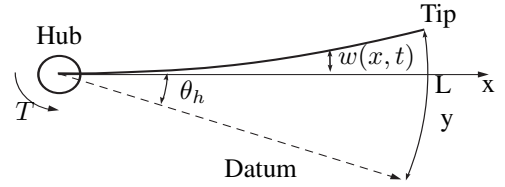


Fig. 3: Flexible manipulator model.

TABLE 2: NATURAL FREQUENCY (HZ) OF THE SINGLE-LINK FLEXIBLE MANIPULATOR

Mode No.	Analytical	Experimental
1	22.17	20.94
2	52.13	55.06
3	123.61	-

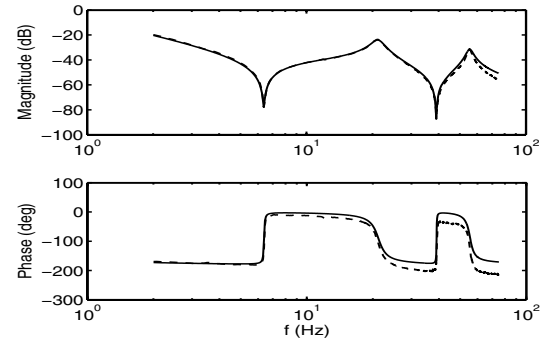


Fig. 4: Identified model (—) and experimental (---) frequency response of amplifier input voltage u to hub angle θ_h .

where

$$b(s) \triangleq 367.0451 (s^2 + 0.4428s + 1605) \times (s^2 + 1.197s + 5.988e004) \quad (9)$$

$$a(s) \triangleq s(s + 1.6)(s^2 + 16.72s + 1.768e004) \times (s^2 + 23.35s + 1.193e005) \quad (10)$$

$$p(s) \triangleq -33655.44 (s^2 + 1.693s + 6.943e004) \quad (11)$$

and

$$q(s) \triangleq (s^2 + 16.72s + 1.768e004) \times (s^2 + 23.35s + 1.193e005). \quad (12)$$

It is worth noting that the poles characterising the flexible modes of the beam in $G_{\theta_h u}(s)$ and $G_{w_{tip} u}(s)$ are the same (i.e., $s(s + 1.6)q(s) = a(s)$). Hence damping the resonances of $G_{\theta_h u}(s)$ using a feedback controller would also damp the resonances in $G_{w_{tip} u}(s)$ and $G_{y_{tip} u}(s)$.

4. CONTROLLER DESIGN

This section discusses the proposed control strategy for vibration damping and position control of the flexible manipulator. The control strategy consists of a polynomial based controller and an integral controller, as illustrated in Figure 6. In designing the controllers, the response of the flexible manipulator needs to satisfy the following specifications:

- 1) Zero steady-state tip positioning error

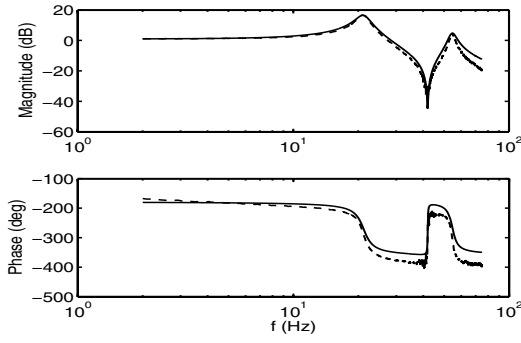


Fig. 5: Identified model (—) and experimental (---) frequency response of amplifier input voltage u to tip deflection w_{tip} .

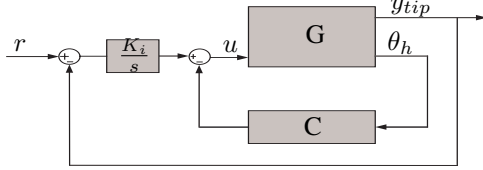


Fig. 6: Polynomial-based controller $C(s)$ and integral controller $K_i/s(s)$.

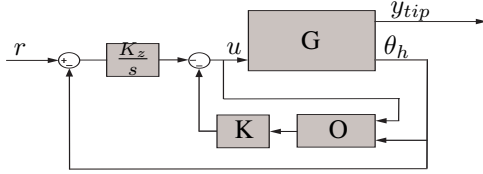


Fig. 7: LQG state feedback controller with integral action scheme.

- 2) Rise time and settling time of less than 1 and 1.5 seconds, respectively.
- 3) Overshoot of less than 2%.
- 4) Minimum of 10 dB damping in the first resonant mode (in order to flatten its peak).

An LQG controller in conjunction with an integral action scheme, see Figure 7, is also designed for achieving the above specifications. This LQG based control scheme has been used by other researchers, e.g. [7], and it is used here for the sake of comparison with the proposed polynomial-based control strategy.

A. Polynomial-based and integral controller

Let

$$C(s) \triangleq \frac{y(s)}{x(s)}. \quad (13)$$

be a proper controller. Standard results in control theory, [11], show that the closed-loop system is given by

$$G_{\theta_h u}^{(cl)}(s) \triangleq \frac{G_{\theta_h u}(s)}{1 + G_{\theta_h u}(s)C(s)}. \quad (14)$$

and the corresponding closed-loop poles are roots of the polynomial

$$c(s) \triangleq a(s)x(s) + b(s)y(s). \quad (15)$$

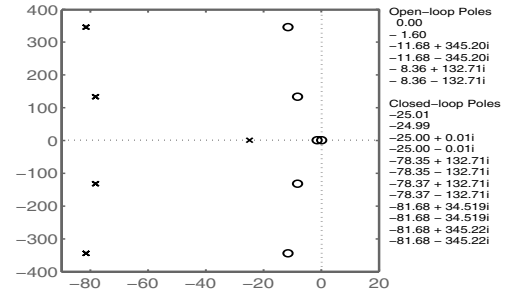


Fig. 8: Open-loop (O) and closed-loop (X) pole locations of the system.

As the model $G_{\theta_h u}(s)$ is of order 6, (15) would represent a diophantine equation for any 12th order monic polynomial $c(s)$. If $\{p_k\}_{k=1}^{12}$ is a desired set of closed-loop poles, and $c(s)$ is the corresponding monic polynomial with $\{p_k\}_{k=1}^{12}$ as its roots, then there exists a unique pair of polynomials $y(s)$ and $x(s)$, of orders 5 and 6 respectively, with $x(s)$ monic, which satisfy (15). The coefficients of the polynomials $y(s)$ and $x(s)$ can be determined by solving the linear equations obtained by matching the coefficients in (15).

Solving for the coefficients though conceptually simple is not numerically well conditioned. Moreover, the controllers rendered by any arbitrary choice of $\{p_k\}_{k=1}^{12}$ need not be stable. The former problem can be tackled by using suitable preconditioning matrices. However, the latter problem of restraining the controller to be stable has not been satisfactorily solved to the authors' knowledge.

In Figure 8 open-loop poles of $G_{\theta_h u}(i\omega)$ and the desired closed-loop pole locations are presented. The controller polynomials $y(s)$ and $x(s)$ obtained for the choice of the closed-loop poles presented in Figure 8 are

$$y(s) = 61128.1795(s + 5.963)(s^2 - 64.13s + 4557) \times (s^2 + 48.39s + 5.956e004) \quad (16)$$

and

$$x(s) = (s^2 + 28.72s + 1861)(s^2 + 150.3s + 6.004e004) \times (s^2 + 519.5s + 1.948e005). \quad (17)$$

A trade off between system damping and controller stability needs to be considered while selecting the closed-loop pole locations. The further away the closed-loop poles are placed (from the open-loop poles) in the left half plane, the higher the system damping can be achieved but this is at the cost of making the controller less stable. In this work, the closed-loop pole locations are optimized to give a high system damping but with a reasonable gain and phase margin.

5. SIMULATION AND EXPERIMENTAL RESULTS

Here the damping introduced by the polynomial based controller on the resonant modes are first evaluated. In

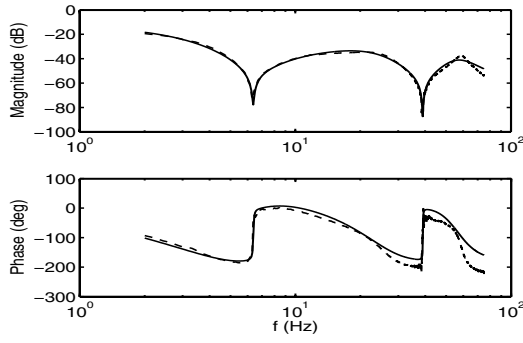


Fig. 9: Simulated (—) and experimental (---) closed-loop frequency response of amplifier input voltage u to hub angle θ_h .

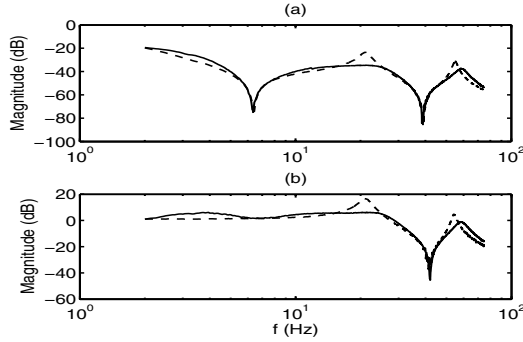


Fig. 10: Closed-loop (—) and open-loop (---). (a) Frequency response of amplifier input voltage u to hub angle θ_h . (b) Frequency response of amplifier input voltage u to tip deflection w_{tip} .

Figure 9 the closed-loop FRF $G_{\theta_h u}^{(cl)}(i\omega)$, (14), is plotted along with its experimentally determined non-parametric counterpart. Experimentally determined non-parametric $G_{\theta_h u}^{(cl)}(i\omega)$ is obtained by applying a random noise as input $u(t)$ using the spectrum analyser and the controller implemented as suggested in in Section 2. It is fairly evident that the experimental results match the simulations except near the second resonant mode. This is due to the fact that the second resonance is very close to the maximum bandwidth of the drive.

In Figure 10 the non parametric (experimentally determined) closed-loop responses $G_{\theta_h u}^{(cl)}(i\omega)$ and $G_{w_{tip} u}^{(cl)}(i\omega)$ are plotted along with their corresponding non-parametric open-loop FRFs $G_{\theta_h u}(i\omega)$ and $G_{w_{tip} u}(i\omega)$ respectively. A damping of the first and the second resonances are evident from the plots. More precisely the magnitudes of the first and second resonant modes are reduced by 10.5 dB and 5.7 dB, respectively.

The goal of this paper is to achieve precise tip positioning. Without loss of generality we wish to position the tip at $y_{tip} = \frac{\pi L}{2}$ with the current position being set to zero. This is normally achieved by applying a step input with step size $\frac{\pi L}{2}$. In order to achieve precise tip-positioning with zero steady state error an integral controller is used. The integral controller gain K_I is chosen such that the response of the flexible manipulator

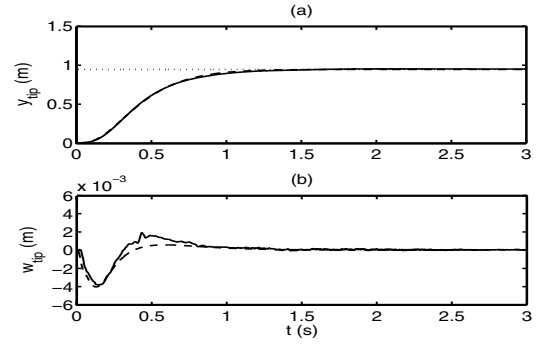


Fig. 11: Time response plots of the flexible manipulator using polynomial-based and integral controller with hub angle and tip deflection feedback. Experimental (—) and simulated (---): (a) Tip position y_{tip} , (b) Tip deflection w_{tip} .

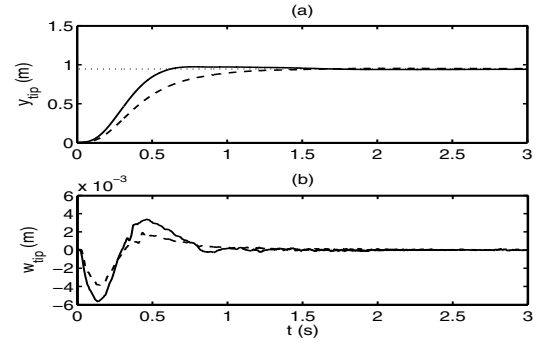


Fig. 12: Time response plots of the flexible manipulator using polynomial-based and integral controller with hub angle and tip deflection feedback. $K_I = 15$ (—) and $K_I = 10$ (---): (a) Tip position y_{tip} , (b) Tip deflection w_{tip} .

conforms to the given specifications. Figure 11 shows the time response of the flexible manipulator in closed-loop to the step input $u(t) = \frac{\pi L}{2}$ with $K_I = 10$. It is apparent from the plot (a) in Figure 11 that y_{tip} has a zero steady-state error, a zero overshoot, a rise time of 0.8 seconds and a settling time of 1.2 seconds. Plot (b) in Figure 11 shows that as a result of the polynomial based controller, tip vibrations due to the resonant modes are almost completely damped. The observed initial deflection in the negative direction is a typical response of a non-minimum phase system. Note that, the response of the tip position and the tip deflection are very similar to simulation results obtained from the identified models.

The rise time of y_{tip} can be reduced by increasing the value of K_I , but this comes at the expense of a higher overshoot. Figure 12 shows the response y_{tip} when K_I is increased to 15. It can be observed that the rise time has decreased to 0.5 seconds while the overshoot has increased from 0 to 3.1%. It is worth noting that, even for a faster tip position response, Figure 12 does not show any exacerbation of the vibrations.

Figure 13 illustrates the response y_{tip} using the LQG controller in conjunction with the integral action, refer to Figure 7. The LQG controller is tuned such that it produces

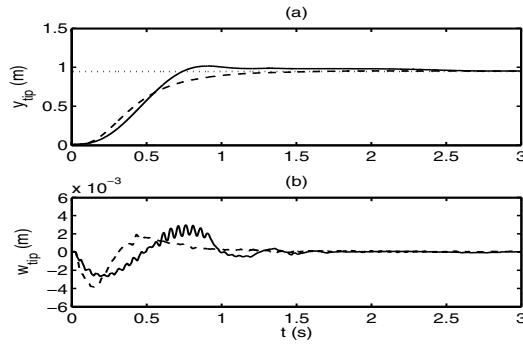


Fig. 13: Time response plots of the flexible manipulator using LQG controller and integral action scheme with hub angle feedback. LQG (—) and proposed controller (---): (a) Tip position y_{tip} , (b) Tip deflection w_{tip} .

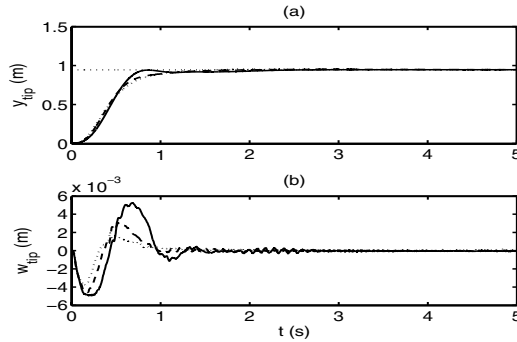


Fig. 14: Time response plots of the flexible manipulator using polynomial based and integral controller with tip mass. Tip mass = 92 g (—), Tip mass = 35 g (---) and No mass (...): (a) Tip position y_{tip} , (b) Tip deflection w_{tip} .

a tip position response that is similar to the one produced by the proposed controller. Figure 13 shows that y_{tip} has a rise time of 0.7 seconds but the tip deflection w_{tip} appears to be affected by the resonance modes.

The robustness of the proposed controller is examined by attaching a certain amount of mass to the tip of the flexible manipulator. Two masses are used here, the first has a weight of 35 g (which is 14% of the flexible beam weight) and a second set has a weight of 92 g (which is 35% of the flexible beam weight). These masses alter the dynamics of the flexible manipulator and also perturb or shift the resonances. Figure 14 shows the response y_{tip} conforms to the given specifications for both the cases. However, in the case of a LQG deterioration in the performance is evident.

6. CONCLUSION

In this paper a single link flexible manipulator is fabricated to represent a typical flexible robotic arm manipulator. Analytical models could not correctly predict the flexible modes, as the models did not account for the structural artifacts introduced by the PSD and other unmodeled dynamics. Hence, an experimental approach to modelling the flexible manipulator was chosen. The transfer-functions characterising the collocated hub angle $\theta_h(t)$ response to the input $u(t)$ and the noncollo-

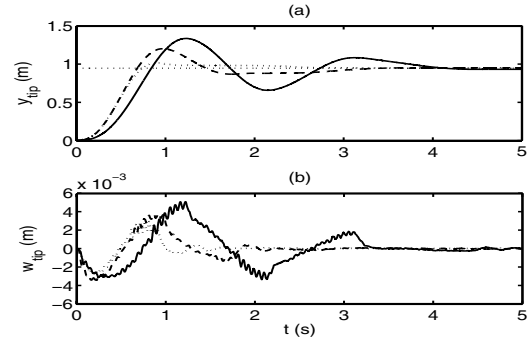


Fig. 15: Time response plots of the flexible manipulator using LQG controller and integral action scheme with tip mass. Tip mass = 92 g (—), Tip mass = 35 g (---) and No mass (...): (a) Tip position y_{tip} , (b) Motor torque T , (c) Tip deflection w_{tip} .

cated tip position $y_{tip}(t)$ response to the input $u(t)$ were found to have the same dynamic modes. This allows for the damping of the tip position $y_{tip}(t)$ response, indirectly, by damping the collocated hub angle $\theta_h(t)$ response. A polynomial based feedback controller was designed to damp the lightly damped modes of the system. However, damping alone does not guarantee a zero steady state error in the tip position $y_{tip}(t)$. Hence an integral controller was designed to enforce this. It was also noted that the polynomial based controller was robust to perturbations in the resonance and rigid modes of the manipulator.

REFERENCES

- [1] R. P. Sutton, G. D. Halikias, A. R. Plummer, and D. A. Wilson, "Robust control of a lightweight flexible manipulator under the influence of gravity," in *Proceedings of the 1997 IEEE International Conference on Control Applications*, 1997, pp. 300–305.
- [2] A. R. Fraser and R. W. Daniel, *Perturbation techniques for flexible manipulators*. Kluwer Academic Publisher, 1991.
- [3] R. H. Cannon and E. Schmitz, "Initial experiments on the end-point control of a flexible one-link robot," *The International Journal of Robotics Research*, vol. 3, no. 3, pp. 62–75, 1984.
- [4] H. Krishnan and M. Vidyasagar, "Control of single-link flexible beam using hankel-norm-based reduced-order model," *IEE Proceeding - Control Theory Application*, vol. 145, no. 2, pp. 151–158, March 1998.
- [5] R. N. Banavar and P. Dominic, "An LQG/ H_∞ controller for a flexible manipulator," *IEEE Transactions on Control Systems Technology*, vol. 3, no. 4, pp. 409–416, December 1995.
- [6] V. A. Spector and H. Flashner, "Modeling and design implications of noncollocated control in flexible systems," *Transactions of the ASME Journal of Dynamic Systems, Measurement, and Control*, vol. 112, pp. 186–193, June 1990.
- [7] R. K. Wen-Wei Chiang and J. Robert H. Cannon, "Design and experimental demonstration of rapid, precise end-point control of a wrist by a very flexible manipulator," *The International Journal of Robotics Research*, vol. 10, no. 1, pp. 30–40, 1991.
- [8] Z.-H. Luo, "Direct strain feedback control of flexible robot arms: new theoretical and experimental results," *IEEE Transaction on Automatic Control*, vol. 38, no. 11, pp. 1610–1622, November 1993.
- [9] D. Wang and M. Vidyasagar, "Passivity control of a single flexible link," in *Proceeding of IEEE International Conference on Robotics and Automation*, 1990, pp. 1432–1437.
- [10] G. G. Hastings and W. J. Book, "Verification of a linear dynamic model for flexible manipulator," in *Proceedings of IEEE International Conference on Robotics and Automation*, April 1986, pp. 1024–1029.
- [11] G. C. Goodwin, S. F. Graebe and M. E. Salgado, *Control System Design*. Prentice Hall International, Inc, 2001.